University of California
Santa Barbara

Fermi level engineering of half-metal Heusler Compounds

A dissertation submitted in partial satisfaction
of the requirements for the degree

Doctor of Philosophy
in
Materials

By

Yu Hao Chang

Committee in charge:

Professor Chris J. Palmstrøm, Chair
Professor John Harter
Professor Michael Gordon
Professor Ram Seshadri

September 2023

The Dissertation of Yu Hao Chang is approved.

_____

John Harter

_____

Ram Seshadri

_____

Michael Gordon

_____

Chris J. Palmstrøm, Committee Chair

June 2023

Fermi level Engineering of half-metal Heusler Compounds

By

Yu Hao Chang

Acknowledgements

The work presented in this dissertation would not have been possible without the guidance and support of many people and groups, especially during this challenging time of a global COVID pandemic. First and foremost, I would like to thank my advisor, Professor Chris Palmstrøm. His patience, commitment to excellence, determination, and great sense of humor has helped me grow as an independent researcher and thinker. He always pays attention to every single detail and individual around him to keep everyone going and motivated, especially during the COVID pandemic. His vast knowledge in material science has facilitated the various directions and foundational concepts that helped facilitated the completion of my degree. His expertise in vacuum equipment and technology always brought new perspectives toward each problem and solution that we faced throughout the years. His willingness and determination to tackle every single problem has motivated me to become someone like him. In addition, I would also like to thank all my other committee members: Professor Ram Seshadri, Professor Michael Gordon, and Professor John Harter for all of their support, providing me feedback, and comments throughout the years. Without their help, many of the ideas and direction would have been lost.

I would like to thank to all the Palmstrøm lab members, past and present, who I have had the privilege to work with: Shinichi, Tobias, Tony (Anthony), Connor, Jason, Aaron, Aranya, Hadass, Collin, Sukgeun, Shouvik, Sean, Masahiko, Joon Sue, Mihir,

Brian, Nate, Jay, Bo, Teun, Michelle, Dan, Anthony, Michael, and Elliot. I was able to grow both as a responsible lab member as well as a friend with them throughout the years.

Beyond our lab group, I would also like to thank many collaborators: Chip Eddy, Jr., and Samantha Rosenberg from the Naval Research Laboratory, Patrick Taylor, and Patrick Folk from the Army Research Laboratory whom I have the honor to work alongside with and experience a different aspect of academia research. I'd like to thank John English and Kurt Olsson for their help and advice while tackling problem in the UHV equipment. I would also like to thank Mark Mangus from IBeAM Laboratory in Arizona State University for the analysis of the RBS data for this thesis and Alexei Fedorov from the Advanced Light Source in Lawrence Berkeley National Laboratory for the help and advice of the ARPES study and measurement. In addition, I would also like to thank all the support staff of CNSI and Nanofab who were vital in keeping the characterization and fabrication tools up and running. Next, I would like to thank all the friends and acquaintances I have made throughout the year in Santa Barbara. Special thanks to my three roommates, Viola, Chao, and Clayton who have shared the challenges, celebrated the wins, and have brought additional balance to my life throughout the years. I would also like to thank Ismail Ibrahim and Anniesha Hack who proofread through my dissertation.

Finally, I would like to thank my parents, Andy and Anne, and my brother Kevin, and the rest of my family members who has provide me encouragement, love, and support throughout the years. All of their unwavering support has truly provided me the strength to overcome the challenges during this difficult time that we are all facing together right now.

Even though the path we took has been a difficult one, I was able to overcome it thanks to everyone that has supported me throughout the years.

Curriculum Vitae

Yu Hao Chang

EDUCATION

University of California, Santa Barbara
Doctor of Philosophy in Materials, anticipated June 2023
Advisor: Professor Chris J. Palmstrøm
GPA: 3.92

University of California, Berkeley
B.S. Chemical Engineering and Material Science & Engineering, 2016
GPA: 3.89

ACADEMIC EXPERIENCE

Graduate Research Assistant, Full Time: 08/2016 – 12/2022

Materials Department, University of California at Santa Barbara. Chris J. Palmstrøm, Advisor, molecular beam epitaxy lab, cjpalm@ucsb.edu

Teaching Assistant, *Materials 215A*: *Semiconductor Device Processing*
Fall 2017, Fall 2020, Fall 2021, Fall 2022

Materials Department, University of California at Santa Barbara. Lead discussion and Laboratory section. Develop course materials including homework and exams.

Teaching Assistant, *Materials 215B*: *Semiconductor Device Processing*
Winter 2021

Materials Department, University of California at Santa Barbara. Lead discussion and Laboratory section. Develop course materials including homework and exams.

SKILLS AND TECHNIQUES

Thin-film growth: Molecular beam epitaxy, Plasma-enhanced atomic layer deposition

Electronic characterization: Spin-resolved and angle-resolved photoemission spectroscopy, scanning tunneling spectroscopy, magneto-transport, Hall effect measurement

Surface characterization: atomic force microscopy, scanning tunneling microscopy, reflection high-energy electron diffraction, low-energy electron diffraction, X-ray photoelectron spectroscopy

Structural/magnetic characterization: High-resolution X-ray diffraction, scanning electron microscopy, SQUID magnetometry, Reciprocal space mapping

Other: Ultra-high vacuum maintenance and design, cleanroom processing, IGOR Pro, MATLAB, Proficient in Mandarin Chinese

WORK EXPERIENCE

3M Company
Research & Development Intern, Summer 2015
Maplewood, MN, USA

Dow Wetland Project – Dow Chemical/Corteva Wetland Preserves
Project Lead, 2014-2016
Antioch, CA, USA

Balsara Research Group – University of California, Berkeley
Undergraduate Researcher, 2013-2016
Berkeley, CA, USA

AWARDS

John M. Prausnitz Award 2016
University of California, Berkeley – College of Chemistry

Dr. Melvin J. Heger-Horst Scholarship 2015
University of California, Berkeley – College of Chemistry

Robert and Elizabeth Polansky Undergraduate Fellowship 2014
University of California, Berkeley – College of Chemistry

LEADERSHIP EXPERIENCE

University of California, Berkeley - Chemical Engineering Consulting
2015-2016
President/Founder

University of California, Berkeley - Cal Environmental Team
2014-2016
Senior Adviser/Chemical Process Manager

University of California, Berkeley - Berkeley Chem-E-Car
2012-2016
Vice President/Project Lead

University of California, Berkeley - American Institute of Chemical Engineers
2014-2016
Vice President

PUBLICATIONS

"High degree $L2_1$ ordering single-crystal full-Heusler Co_2TiGe thin films using post-growth annealing", **Y. H. Chang**, T.L. Brown-Heft, S. Chatterjee, J.A. Logan, and C. J. Palmstrøm. *Applied Physics Letters in Preparation.*

"Identifying the fingerprints of topological states by tuning magnetoresistance in a semimetal: The case of topological half-Heusler $Pt_{1-x}Au_xLuSb$", S. Chatterjee, F.C. de Lima, J.A. Logan, Y. Fang, H. Inbar, A. Goswami, C. Dempsey, J. Dong, S. Khalid, T. Brown-Heft, **Y.H. Chang**, T. Guo, D.J. Pennachio, N. Wilson, S. Chikara, A. Suslov, A.V. Fedorov, D. Read, J. Cano, A. Janotti, and C.J. Palmstrøm. *Physical Review Materials* **5,** 124207 (2021)**.**

"Controlling magnetoresistance by tuning semimetallicity through dimensional confinement and heteroepitaxy", S. Chatterjee, S. Khalid, H.S. Inbar, A. Goswami, T. Guo, **Y.H. Chang**, E. Young, A.V. Fedorov, D. Read, A. Janotti and C.J. Palmstrøm. *Science Advance* **7**: eabe8971 (2021).

"Gated Magnetotransport in α -Sn Thin Films On CdTe", O. Vail, **A. Chang,** S. Harrington, P. Folkes, P. Taylor, B. Nichols, C. Palmstrøm, and G. de Coster. *Journal of Electronic Materials* **50**, 6329–6336 (2021).

"Lithium-Sulfur Batteries with a Block Copolymer Electrolyte Analyzed by X-ray Microtomography", D. Devaux, I. Villaluenga, X. Jiang, **Y.H. Chang**, D.Y. Parkinson, and N.P. Balsara. *Journal of The Electrochemical Society* 167, 060506 (2020).

"Weak antilocalization in quasi-two-dimensional electronic states of epitaxial LuSb thin films", S. Chatterjee, S. Khalid, H.S. Inbar, A. Goswami, F.C. de Lima, A. Sharan, F.P. Sabino, T.L. Brown-Heft, **Y.H. Chang**, A.V. Fedorov, Dan Read, A. Janotti, and C.J. Palmstrøm. *Physical Review B* **99**, 125134 (2019).

CONFERENCE PRESENTATIONS & POSTER

Y.H. Chang, S.D. Harrington, S. Chatterjee, H.S Inbar, and C. J. Palmstrøm. "Chemical potential tuning & strain engineering of Heusler Heterostructures." Contributed talk and poster session presented at Vannevar Bush Faculty Fellowship, April 29 – April 30, 2019, Arlington, VA.

S.D. Harrington, A.D. Rice, **Y.H. Chang**, and C. J. Palmstrøm. “Band engineering and alloying of Heusler Compound Heterostructures.” Contributed talk and poster session presented at Vannevar Bush Faculty Fellowship, April 9 – April 10, 2018, National Harbor, MD.

T.L. Brown-Heft, S. Chatterjee, **Y.H. Chang**, S. Harrington, H. Inbar, A. P. McFadden, J. A. Logan, C. Guillemard, P. Le Fèvre, F. Bertran, S. Andrieu, C. J. Palmstrøm “Tailoring the Magnetic Properties of Epitaxial Heusler Thin Films.” Contributed poster session presented at Vannevar Bush Faculty Fellowship, April 9 – April 10, 2018, National Harbor, MD.

Y.H. Chang, S.D. Harrington, S. Chatterjee, H.S Inbar, and C. J. Palmstrøm. “Engineering Semiconducting Heusler Compound Heterostructures.” Contributed poster session presented at National Security Science and Engineering Faculty Fellowship, April 25, 2017, Dayton, OH.

Abstract

Fermi level engineering of half-metal Heusler Compounds

By

Yu Hao Chang

Heusler compounds are a large family of ternary intermetallic compounds with more than 1500 predicted members across a large fraction of the periodic table [1]. They have been previously shown to exhibit novel electronic and magnetic behaviors such as half-metallic ferromagnetism [2], superconductivity [3], semiconductivity [4], and topologically non-trivial surface states [5]. Recent theoretical predictions [6,7] suggest the presence of time-reversal breaking Weyl and nodal line semimetallic behaviors in full-Heusler half-metallic Co_2TiGe and Co_2TiSn.

In this work, the study of Weyl semimetallic half-metal Co_2TiSn thin film was grown using Molecular Beam Epitaxy. A method of Fermi level tuning by substituting Co with Ni element was applied in order to bring the Fermi level toward the Weyl point to observe the signature of the Weyl semimetallic behavior in this system. The electronic structure of the Co_2TiSn, the effect of Fermi level tuning using Ni alloying, and the probing of any signatures of Weyl semimetallicity in Co_2TiSn were examined by angle-resolved photoemission spectroscopy, electrical, and magnetotransport measurement. In the second part of the study, the Fermi level tuning is used for the half-metal half Heusler PtMnSb, which has been seen as a promising material for spintronics application with inversion

broken symmetry and large spin-orbit coupling, in order to further investigate the interplay of non-trivial band topology and magnetism within this system. The PtMnSb thin film was grown using Molecular Beam Epitaxy. Similar to that of Co_2TiSn, the effect of Fermi level tuning by substituting Mn with Lu element to close the band gap was examined using X-ray diffraction and transport measurement to realize if a potential band inversion/Weyl point formation can form during the topological phase transition from a half metal to a topological insulator through Lu alloying.

Contents

Chapter 1

Introduction

Topology has long been a field of interest among mathematicians, physicists, and material scientists in order to discover exotic matters that is beyond common knowledge. The study of the topological material can be traced back to the early 1970s, where the concept of topology was used to explain why superconductivity occurs in certain materials at extremely low temperatures but disappears at higher ones [8, 9]. J. Michael Kosterlitz and David J. Thouless, received the Nobel Prize in Physics in 2016 for the theoretical discoveries of topological phase transitions and topological phase of matter [10]. This opened up a new field of materials that allows for the production of many promising

devices such as a cancer-scanning laser [11], ultralow energy transistors [12], free-space spatial-division-multiplexing optical transmission [13], increased energy-efficient microelectronic components [14], and many others.

Study of topological material has become a rapidly developing field of research that has interested many scientists to discover new materials that fit within the quantum mechanical regime in the past decades. Many topological materials such as the single element α-Sn as a topological Dirac semimetal [15-20], binary compound of Bi_2Se_3 and Bi_2Te_3 as a topological insulator [21-24], and ternary half-Heusler compound of LuPtBi as a potential topological superconductor [25-27], have been shown to possess the topological properties in both theoretical and experimental studies. In recent years, many Heusler compounds have been predicted to possess different topological properties. This family of compounds is of particular interest because of their high degree of tunability of electronic, magnetic, and structural properties [28]. Specifically, in certain ferromagnetic Heusler compounds, the internal field generated by magnetic moments can lead to the breaking of time-reversal symmetry that give rise to new topological states of matter that possess Weyl semimetallicity which only started to be explored in the recent years [6,7].

1.1 Topological materials

Before the discovery of topological materials, electronic materials have largely been divided into metals and insulator. Metals are materials that possess at least one

partially filled band while insulators are materials with a finite band gap between the filled valence band and empty conduction band. This means that metals can easy conduct as there are empty electronic states available for electrons to be excited into while insulators are nonconducting because of the filled valence band and empty conduction band resulting in no free electrons for conduction. However, in recent years, physicists discovered a new topological state of matter. This discovery resulted in a new type of insulator: the topological insulator. A topological insulator is a quantum phase of matter with the material having insulating bulk states and conducting topological surface states [29], which is different from the traditional insulator where it is insulating throughout the bulk without conducting surface states. One way to understand how these topological phases arise is to understand it by its band structure as shown in figure 1.1 [30]. Band structures are a representation of the energy versus crystalline momentum of electronic states of materials and are used to explain their electronic, optical, and magnetic properties.

For a normal insulator, it possesses electronic bands (the conduction band in red and the valence band in blue) with a finite band gap. Because of this finite band gap, the normal insulator is nonconducting. Now, if that finite band gap is tended toward zero, it will reach a critical point with zero band gap, resulting in trivial semimetals, which are materials that possess no or negative band gap between the conduction and valence band. A topological phase transition can occur when band inversion happens where the orbitals that normally form the conduction band now have energy below what normally forms the valence band. Band inversion, which is a phenomenon results from the crossing of the valence band and conduction band of different parities, usually assumed to result from the

band splitting caused by spin orbit coupling [31]. Spin orbital coupling accounts for the interaction between a particle's spin and orbital angular momentum contribution, which increase with heavier element [32].

This is part of the reason why the search for new topological insulators is focused on materials with heavier elements due to stronger spin orbital coupling. What is interesting is that these resulting surface states have spin degeneracy, meaning that the two surface states each possess a unique spin direction that is spin and momenta are locked [33]. Since there is a spin degeneracy between the surface state, it means that electrons at momentum points k and -k have opposite spin and same energy, which means that the spin has to rotate with k around the Fermi surface in order to transform into the other spin direction. This means that the system preserved time-reversal symmetry [34]. On the other hand, a different type of topological phases can be realized if a band inversion occurred while the system preserved both time-reversal symmetry and other symmetry protection, such as lattice inversion symmetry which reverses the lattice coordinates with respect to a symmetry center [34] as shown in figure 1.2.

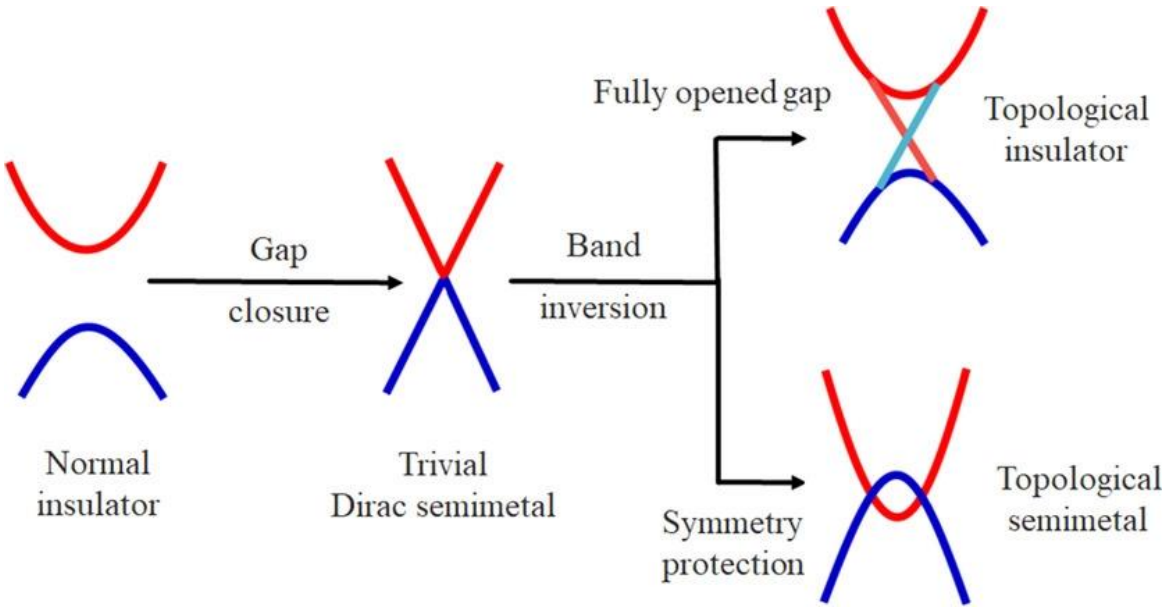

Figure 1.1: Topological phase transition of the topological insulator and topological semimetals. A band inversion on the ordinary insulators can result in a topological insulator. A band inversion on the normal insulator at the critical point with zero band gap and symmetry protection can result in topological semimetals. Image reprinted from [30] with permission.

Unlike that of the topological insulator, topological semimetals possess a pair of crossing points. For topological semimetals that has either time-reversal symmetry or lattice inversion symmetry broken, it results in Weyl semimetal that is two-fold degenerate and has a total of two linear crossing of two points, which is also known as Weyl points. For topological semimetals that preserved both the time-reversal symmetry and lattice inversion symmetry, it results Dirac semimetals that has a four-fold degenerate and has a total of four linear crossing of four points, which is also known as Dirac points [30].

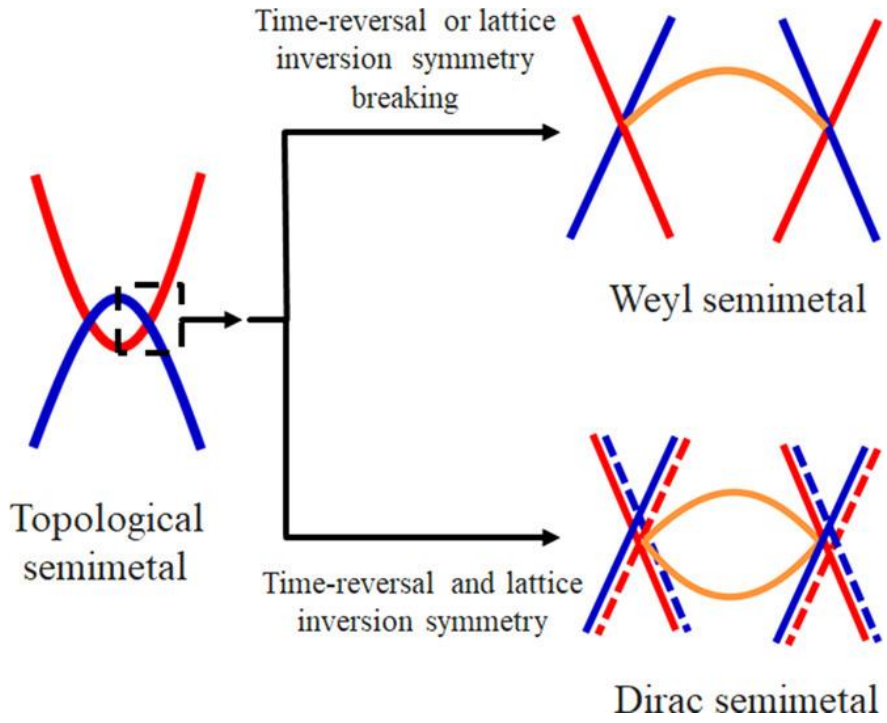

Figure 1.2 Topological phase transition between the topological semimetal and the Weyl semimetal or Dirac semimetal depending on the symmetry. The Dirac semimetals require the coexistence of the time reversal symmetry and inversion symmetry while the Weyl semimetals require the symmetry breaking of either time reversal symmetry or the lattice inversion symmetry breaking. Image reprinted from [30] with permission.

1.2 Heusler compounds

The Heusler compound is a class of ternary compounds that was first discovered by Fritz Heusler in 1903 when he studied the full-Heusler compound Cu_2MnAl, where none of its constituent elements is magnetic by itself, behaves like a ferromagnet [1, 35]. Since the discovery of the Heusler compound, there are predictions of more than 1,500 compounds with similar crystal structures having a vast array of tunable properties as

shown in figure 1.3. However, only a small fraction of the Heusler compounds have been studied.

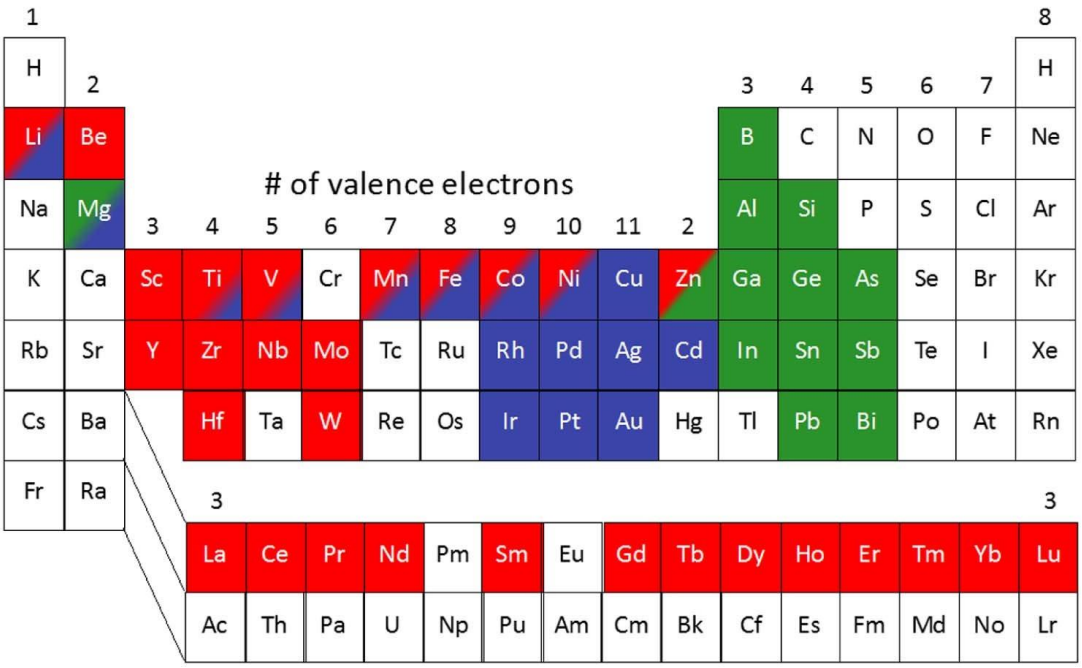

Figure 1.3: Periodic table with color coding showing the typical elements for X (blue), Y (red) and Z (green) in the half-Heusler XYZ and full-Heusler X_2YZ compounds. Image reprinted from [35] with permission.

In Figure 1.4. The full-Heusler compound has a 2:1:1 stoichiometry and half-Heusler compound has a 1:1:1 stoichiometry. The half-Heusler compounds have the general formula XYZ and crystallize in a non-centrosymmetric cubic structure, which often refers to space group $F\bar{4}3m$. Half Heusler compounds have the structure of MgAgAs ($C1_b$). The structure of half-Heusler compounds can often be thought of as a zinc blende XZ

structure with its octahedral lattice sites all filled by Y atoms. On the other hand, full-Heusler compounds have the general formula of X_2YZ and crystallize in the cubic space group $Fm\bar{3}m$. Full-Heusler compounds have the structure of Cu_2MnAl ($L2_1$). The structure of full-Heusler compounds can often be thought of as a rock salt YZ structure with its tetrahedral lattice sites all filled by X or with four interpenetrating face-center cubic sublattices with each occupied by two of X and one of Y and Z atoms [1, 35].

With a large number of compounds within the Heusler family, it is expected to exhibit a wide variety of properties which depends on the choice of atoms in the formula unit. These properties range from metallic (Ni_2TiSn [36]), semiconducting (CoTiSb [37]), shape memory (Ni_2MnGa [38]), half-metallic (Co_2MnSi [39]), superconductivity (TbPdBi [40]), topologically non-trivial surface states (LuPtBi [26], YPtBi [26]), and Weyl semimetallic (Co_2TiZ (Z=Si, Ge, Sn) [7]). In addition, this family of materials has attracted much attention not only due to the vast number compounds this family has, but also because of the possibility of predicting the material properties of many Heusler compounds by a simple valence electron count per formula unit [1, 35].

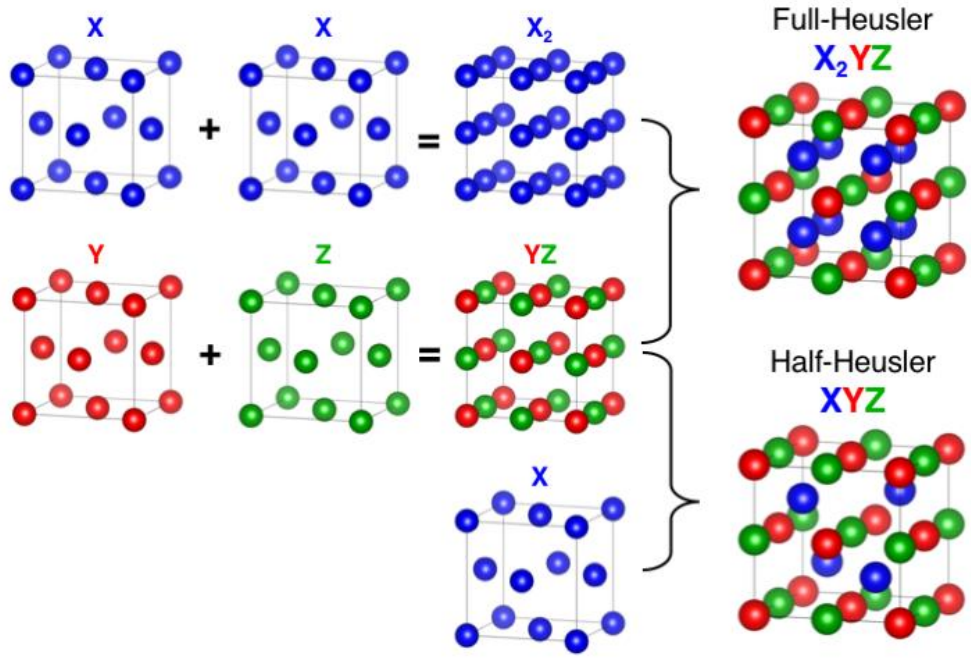

Figure 1.4: The crystal structure of the full-Heusler and half-Heusler compound. The full-Heusler compound can be view as four interpenetrated face-centered cubic crystals as shown by the individual X, Y, Z atom crystal structure. Similarly, the half-Heusler compound can be view as a combination of the YZ rocksalt structure and face-center cubic X sublattice.

Figure 1.5 shows the list of electronic structures for full and half-Heusler compounds. For example, a half Heusler compound with 8 or 18 valence electrons results in a material with topological or semiconducting properties and some of the Full Heusler compounds with 26-29 valence electrons results in materials with superconducting properties. Lastly, Heusler compounds are very promising due to their high compatibility with traditional III-V substrates and large tunability.

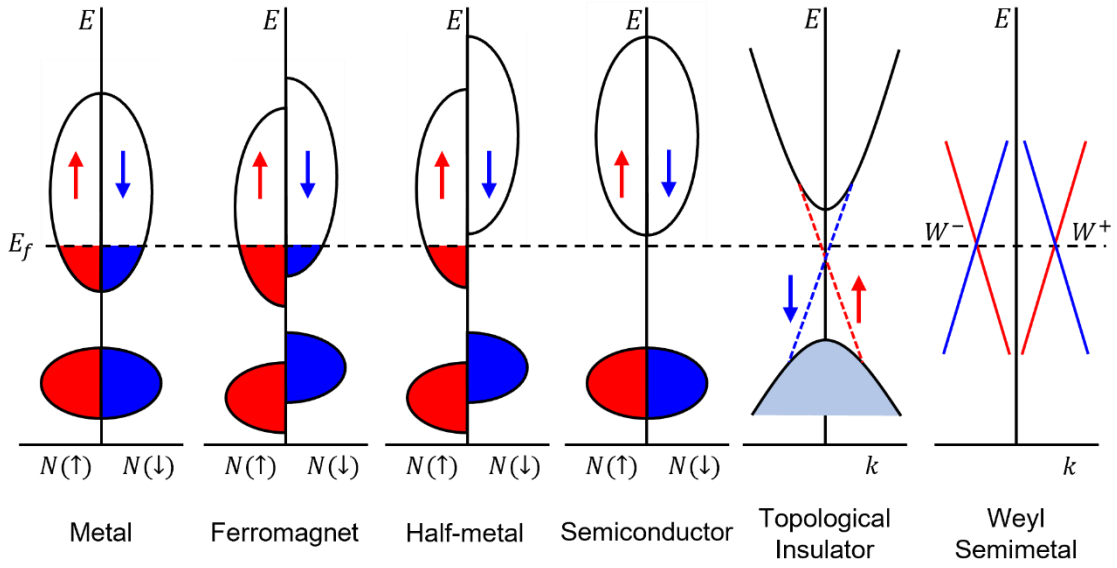

Figure 1.5: electronic properties of full and half Heusler compound as a function of the number of valence electrons per formula unit. Ferromagnet with 17 and 19 electrons, half-metal with 22 electrons, semiconductor with 8 and 18 electrons filled d-band, topological insulator with 8 and 18 electrons possesses band inversion, superconductor with 27 electrons, and Weyl semimetal with 8 and 18 electrons possesses Weyl points. Image reprinted from [41].

This allows them to form quaternary and other complex compounds for other exotic properties. For example, a recent study shows that vanadium doping in $Co_2Ti_{1-x}V_xSn$ allows the Fermi level tuning of Weyl point toward the Fermi level without significant affect in chemical disorder of the compounds [42]. These promising behaviors suggest the understanding of exotic properties and useful interfaces can be done through heterostructure, while maintaining similar lattice parameter and crystal structure throughout the heterojunction.

1.2.1 Chemical ordering in Heusler compound

Chemical order has been shown to be an important factor when it comes to affecting the intrinsic properties of the materials [7, 43-46]. However, determining the chemical ordering of ternary compounds can prove to be difficult because of the number of different combinations of disorder and crystal structures that can be formed compared to single element or binary compound. This is often a great challenge when it comes to determining the chemical ordering of ternary Heusler compounds. Figure 1.6 shows the typical $L2_1$ full-Heusler structure, $C1_b$ half-Heusler structure, and the B2 disorder structure of the Full Heusler compound. For full-Heusler structure, 3 different chemical orders can be realized: the complete $L2_1$ Full Heusler ordering where each of the X, Y, and Z atoms occupied the respective atomic site shown in Figure 1.4, the B2 (CsCl) ordering, which is completely disordered between the Y and Z atoms, and the A2 ordering (not shown in figure), which is completely disordered among the X, Y, and Z atoms. In Heusler Weyl semimetal materials such as Co_2MnAl, it was shown that a B2 disordering phase resulted in a reduction in anomalous hall conductivity, magnetoresistance, and Berry curvature contribution which originated from the Weyl point compared to those calculated $L2_1$-ordered Co_2MnAl in both theoretical prediction and experimental result alike [47]. In this work, X-ray diffraction reciprocal space mapping is used in Chapter 3 to demonstrate a systematic way of studying chemical ordering of the Co-based Heusler compound to determine an optimal synthesis condition to achieve high $L2_1$ full-Heusler ordering.

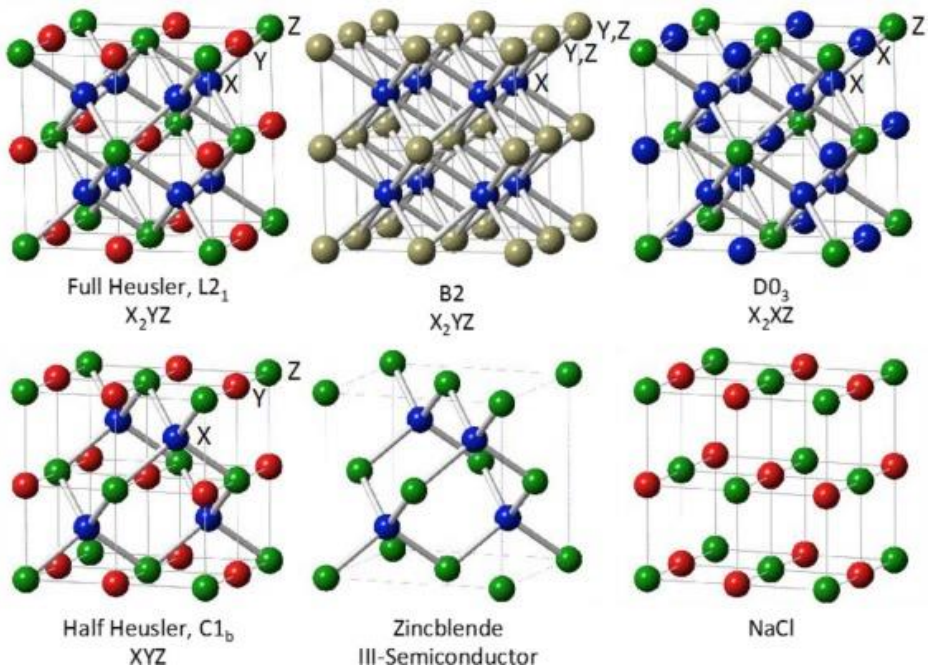

Figure 1.6: General ordered cubic crystal structure for the full-Heusler X_2YZ and half-Heusler XYZ. The B2 structure is when Y and Z are completely disordered and $D0_3$ is when X and Y are the same element (X_2XZ). The NaCl and Zincblende structure are there to present the strong similarities between those and that of the half-Heusler compounds. Image reprinted from [35] with permission.

1.2.2 Theoretical calculated electronic structure of Weyl Semimetal Full Heusler Co_2TiSn

One of the focuses of this work lies in the Co-based full-Heusler compounds. Co_2TiSn is a half-metallic, full-Heusler compound that have been recently predicted to be a topological Weyl semimetal [6,7]. Theoretical calculations suggest that this half metallicity can give rise to both the Weyl semimetal and nodal-line semimetal state, which require the crossings of two singly degenerate spin polarized bands [7]. Theoretical calculation done by Payal Chaudhary et al. [42] calculated the electronic structure of the

Co_2TiSn with the spin-orbit coupling show in figure 1.7. In this study, a calculated minority spin band gap of 0.5 eV was found while a clear band crossing can be seen in the majority spin between the conduction and valence bands along the $\Gamma - X$ and $\Gamma - K$ direction. Furthermore, additional band crossings between the majority and minority spins can be seen as the two spins electronic structures are overlayed. The band crossing in the Co-Ti hybridized 3d band that is denoted by the red circle can be seen in the electronic structure along the $\Gamma - X$, $\Gamma - K$, and $\Gamma - W$ direction. The two Weyl points W_{001}^{2} and W_{001}^{3} are determined to be about 0.278 eV above the Fermi level [42].

However, due to the large energy difference between the Fermi level and the Weyl points, it has been shown to be a challenge to study its Weyl semimetallic properties by transport on the stochiometric structure. In addition, the study on the realization of $L2_1$ ordering of these Co-based full Heusler compounds also has not been done. Chemical order has been shown to be an important factor when it comes to affecting the intrinsic properties of the materials. In Heusler Weyl semimetal materials such as Co_2MnAl, it was shown that a B2 disordering phase resulted in a reduction in anomalous hall conductivity, magnetoresistance, and Berry curvature contribution originated from the Weyl point compared to those calculated $L2_1$-ordered Co_2MnAl in both theoretical prediction and experimental result alike [47].

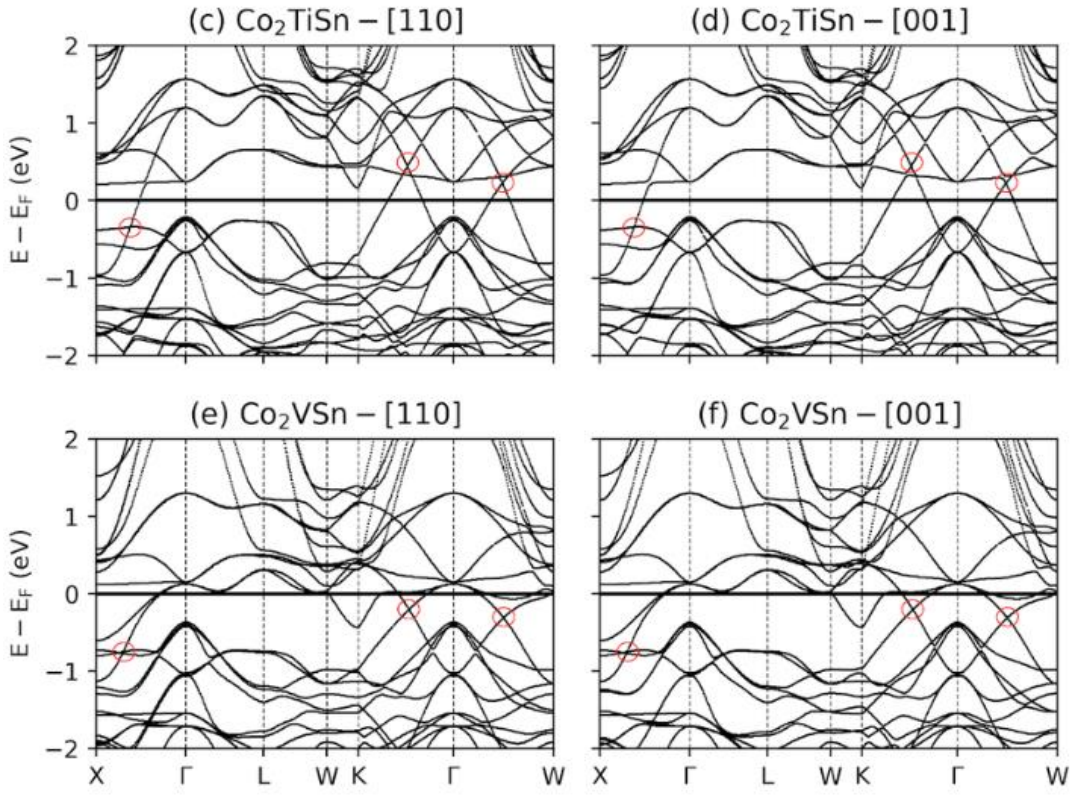

Figure 1.7 (c), (e) Calculated band structures of Co_2TiSn and Co_2VSn with spin-orbit coupling in the [110] quantization direction. (d), (f) Calculated band structures of Co_2TiSn and Co_2VSn with spin-orbit coupling in the [001] quantization direction. The red circles indicate the location of the crossings in the Co-Y (Y = Ti, V) hybridized 3d bands. Image reprinted from [42] with permission.

The goal of this work then is to develop a method to synthesize these materials using Molecular Beam Epitaxy (MBE) and optimize the growth conditions to obtain a thin film with highly $L2_1$ chemical order, utilize Fermi level tuning to shift the Weyl point toward the Fermi level, and understand the behavior of electronic structure as well as Fermi level tuning through angle-resolved Photoemission spectroscopy (ARPES).

1.2.3 Topological phase transition of $PtMn_xLu_{1-x}Sb$ from a half metal to a topological insulator

The second part of the dissertation focuses on the study of PtMnSb. PtMnSb is one of the first predicted half-metals with high Curie temperature above room temperature By R.A. de Groot in 1983 [48]. PtMnSb was predicted to possess both broken inversion symmetry and large spin-orbit coupling. However, even after 2 decades, there has been very little experimental works done on PtMnSb [48-50]. The work of PtMnSb film growth on the oxide substrate has been limited to low crystallinity quality films [49, 50].

In this study, we establish a method to stabilize the growth of high-quality single crystal PtMnSb thin films using Molecular Beam Epitaxy on LuSb (001) buffer layers grown on GaSb (001) substrate to achieve epitaxial films of PtMnSb (001). In the second part of this study, what we are interested in is to determine if there will be any possible Weyl phase results from the band crossing within the band gap because of the band closing by Mn-Lu alloying. Thus, in this study, we need to establish a method to stabilize the growth of $PtMn_xLu_{1-x}Sb$ thin film using Molecular Beam Epitaxy on a LuSb buffer layer. Furthermore, the alloyed $PtMn_xLu_{1-x}Sb$ thin films were examined through transport measurement in order to understand if Lu alloying of PtMnSb results in band inversion/Weyl point formation during the topological phase transition from a half metal to a topological insulator.

1.3 Fermi level tuning

Fermi level tuning is a technique in which an alloying element, which has either more or less valence electron than the host element, is introduced into a materials system as a substitutional element. This allows the shifting in Fermi level in order to achieve certain properties that otherwise cannot be observed for the stochiometric formula. For example, Fermi level tuning using Pb alloying in Bi_2Te_3 allows a tuning of the Fermi level. Since Pb has one less electron than Bi, Pb will acts as hole doping and decrease the bulk electron density. This results in the Dirac cone become isolated from the bulk states and the topological surface state is well isolated. It was found that approximately 10% Pb alloying results in the isolation of the Dirac cone from the bulk states, resulting in a truly bulk insulating topological insulator from ARPES and transport measurement [51].

Another example is a computational analysis that uses vanadium alloying in half-metallic full-Heusler Co_2TiSn to tune the Fermi level towards the Weyl point in order to realize the Weyl semimetallic properties through predicted transport measurement [42]. However, the method of Fermi level tuning needs to be carefully considered as the alloying element can possibly bring a change in the crystal structure, electronic band structure and material properties. Chapter 4 shows the study of utilizing the method of substituting Co atoms with Ni at the Co site, adding an additional electron, for the Co_2TiSn in order to shift the Fermi level up in energy towards the Weyl point.

1.4 Overview of this Dissertation

This dissertation outlines the effort to study the half-metallic full-Heusler compound Co_2TiSn, which were recently predicted to possess Weyl semimetallic properties, and the half-metallic half Heusler compound of PtMnSb.

Chapter 2 discusses the capabilities and infrastructure involved in molecular beam epitaxy. The tools and techniques utilized to calibrate the growths and characterize the resulting samples are also detailed.

Chapter 3 and 4 discusses the growth of Co_2TiSn thin film using Molecular Beam Epitaxy, the method of using high temperature post growth annealing process to achieve $L2_1$ ordering, the method of using Fermi leveling tuning by Ni alloying Co_2TiSn in order to shift the Fermi level toward the Weyl point. A detailed study of the growth, post-growth annealing, surface morphology, electrical and magnetic transport, and ARPES measurement of Co_2TiSn was presented.

Chapter 5 discusses the results of half Heusler PtMnSb. This chapter presents the growth and transport of the stoichiometry PtMnSb as well as the Lu alloying PtMnSb in order to investigate the interplay of non-trivial band topology and magnetism. A detailed study of the growth, surface morphology, electrical and magnetic transport, and a short preliminary study of the ARPES measurement of PtMnSb was presented.

Chapter 6 summarizes the dissertation and provides a future direction to the work that has been presented here. It includes a method of improving surface morphology using

different substrates as well as a future direction in order to discover the Weyl semi metallicity in Co_2TiSn as well as ARPES analysis of the Lu alloying PtMnSb thin film.

Chapter 2

Growth and Characterization Techniques

2.1 Interconnected ultra-high vacuum growth and characterization system

The thin film samples studied in this dissertation were prepared using the interconnected molecular beam epitaxy (MBE) facility in the Chris J. Palmstrøm Lab at the University of California, Santa Barbara. The lab consists of multiple interconnected

ultra-high vacuum (UHV) growth and characterization instruments chambers, as shown in Fig. 2.1. The interconnected system includes seven MBE chambers, three bi-direction transfer chambers that have the capability for electron beam (e-beam) and/or effusion cell deposition of various metals and oxides, angle-resolved photoemission spectroscopy (APRES), magneto-optic Kerr effect (MOKE) magnetometry, X-ray photoemission spectroscopy (XPS), and two scanning tunneling microscopy (STM) systems. In addition, other various *ex-situ* measurement techniques were utilized, including physical property measurement system (PPMS) and superconducting quantum interference device (SQUID) from the Chris J. Palmstrøm Lab, atomic force microscopy (AFM) and high resolution x-ray diffraction (XRD) from the California NanoSystems Institute at University of California, Santa Barbara, and spin-resolved and angle-resolved photoemission spectroscopy (spin-APRES) from both Advanced Light Source at Lawrence Berkeley National Laboratory (LBNL), Berkeley and SLAC National Accelerator Laboratory at Stanford University.

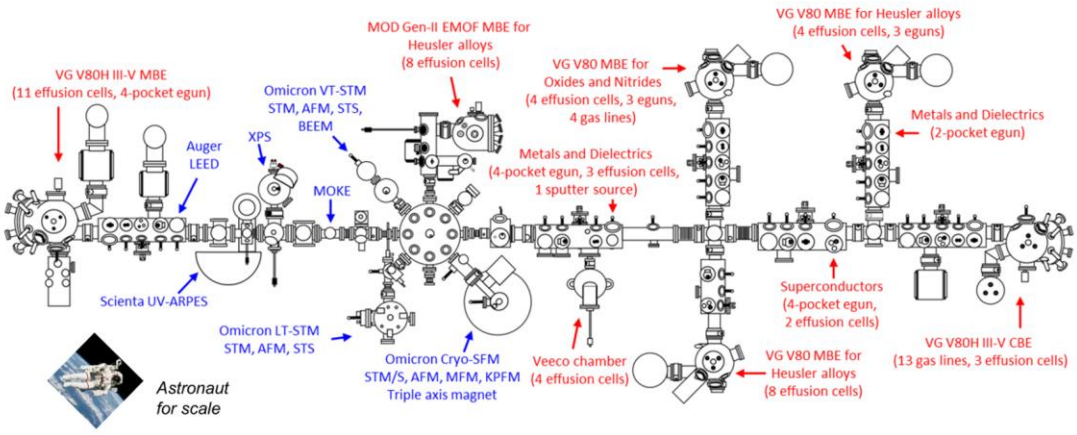

Figure 2.1: Ultra-high vacuum interconnected molecular beam epitaxy and surfaces characterization suite in the Chris Palmstrøm Lab at University of California Santa Barbara.

Each equipment and measurement module has its own unique capabilities and limitation. Some of them that were used for the study of this research work presented here will be further described in the following sections.

2.2 Molecular beam epitaxy (MBE)

MBE is a technique that started its appearance in the mid-1900s. It is a material synthesizing technique that allows high precision control over its crystal growth condition and crystal quality. An MBE system shown in Figure 2.2 is typically composed of several effusion cells and/or e-beam deposition modules, a manipulator with a substrate heater that controls the growth temperature of the thin film, and reflection high-energy electron diffraction (RHEED) that provides the preliminary surface characterization of the growing thin film. Effusion cell, also often known as Knudsen cell, is an effusion evaporator that allows high precision control over the growth rate by controlling the crucible temperature that the source material is placed. Typically, it contains a high-purity elemental source material and can control the growth rate in the regime of ~ 2 Å/min for different elemental sources in a UHV environment. This slow growth rate allows atomic layer control over the sample structure, interfaces, and surface termination.

However, in order to achieve this epitaxy growth regime, an ultra-high vacuum (UHV) environment is required. UHV environment has various definitions, but with the field of thin film and epitaxial growth, it is often referred to as pressures lower than 10^{-9}

Torr. However, for a MBE system, a chamber base pressure of $<5\times10^{-11}$ Torr is desired. With this base pressure, the gas molecules within the MBE system can be considered ballistic and non-interacting with a mean free path in the range of kilometers. However, in order to achieve such low base pressure, several pumping systems are required.

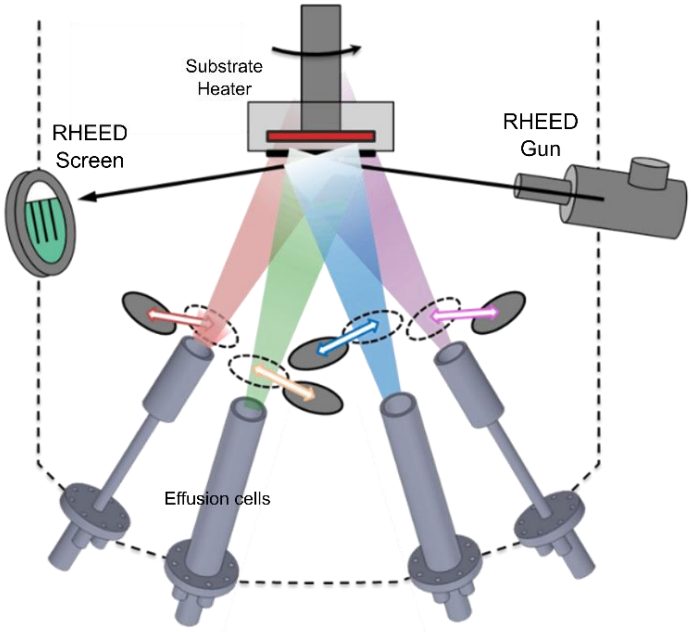

Figure 2.2. Schematic of a Molecular beam epitaxy

The MBE system is typically first pumped out using an oil free roughing pump such as a scroll or diaphragm pump. These pumps can typically bring the pressure down to the range of 10^{-2} – 10^{-3} Torr. After such pressure is achieved, a turbo pump, ion pump, cryopump and combinations of these can be used to further decrease the pressure to$<10^{-10}$ Torr. Some III-V MBE systems also utilized cryopump to allow higher pumping speed to achieve the low base pressure that is desired. In addition to external pumping units, a Titanium sublimation pump, which is a series of Titanium filaments that is installed *in-situ* to the

MBE system, can be used at high base pressure to getter reactive species while the other pumps are active. Lastly, in order to achieve the base pressure of 10^{-11} Torr, the cryoshield of the MBE system is filled with liquid nitrogen to absorb any residual gases with boiling point higher than 77 K, such as water and hydrocarbons. Besides the pumping units, regular maintenance of the MBE system is also required to achieve an UHV environment. Maintenance of the MBE typically involves checking for leaks and baking of the system. The MBE system is baked at 150 – 200 ^{o}C for several days while having an active pump to remove any residual gases. High baking temperature is often desired so any water molecule within the chamber can be removed. After the baking process, a full sweep of the system is required to examine any potential leaking to the atmosphere. This is done by using a residual gas analyzer (RGA) to detect Helium element by sprayed the Helium gas between the metal seals part and welding of the chamber.

A proportional-integral-differential (PID) feedback controller is used for both the effusion cell and manipulator substrate temperature control. A high precision control is required during the thin film growth for both the effusion cell and substrate temperature to avoid any abrupt change of elemental flux from the cell or substrate temperature. However, the thermocouples within these components are governed by infrared radiation and are not in direct contact. As a result, the thermocouple temperature reading typically can result in a deviation of 50 – 100 ^{o}C or more to the real temperature. This issue can be detected and resolved by several methods. For substrate temperature, a precise temperature value can be calibrated by either using a pyrometer that used calibrated infrared emissivity values of known substrate or using well-known phase transition that occurred at specific temperature

for calibration. Similarly, each effusion cell for different elemental source can also be calibrated by different flux measurement techniques by determining the amount of material that has been deposited in a fix period of time using techniques such as Rutherford backscattering spectrometry (RBS), RHEED oscillation, quartz crystal microbalance (QCM), and many more. Some of the techniques that are used for this dissertation will be further described in the following section.

The process of the MBE growth is described as following: The flux of the effused atoms from the effusion cell is governed by an Arrhenius behavior.

$$\phi_{\text{flux}} = \phi_{\text{o}} \cdot e^{-\frac{E_a}{k_B T}} \tag{2.1}$$

Where ϕ_o is pre-exponential rate factor accounting for geometric consideration between the effusion cell position and the target sample, E_a is the activation energy, k_B is the Boltzmann constant, and T is the temperature. The effused atoms absorb at the surface of the targeted substrate and become adatoms. Two major interactions at the surface will typically occur. The adatom can either desorbed from the surface, which will define the sticking coefficient of each element at different temperature or go through a process of surface diffusion at the surface of the substrate. The adatom that goes through surface diffusion will continue until it reaches the lowest energy position. Because of this complex process, many important considerations, such as effusion cell temperatures, stoichiometric ratio of the targeted thin film, substrate temperature, growth rate, and many more are needed in order to produce the desired samples.

2.3 Calibration Techniques for Heusler Growth in MBE

Flux calibration is an important step to achieve high precision control of the MBE growth. As previously noted, atomic flux is governed by an Arrhenius behavior shown in equation 2.1. In this work, calibration of the effusion cell is typically done by four different methods: RHEED oscillation, beam flux measurement, Rutherford backscattering spectrometry (RBS), and quartz crystal microbalance (QCM) measurement.

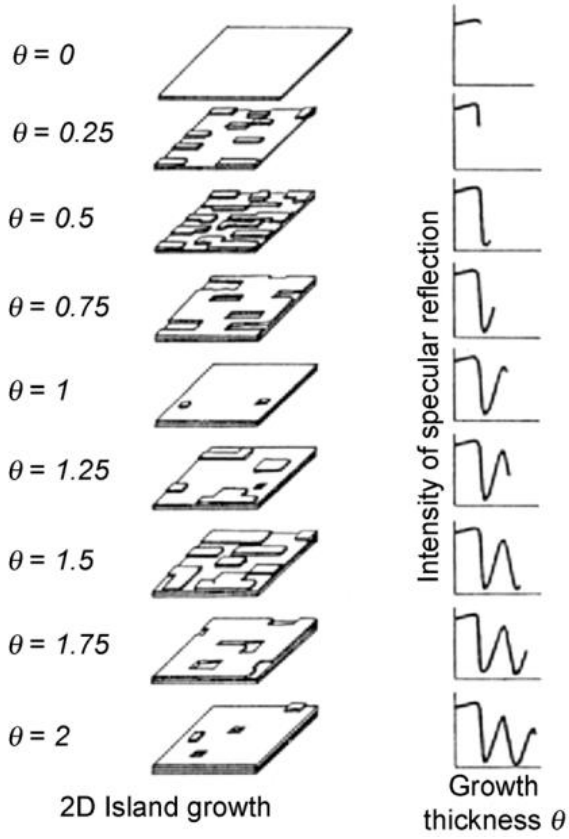

Figure 2.3 Illustrations showing a 2D-island growth style and the intensity change of specular spot during the growth. Image reprinted from [52] with permission.

A fast and *in-situ* method of measuring the flux is using RHEED oscillation shown in figure 2.3. RHEED oscillation can be used when a layer-by-layer growth mode is present. It is typically used for a single element such as Sn and some binary compound that has a layer-by-layer growth mode at the start of growth. At the starting surface, the RHEED beam intensity is at its maximum from a known substrate with a smooth surface. As the adatom from the effusion cell begin to cover the substrate surface, the RHEED intensity starts to drop due to lower coherent from the reflected beam with a minimum value at 50% coverage. As the single monolayer began to fully cover, the reflected coherent beam is increased to a maximum when the single monolayer is fully covered. By understanding the crystal structure of the grown samples, the time it takes for each maximum to achieve can be used to do back-calculations with the Arrhenius equation to determine the growth rate. However, for this dissertation, RHEED oscillation was only used in the study of α-Sn, while the calibration for the Heusler growth is all done by beam flux measurement and Rutherford backscattering spectrometry (RBS).

Beam flux measurement is typically done by a commercially available ionization gauge placed in the path of the molecular beam. It is designed to be placed under the manipulator and retracted away to prevent blocking the growth path during MBE growth. The ion gauge is used to measure the beam-equivalent pressure of the effusion cell flux at different temperature when RBS samples is grown. The ion gauge is consisting of a filament that is driven by a current; this generates electrons that emit from the filament and are accelerated towards a positively biased grid. The electrons then collide with the incoming effused atoms and ionize atoms. These ionized atoms are attracted to a collector

wire in the center of the grid cage and the resulting current is measured and is proportional to the beam-equivalent flux of atoms. A fix electron emission current from the filament is required for reproducibility and conversion between collector current and beam-equivalent pressure. However, this beam-equivalent pressure only provided a relative flux value that relates the cell temperature and the ion gauge pressure. In order to measure the number of atoms per unit area that have been deposited on a substrate, Rutherford backscattering spectrometry (RBS), an overview of the RBS technique is describe in Appendix A) is utilized. RBS measurements are performed at the Ion Beam Analysis of Materials facility in the Eyring Materials Center at Arizona State University and Ion Beam Analysis of College of Science & Engineering in Shepherd Labs at University of Minnesota. RBS is an ion scattering technique that use high energy ions, typically 2-3 MeV He^{+} or He^{++}, directly onto the sample and the energy distribution and yield of the backscattering high energy ions at a fixed angle is measured. This technique does not require a reference standard as the backscattering cross section and the ion energy loss (stopping power) for each element are known. Thus, it is possible to obtain a quantitative compositional depth profile from the RBS spectrum.

RBS can be used to accurately measure total areal atomic density of the sample and differentiate multiple elements by measuring the yield and energy of backscattered high energy ions impinging on a sample. By determining the energy position of different elements, multiple elements can be measured in a single thin film. The fitting of the RBS measurements is fitted using RUMP software, see Appendix A. Figure 2.4 shows an example of the raw RBS data and the corresponding fitting between temperature and the

RBS flux result. This is used to calibrate the beam-equivalent pressure measured with the ion gauge and cell temperature with respect to atomic flux. This calibration needs to be performed fairly regularly as changes in shape of source charge in the crucible or material building up at the lip of the crucible will influence the atomic flux uniformity. A feedback loop between RBS measurement and ion gauge measurements is used to ensure the effusion flux is controlled at a high precision.

Lastly, quartz crystal microbalance (QCM) measurement is used mainly for both the Magnesium oxide buffer growth and Aluminum oxide capping in this study. QCM is operated by measuring the frequency of a resonating quartz crystal. As elements or compounds are deposited onto the crystal, QCM monitors the change in mass or thickness of layers adhering to the surface of a quartz crystal. This is achieved by measuring the change in resonance frequency of the quartz crystal upon excitation by a driving voltage. With the known density and Z-factor, the frequency shift can be correlated with the thickness of the deposited material.

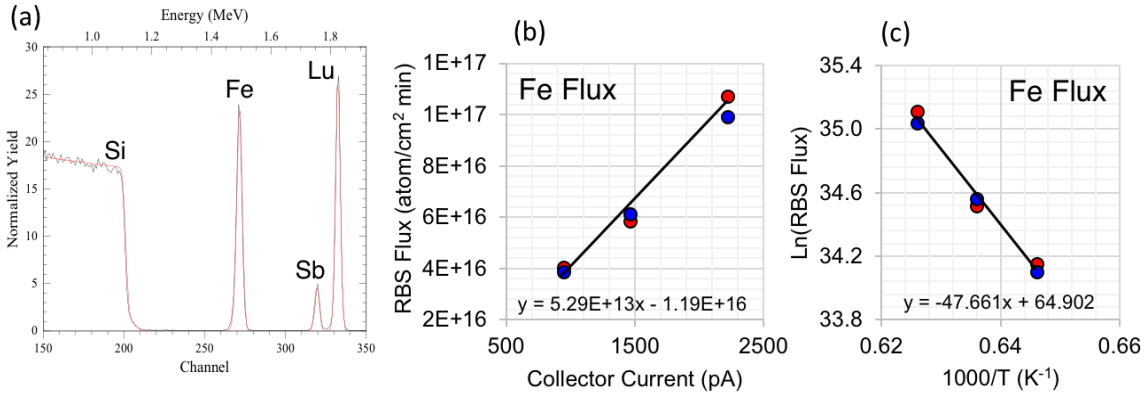

Figure 2.4 raw RBS data and the corresponding fitting between temperature and the RBS flux

2.4 Reflection high-energy electron diffraction

Reflection high-energy electron diffraction, also known as RHEED, is a common technique that is widely used during the growth of thin film in Molecular beam epitaxy. RHEED is typically composed of 2 main apparatus: the electron gun and the RHEED screen. The electron gun is typically positioned parallel to the substrate manipulator and has an incident on the target sample at a grazing angle of a few degrees. The incident electron that collided at the surface is then scattered near the grazing incidence and strikes a RHEED screen. The schematic of the RHEED is shown in Figure 2.5. A typical RHEED gun allows the use of electron beam with an energy between 8 and 100 keV. Usually, electron optics become easier as the energy is increased. However, at lower energies, it is possible to go to higher incident glancing angle while maintaining surface sensitivity as it makes step edges as well as multiple scattering between terraces less important [53].

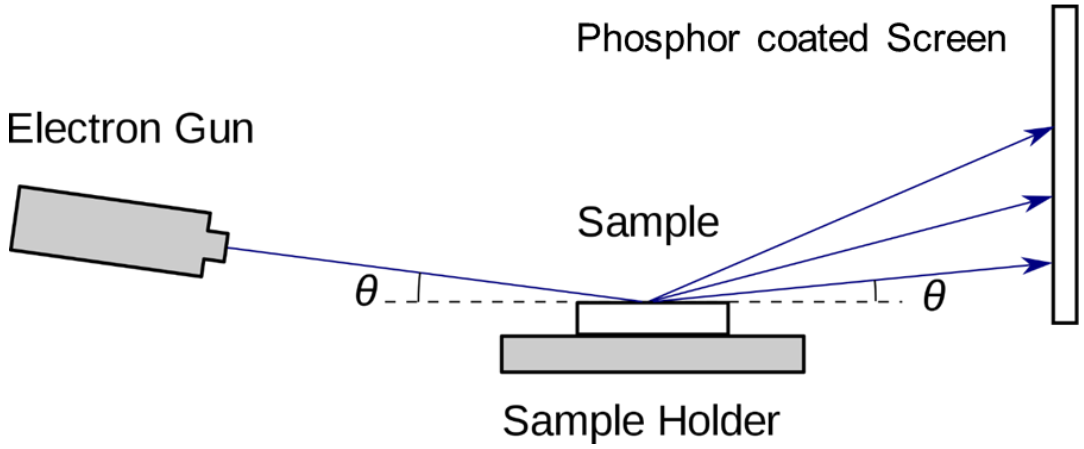

Figure 2.5. Schematic of the RHEED setup

On the other hand, by going to higher energies, the RHEED pattern is compressed by a factor proportional to the square root of the energy, such that the greater number of Laue zones can be observed. Thus, the typical optimal operation energy is set between 10 to 20 keV. RHEED screen is a fluorescent screen that consists of a phosphor covered, indium-tin-oxide coated Pyrex disk [54]. The indium-tin-oxide coated Pyrex disk is used to prevent the charging effect. A monitor or camera is installed in front of the RHEED screen to capture the RHEED pattern in real time. This allows not only the observation of the RHEED pattern during growth but also the measurement of the RHEED intensity oscillation to calibrate the growth rate of specific element or compound.

To understand the basics of RHEED, several assumptions are made: electron collisions are elastic, electrons do not penetrate deep into the material, electrons heaving as wave, and the material's width is large compared to the coherence length of the electron beam [55]. To understand the physics of RHEED pattern, let's consider the Von Laue formulation and the Ewald construction, where Laue condition and conservation of energy gives [56]

$$\Delta \mathrm{k} = \mathrm{k_i} - \mathrm{k_o} \tag{2.2}$$

Where k_o is the incoming momentum of the diffraction electron from a lattice plane and k_i is the outgoing momentum of the electron. We will expect the amplitude of the incoming and outgoing momenta to be the same such that:

$$|\mathrm{k_i}| = |\mathrm{k_o}| \tag{2.3}$$

Given that the sphere is an Ewald sphere, (which is defined as a sphere that has a radius of $|k_o|$), the intersection of this sphere with the reciprocal lattice from the sample will result in the pattern that will be seen on the RHEED screen as show in Figure 2.6. As a result, for a perfectly flat sample, we will have an infinite 2D square lattice such that the infinite rods perpendicular to the sample will intersect with the Ewald sphere, resulting in a pattern of concentric dots [55]. Similarly, what we typically observe in a Heusler compound is a flat surface with small domains, resulting in infinite rods that have a finite width. This results in a RHEED pattern that is a streak rather than spots.

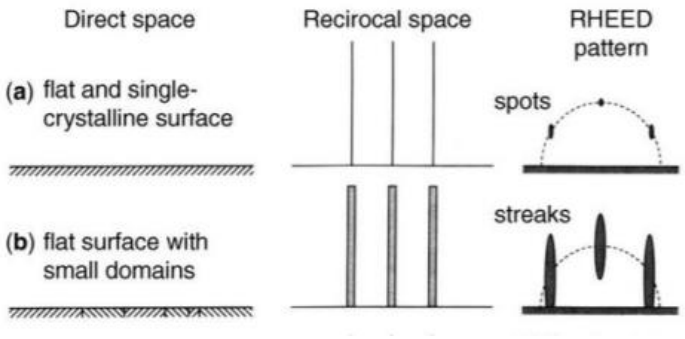

Figure 2.6 The two different RHEED patterns that were typically observed for Heusler compounds, where only the lowest Laue zone is shown. Image reprinted from [55].

2.5 High Resolution X-ray diffraction

High Resolution X-ray diffraction, commonly known as HRXRD, is a technique for the non-destructive analysis of mostly layered, nearly perfect crystalline structured materials. This technique is commonly used to study material properties such as lattice constant, crystal phases, and film morphology. In this dissertation, a few key features will

be covered here A comprehensive description of x-ray diffraction can be found in reference [57]. Starting with the instrumentation, x-ray diffraction is typically composed of three main components: the x-ray source, the detector, and the goniometer stage where the sample rests. Starting from the x-ray source, which a Cu $K_{\alpha 1}$ X-ray with a wavelength of $\lambda = 1.540598$ Å is used for the study of this dissertation, the x-ray beam is emitted and collided with the target sample that is affixed on the goniometer. The goniometer (or the detector and the source) carefully varied angles between the source, sample, and the detector while recording the diffracted X-rays intensity entering the detector. The interaction of the incident x-rays with the sample produces constructive interference (and a diffracted ray) when conditions satisfy Bragg's Law. This allows for the study of the lattice constant from the diffraction angle as well as crystal quality by linewidth of the peak. In addition, the presence or absence of certain peaks can be used to determine crystal type, reaction phases, as well as defect phases.

In order to understand the physics of x-ray diffraction, we need to start by understanding Bragg's Law. When an x-ray beam interacts with the electrons around an atom, it can either be absorbed which causes an electron to be ejected from the atom or the x-ray beam can scatter. However, when an x-ray beam enters a sample there will be additional complexity due to the fact that atoms in crystal are periodic, which means the scattered wave from each of the scattering points can result in a constructive or destructive interference. The general relationship between the wavelength of the incident x-ray, angle of incidence, and spacing between the crystal lattice planes of atoms can be determined by Bragg's Law for constructive interference [57]

$$n\lambda = 2d\sin\theta \tag{2.4}$$

Where n is the order of reflection, λ is the wavelength of the incident x-ray, d is the interplanar spacing of the crystal, and θ is the angle of incidence. However, as previously discussed, in order to satisfy Bragg's law for constructive interference, a very powerful and useful way of representing the stratifying of the Bragg's law is given by the Ewald construction, which is essentially Bragg's law constructed in reciprocal space. It can be first determine the reciprocal vectors $b_1 b_2 b_3$ of the crystal axes $a_1 a_2 a_3$ by

$$b_1 = \frac{a_2 \times a_3}{a_1 \times a_2 \times a_3}, b_2 = \frac{a_1 \times a_3}{a_1 \times a_2 \times a_3}, b_3 = \frac{a_1 \times a_2}{a_1 \times a_2 \times a_3} \tag{2.5}$$

Where each reciprocal lattice vector is perpendicular to the plane defined by the two crystal axes having different indices. With these conditions, it can be determined that

$$a_i \cdot b_j = \begin{cases} 1, i = j \\ 0, i \neq j \end{cases} \tag{2.6}$$

Now, to determine the distance between the *hkl*-planes d_{hkl}, a vector H_{hkl} in terms of the reciprocal vector can be define such that

$$H_{hkl} = hb_1 + kb_2 + lb_3 \tag{2.7}$$

By using the relationship from eq. (2.6), the spacing of the *hkl*-planes d_{hkl} can be written as

$$d_{hkl} = \frac{a_1}{h} \cdot \frac{hb_1 + kb_2 + lb_3}{|H_{hkl}|} = \frac{1}{|H_{hkl}|} \tag{2.8}$$

This result shows that the vector H_{hkl} is perpendicular to the plane hkl and the length is equal to the reciprocal of the spacing. Now, in order to understand the diffraction conditions of a real crystal with different atoms at each atomic site, a property known as

the structure factor *F* is used since it is only in the structure factor that the atomic position appears, which is given by the equation [57]

$$F = \sum_n f_n e^{(2\pi i/\lambda)(k-k_o)\cdot r_n} \quad (2.9)$$

The derivation of the equation will not be discussed here and can be found in reference [57]. The important conclusion here is that by evaluating the structure factor of the atoms in the specific structure, systematic absences of diffraction peaks can be used to determine the space group symmetry and crystal type. The structure factors used in this work were calculated using the VESTA software package and will become an important factor in determining the crystal ordering of the L_{21} Heusler ordering in the later section.

2.5.1 Reciprocal space mapping

Instead of measuring a one-dimensional slice of reciprocal space, a two-dimensional slice of reciprocal space can also be taken. This two-dimensional measurement in X-ray diffraction is known as reciprocal space mapping (RSM). Since a two-dimensional slice of the reciprocal space can be taken, it means that it can help determine the exact position, size, and shape of the reciprocal space points compared to that of the one-dimensional XRD. This is commonly used to determine quantitative information on strain, strain-relaxation, shear, as well as dislocation density in a thin film [58, 59]. In order to obtain a reciprocal space mapping, a triple axis diffractometer is used [60]. The triple axis diffractometer mechanically rocks the second axis that contains the sample through a range of incident x-ray angles while additional rocking angle is measured

on the third axis. This allows precise measurement of both rocking angle and scattering angle in order to map out high resolution reciprocal space mapping [60]. However, one of the biggest disadvantages when it comes to reciprocal space mapping is the long data collection time since it requires multidimensional reciprocal space data in order to piece together the mapping. Reciprocal space mapping has been one of the primary tools for developing for strain engineered films. It can be used to determine lattice mismatching, relaxation, lattice strain, and lattice constant in a multilayer thin film [61]. Studies such as study of strain and relaxation of $Si_{1-x}Ge_x$ growth on Si substrates by MBE growth [62], study of biaxial strain in $(11\bar{2}0)$ plane $In_xGa_{1-x}N$/GaN layers [63], and many more have shown the high precision results that allow for the understanding of strain effect in multiplayer thin films.

However, for this study, the reciprocal space mapping is mainly used to understand the signal of an off-axis Bragg reflection peak that is otherwise difficult to determine on a one-dimensional diffractometer due to its limited access to the multidimensional mapping. One of the biggest challenges in growing a high quality Full Heusler thin film is determining its degree of chemical ordering. The details of the chemical ordering will be discussed in a later section. But one of the main goals of this work is to determine an optimal post-growth process to obtain the $L2_1$ ordering, which is the Full Heusler ordering.

2.6 Magnetotransport

In order to determine the electronic properties of materials such as carrier type, carrier concentrations, resistivity, carrier mobility and scattering mechanism, magnetotransport measurement using Hall Bar analysis is often utilized. Hall effect measurement is a commonly used technique that typically comes in two different sample geometries: Hall bar (which is long and narrow with length l, width w, and thickness t) and van der Pauw (nearly square or circular). The Hall effect was discovered by American physicist Edwin Herbert Hall in 1879 [64]. Hall effect can be understood as the following: current within a material is caused by the movement of many charge carriers. When there is no magnetic field present, the charge carriers move in a straight line and only changes its path through a collision with other carriers, impurities, or phonons. However, when a magnetic field is applied perpendicular to the materials in the z direction, the charge carrier will experience a force known as Lorentz force, which can be written as

$$\overrightarrow{F_L} = q\vec{v} \times \vec{B} \tag{2.10}$$

Where $\vec{v}$ is the velocity of the carrier in the *x* direction and $\vec{B}$ is the magnetic inductance in the material in the *z* direction. In steady state, the cross product of the Lorentz force result in a force that is perpendicular to both the magnetic field and the current direction. For a positive applied field, the current I (assuming the conventional "hole" current that is in the negative direction of the electron current) will bend toward the negative y direction while the electron carrier current will bend toward the positive y direction as shown in Figure 2.7, resulting in a charge built up in either side depending on the carrier type.

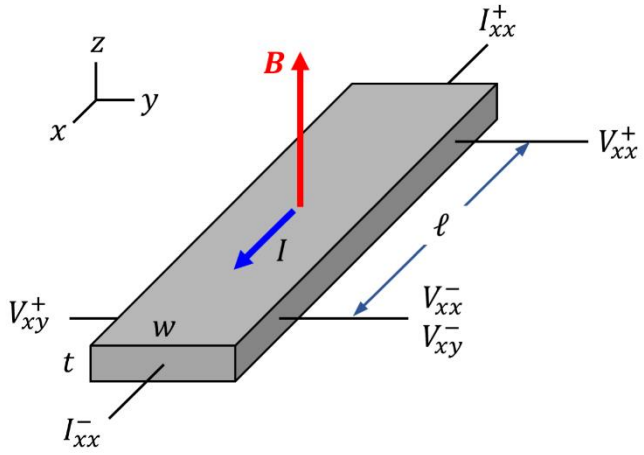

Figure 2.7. Schematic of a standard Hall bar with length l, width w, and thickness t

This charge builds up results in a voltage difference across the y direction, which is known as the Hall voltage, which can be written as

$$V_H = \frac{I_x B_z}{nte} \tag{2.11}$$

Where I_x and B_z are the current and applied magnetic field while n is the charge carrier density, t is the thickness of the sample, and e is the charge of the electron. The total resistance R_{xx} of a Hall bar can be determined by Ohm's law. The total resistance can be written as a function of sheet resistance and the dimension of the Hall bar. The sheet resistance of the thin film can be written as

$$R_{sheet} = R_{xx}\frac{w}{l} = \frac{V}{I}\frac{w}{l} \tag{2.12}$$

Thus, the total resistivity of the film ρ_{xx} in the perpendicular and applied current direction results in the following function:

$$\rho_{xx} = R_{sheet} \cdot t = \frac{V_{xx}}{I_{xx}} \frac{w}{l} t \tag{2.13}$$

Similarly, the Hall voltage V_{xy} can be normalized by the applied current to give Hall resistance and multiplied by film thickness to obtain the Hall resistivity ρ_{xy}

$$\rho_{xy} = R_{xy} \cdot t = \frac{V_{xy}}{I_{xx}} t \tag{2.14}$$

It is important to note that Hall resistivity of ρ_{xy} is not a function of the length or width but rather a function of the film thickness. This effect is known as the ordinary Hall effect which are useful to determine film properties such as carrier type and carrier concentration. However, contribution of the Hall effect typically the sum of the ordinary Hall effect (OHE) and anomalous Hall effect (AHE) contributions. In a ferromagnet, Hall resistance is usually written as

$$R_{xy} = \mu_0 (R_H H + R_{AH} M) \tag{2.15}$$

Where R_H is the ordinary Hall resistance and R_{AH} is the anomalous Hall resistance, while the H is the applied magnetic field and M is the magnetization. μ_o is the vacuum permeability. The ordinary Hall effect arises from the Lorentz force and the anomalous Hall effect originated from the intrinsic magnetization. The Hall resistance increases approximately linearly with the applied field at low field region before it tends towards the saturation at high field region. At the higher field region, a weak linear increase in ρ_H can be observed which contribute to the ordinary Hall effect [65]. By using a simple, single charge-carrier model. The Hall resistance is found by fitting a line to the high-field region far from any AHE contributions and extracting the slope, then normalizing by the current I_{xx}. Solving for bulk carrier density (n) and Hall mobility (μ_H) gives [65]

$$n = \frac{I_{xx}}{et(dV_{xy}/dB)}; \qquad \mu_H = \left(\frac{dV_{xy}}{dB}\right)\frac{l}{w}\frac{1}{V_{xx0}}, \tag{2.16}$$

Where e is the fundamental charge, t is the film thickness measured, l and w are the length and width of the Hall bar, and V_{xx0} is the longitudinal voltage value taken at zero field.

2.7 Angle-resolved photoemission spectroscopy

One of the most revolutionary measurement techniques that arouse in the past decade is that of the Angle-resolved photoemission spectroscopy (ARPES). ARPES is an experimental technique based on the photoelectric effect to determine the binding energy of photoemitted electrons. Through decades of improvements, ARPES became the main technique for probing electronic structure of solids in both the energy and momentum space. It is an extremely powerful technique when it comes to understanding exotic and complex topological materials [66-69].

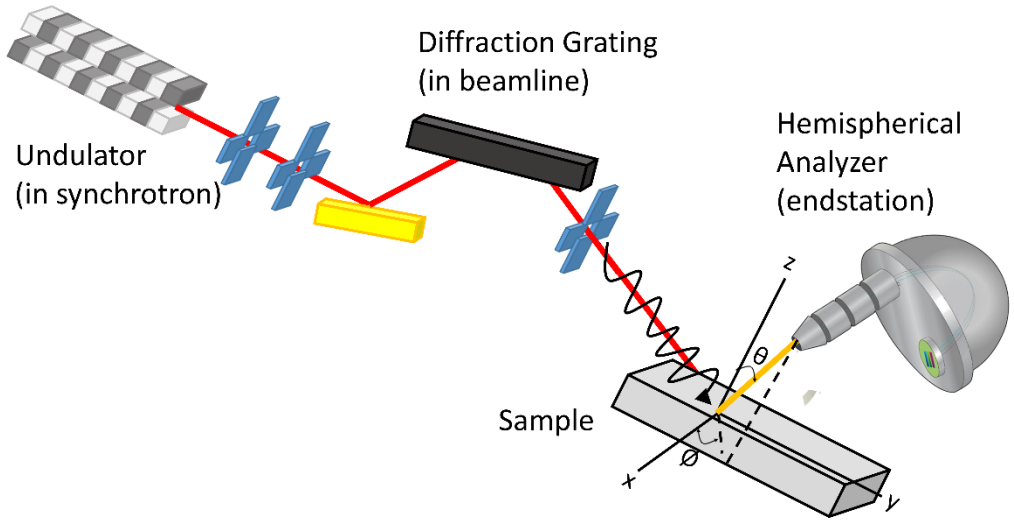

Figure 2.8: Schematic of an Angle-resolved photoemission spectroscopy

The schematic of the ARPES setup is shown in Figure 2.8. In principle, the radiation produced by an individual electron moving along a sinusoidal path is too weak for the purpose of ARPES measurement. In order to overcome such problem, a synchrotron radiation source is needed. A synchrotron facility allows the acceleration of electrons to a speed close to the speed of light. These electron bunch orbits in a large vacuum storage ring, which allows it to produce high energy electron bunch that can vary in energy from 100 MeV to 3000 MeV in a matter of seconds. These high energy electron bunches then pass through a polarized undulator. The polarized undulator is an array of permanent magnets with alternating poles which allows the electron bunches to oscillate in a sinusoidal pattern. The undulator have the advantage of providing photons with both varied energy and polarization through adjustments to the value of the gap and/or shift magnet arrays in an undulator. The high intense radiation then enters the diffraction grating, which is used to obtain a specific wavelength for the photoemission effect. The photon

radiation from the diffraction grating is targeted onto the samples and the emitted electron from the sample is then collected by the hemispherical analyzer, which is used to map out the energy and momentum space of the electrons. The hemispherical analyzer is used because the spherical symmetry of the detector can accurately preserve the angle at which the photoemitted electrons enter the detector. This allows the photoemitted electrons to dispersed in energy in the radial axis and emission angle in the transverse axis. This produced the two-dimensional image that associate with the band structure of the measured materials [68].

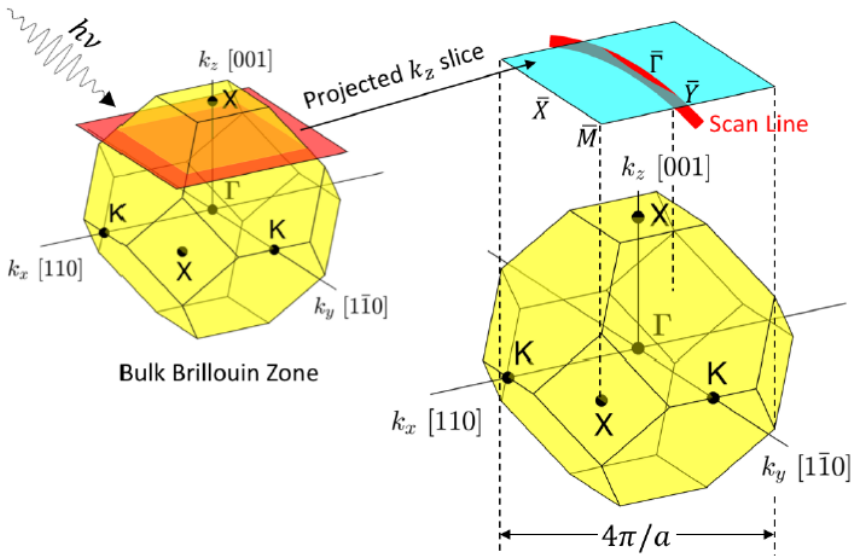

Figure 2.9: (left) photon with energy hv photoexcited electrons within the red projected k_z plane which is projected into the surface Brillouin zone (center) shown in the blue slice.

The ARPES data for the Heusler compounds are typically collected at a photon energy corresponding to its estimated bulk Γ point in the Brillouin zone. Figure 2.9 shows the Bulk Brillouin zone of the Heusler compound. Generally, a photon with hv photoexcited the electrons in the projected k_z slice of the bulk Brillouin zone at given photon energy. The work function ϕ of the sample and electron detector was determined through a photon energy sweep analysis, where the sample is measured through its estimated bulk Γ point at various photon energy. Thus, the kinetic energy of an ejected photoelectron from a given photon energy is calculated by

$$E_{kin} = hv - \phi - |E_B| \tag{2.17}$$

And the energy position of the bulk Γ position can be determined [68]

$$E_{\Gamma}^{4} = \frac{\left(k_{z,\Gamma}\right)^2 \frac{\hbar^2}{2m_e} - U_o}{\cos\left(\frac{\theta\pi}{180}\right)^2} + \phi \tag{2.18}$$

Where the m_e is the mass of the free electron, θ is the polar angel measured from sample normal, and U_o is the inner potential of the material measured. Giving that the binding energy of the electron at the Fermi level is 0. The inner potential U_o can be determined by sweeping the sample through a photon energy sweep measurement to determine the change in the band structure. However, because of the rather low resolution of the ARPES spectral density, the inner potential for the material is assumed to be close to that of the other Heusler compounds such as Co_2TiSn and Ni_2TiSn, which is about $U_o = 12$ eV [4].

The out-of-plane momentum of the free electron is [68]

$$k_z = \sqrt{\frac{2m_e}{\hbar^2}(E_{kin}\cos^2\theta + U_o)} \tag{2.19}$$

While the k_{z,Γ_n} at Γ point at n Brillouin zone is

$$\mathrm{k_{z,\Gamma_n}} = \frac{\mathrm{B_n 2\pi}}{\mathrm{l_{lattice\ constant}}} \tag{2.20}$$

Where B_n is the number of the Brillouin zone. From the equation (2.19) and (2.20), the out-of-plane momentum and energy at $\theta = 0$ at the bulk Γ point can be calculated.

The $E - k_{//}$ dispersion diagram can be measured with a single ARPES scan. This can be used to determine the dispersing features and band structures of the measured materials through its high symmetry momentum direction. However, for the topological materials which might possess Dirac cones or other topological surface states, the simple single ARPES scan that show the linearly dispersing feature might not be sufficient to convince the existing of these surface states. Instead, a Fermi map, which multiple single ARPES scans at various sample orientation across the Surface Brillouin zone is taken. This provides the dispersion map of the full surface Brillouin zone to identify topological features such as Fermi arc [69].

However, Fermi mapping, where multiple line scans taken at different sample orientations are combine together to produce a complete energy dispersion map of the surface Brillouin zone, is an extremely time-consuming process since surface Brillouin zone only contains bulk states from a single value of photon energy, the full picture of the Fermi mapping is required to be measured at various photon energy. This will generally result in at least several days of continuous scanning without interruption. In addition,

surface degradation of the measured material can often be observed in several hours of measurement from beam damaged. As a result, it is often impossible scan the entire bulk Brillouin zone. Though the Fermi mapping of the Full bulk Brillouin zone is difficult, it is still possible to separate the features between a bulk and surface states. Electronics sates confined to the surface do not disperse in the out-of-plane direction. Thus, surface states should appear constant as a function of photon energy, while the bulk sates will disperse with photon energy. This photon energy sweep of the linearly dispersed surface states will provide additional confidence in order to separate the bulk states from the surface states of the materials.

2.8 Magnesium oxide substrate preparation

Magnesium oxide (MgO) substrate has been used for a large fraction of the study in this dissertation. MgO is a rocksalt crystal structure with lattice parameter of 4.212 Å. MgO is widely used for many Heusler compounds due to its relatively small lattice mismatch when the thin film is grown in a 45° rotation about the [001] axis, which has an effective lattice constant of 5.957 Å. However, commercially available MgO substrates have several shortcomings when it comes to its crystal quality. MgO substrates, have substantially worse crystal quality than III-V substrates due to high degree of mosaicisity and crystal twinning. These defects will affect the over-grown thin film quality. In addition,

MgO is also hygroscopic and absorption of water from the atmosphere can often be trapped within the MgO surface. As a result, multiple processes are needed.

The MgO (001) substrates were first annealed at 800 ˚C for 12 hours in 3.00 Standard Liter per minute N_2 and 3.00 Standard Liter per minute O_2 in a tube furnace in the UCSB Nanofabrication Facility. The sample is then loaded into the load lock of the ultra-high vacuum (UHV) interconnected growth and characterization system with a base pressure of $< 1x10^{-10}$ torr. The MgO substrates were annealed *in-situ* at 700 °C for 1 hour prior to growing an epitaxial 20 nm MgO buffer layer at a substrate temperature 630 °C by e-beam evaporation of MgO crystals at a rate of 1 nm per minute. Lastly, the surface morphology is examined with RHEED in the growth chamber to ensure a good starting surface.

Chapter 3

Growth and Characterization of Weyl Semimetallic Half-Metal Co_2TiSn

3.1 Introduction

Topological materials are a new state of quantum matter that have attract lots of attention within the research field for its promising applications such as more energy-efficient microelectronic components, better catalysts, improved thermoelectric converters,

new magnetic storage, and many more [70-75]. But more recently, another class of topological materials also known as the Weyl semimetal, was first discovered in TaAs [76-79]. After the first discovery of the Weyl semimetal materials, many other theoretical works from different groups have been putting their focus in determining other potential candidates within this family. One potential candidate fell under the Heusler family. The Full Heusler half-metallic Co_2TiZ (Z = Si, Ge, Sn) has been recently theorized to be a potential candidate to possess the time-reversal breaking Weyl and nodal line semimetallic behaviors [7]. This chapter will focus on the study of the Co_2TiSn thin film. Co_2TiSn was first studied in bulk crystal form due to its half-metallic properties with a minority spin gap of around 0.5 eV [80]. However, thin film growth as well as its semimetallic properties have not been thoroughly studied. In order to examine its Weyl semimetallic behavior within this system, understanding its electronic structure becomes an important goal.

In order to achieve this goal, one needs to understand the influence of the chemical ordering of the Co_2TiSn. The chemical ordering of the Full Heusler compound may play an important role in preserving the Weyl semimetallic behavior [7]. None of the studies up until now have focused on determining the degree of chemical ordering of Co_2TiSn. One method to achieve high degree of $L2_1$ ordering could be to utilize high temperature post-growth thermal annealing process. Many studies of other compounds such as Cu_2MnAl [81], $Co_2FeAl_{0.5}Si_{0.5}$ [82], and Co_2MnSi [83] have shown increase in the $L2_1$ ordering and magnetic properties using post growth thermal annealing. Furthermore, achieving a high degree of $L2_1$ ordering is important as it has been shown to affect the intrinsic properties of the materials [84-86]. For example, in Heusler Weyl semimetal materials such as

Co_2MnAl, it was shown that a B2-ordered Co_2MnAl resulted in a reduction in anomalous hall conductivity, magnetoresistance, and Berry curvature contribution originated from the Weyl point compared to those $L2_1$-ordered Co_2MnAl in both theoretical prediction and experimental result [84]. Thus, it is important to not only understand the growth of the Co_2TiSn but also to optimize the growth conditions for the $L2_1$ chemical ordering in order to preserve the Weyl semimetallic properties within this system.

3.2 Growth of Co_2TiSn thin film

In this study, the primary choice of substrate is the Magnesium oxide (MgO) with a (001) orientation. As previously discussed in section 2.8, MgO has an effective lattice constant of 5.957 Å when the thin film is grown in a 45^o rotation about the [001] axis. From other experimental work, the experimental lattice constant of Co_2TiSn is determined to be around 6.07 Å [80]. The predicted epitaxial relationship for Co_2TiSn [100] (001) // MgO [110] (001) is shown in figure 3.1 with a 1.8% compressive lattice mismatch for the Heusler. The lattice mismatch between the Co_2TiSn thin film and MgO substrate is relatively small. In addition to its relatively small lattice mismatch, its thermal stability as well as being a good insulator make MgO an ideal substrate for epitaxial growth and eliminating parallel conduction from electrical measurements.

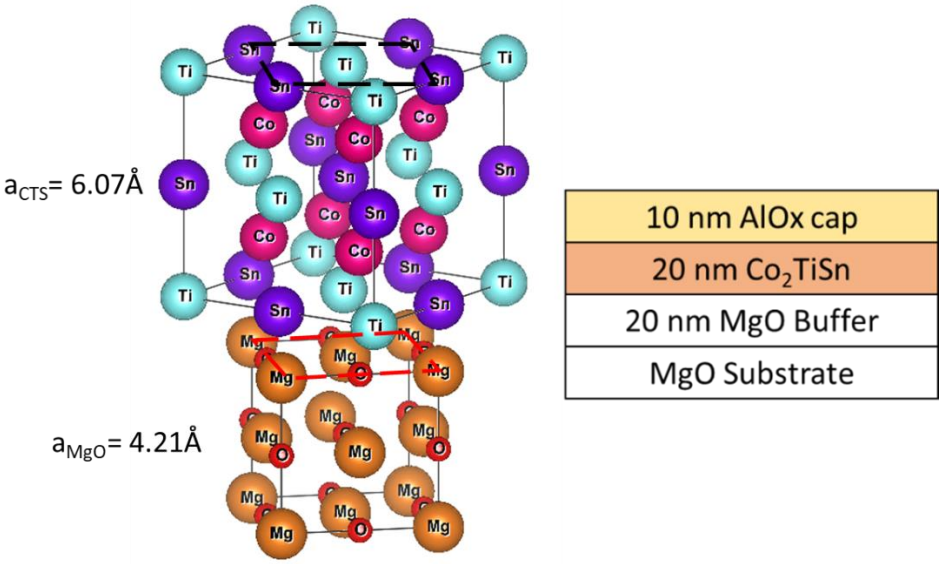

Figure 3.1. (left) crystal structure and epitaxial relationship for Co_2TiSn [100] (001) // MgO [110] (001). (right) the growth structure of the Co_2TiSn thin film on MgO buffers. The surface unit cell indicated by the black dotted line (Co_2TiSn) and red dotted line (MgO) with axes along the bulk <100> and <010> axes is shown.

The preparation of the MgO substrate started with 12 hours annealing at 800 ˚C in a tube furnace in an N_2/O_2 atmosphere before loading it into the load lock of the ultra-high vacuum (UHV) interconnected growth and characterization system with a base pressure of $< 1x10^{-10}$ Torr. The MgO substrates were annealed in-situ at 700 °C for 1 hour prior to growing an epitaxial 20 nm MgO buffer layer at a substrate temperature 630 °C by e-beam evaporation of MgO crystals. Following the MgO buffer layer growth, the samples were transferred into a VG V80 MBE growth chamber with a base pressure $< 1x10^{-10}$ Torr for the Co_2TiSn growth. The growth of the Co_2TiSn thin film was accomplished by co-depositing 4N high purity elemental Ti and 5N high purity elemental Co and Sn from

individual effusion cells. The Ti effusion cell is a specialized high temperature cell from DCA instruments Oy [87], which use a proprietary crucible that allows liquid titanium to be evaporated with a maximum operating temperature of 2000 °C. The atomic fluxes as a function of cell temperature were calibrated by the measurement of elemental atomic areal density of each element for films grown on silicon substrates using Rutherford backscattering spectrometry (RBS). These measurements were also used to calibrate the beam flux monitor for each cell. For each RBS sample, two to three elements were co-deposited ensuring that there was no overlap of their peaks in the RBS energy spectra. Typically, three sets of samples for each element were measured and analyzed with the results compared with previous calibrations using RUMP software [88]. Finally, the effusion cell temperatures were determined and set for a ~2 Å/min a Co_2TiSn growth rate. Figure 3.2 shows the typical substrate temperature variation during the growth for a 20 nm Co_2TiSn thick film. For this system, Ti flux is the limiting factor in growth rate as the maximum temperature of the Ti cell is set about 100 °C below the melting point. Thus, a total of around 2 hours and 20 minutes of growth time is typically required to deposit 20 nm of Co_2TiSn thin film. Various substrate growth temperatures from 300 °C to 600 °C were first examined using Reflection-high energy electron diffraction to monitor film morphology and surface reconstruction during the growth.

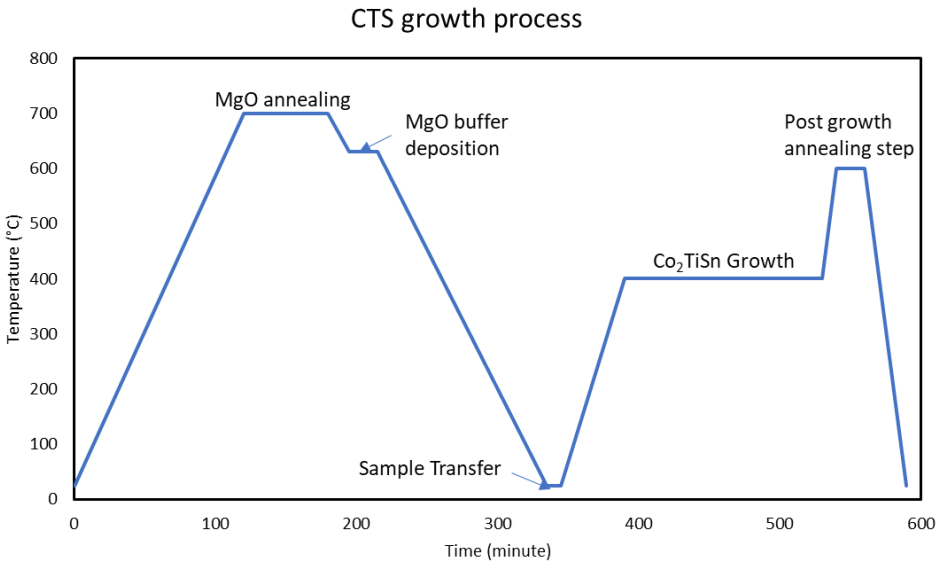

Figure 3.2. typical growth steps of Co_2TiSn thin film on MgO buffer (001)

As one can see from the left RHEED pattern of figure 3.3, the three-dimensional diffraction spots indicate that the Co_2TiSn thin film growth at a temperature of 300 °C results in 3D island growth. As growth temperature is increased, the RHEED pattern becomes less spotty and becomes streaker at around 400 °C, indicating a relatively smooth and flat surface. On the other hand, as growth temperature increase beyond 400 °C, the RHEED pattern once again becomes spotty resulting in 3D island like growth. The additional chevron features in the RHEED pattern are attributed to the formation of facets. Thus, the growth temperature of 400 °C was determined to be the optimal growth temperature for the Co_2TiSn thin film.

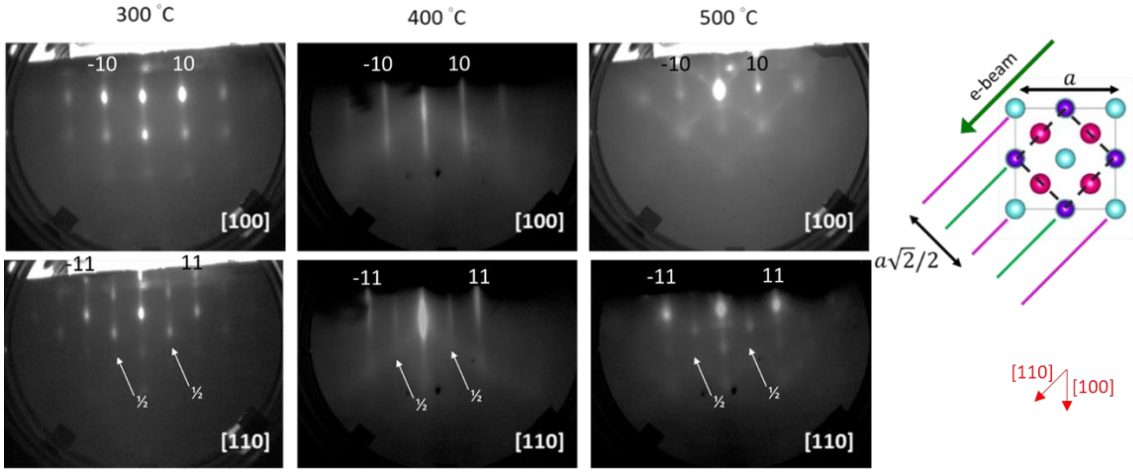

Figure 3.3. (left) RHEED pattern of 20nm Co_2TiSn thin film on MgO (001) at various growth temperatures (left) 300 °C, (middle) 400 °C, and (right) 500 °C along the Co_2TiSn [100] (001) // MgO [110] (001) and Co_2TiSn [110] (001) // MgO [100] (001). direction. (right) shows the relationship between the RHEED beam along the [110] direction of Co_2TiSn from a top-down view.

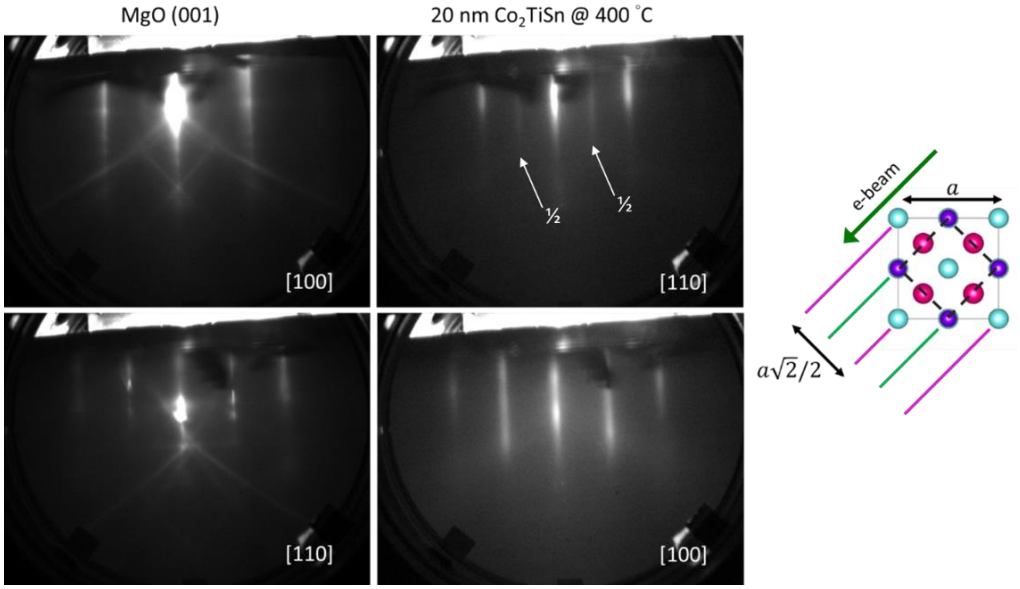

Figure 3.4. RHEED pattern of (left) a 20 nm thick MgO buffer layer on MgO (001) substrate at room temperature and (middle) the epitaxially grown 20 nm thick Co_2TiSn thin film on MgO (001) buffer layer at 400 °C.

Figure 3.4 shows a typical RHEED pattern a 20 nm thick MgO buffer layer on MgO (001) substrate at room temperature and the epitaxially grown 20 nm thick Co_2TiSn thin film on MgO (001) buffer layer at 400 °C. The grown MgO buffer shows the expected (1x1) bulk unreconstructed surface, which does not change after increasing the manipulator temperature to 400 ˚C prior to the Co_2TiSn growth. Initial growth of Co_2TiSn shows a spotty three dimensional like RHEED pattern indicating island growth. As thickness of the film increases with growth time, the RHEED pattern becomes streaker. The presence of the additional ½ order streaks as mark by the white arrow in figure 3.4 with the RHEED beam along the <110> of Co_2TiSn is consistent with an ordered Ti-Sn surface termination. This is typically observed for a full-Heusler and results from either a cobalt or Ti-Sn order terminated surface, where both will result in an effective surface unit cell that is $\sqrt{2}$ smaller and rotated 45° compared to the conventional Ti-Sn terminated surface unit cell [36]. This results in a typical c(2x2) RHEED construction that is often been observed for a full Heusler compound which is also consistent with a $L2_1$ crystal structure [89]. When the RHEED beam is along the Co_2TiSn [110] direction, the observation of the 00 and 01 specular spots are indicated by the purple line in the figure while the additional ½ order streaks are indicated by the green line. The result is a c(2x2) RHEED construction. However, observation of the $L2_1$ ordering c(2x2) RHEED construction does not indicate that the bulk crystal structure has the $L2_1$ ordering since RHEED measurement is surface sensitive.

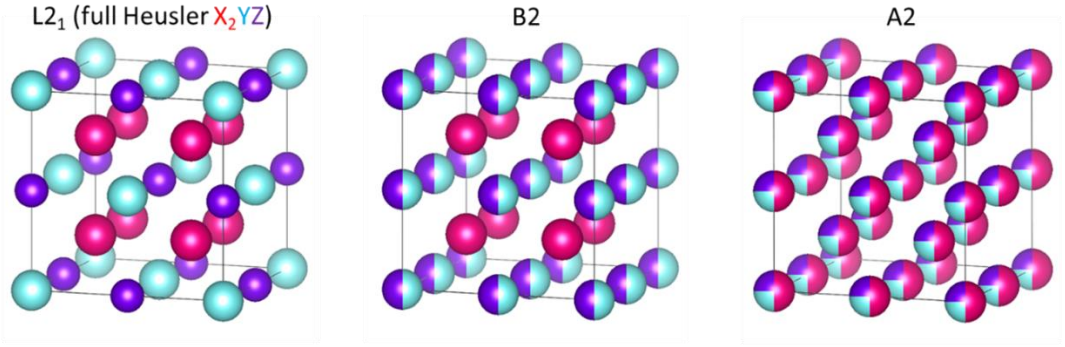

X-ray Bragg Peak structure factor calculation

h	k	l	d (Å)	|F|	2θ	I
1	1	1	3.34	3.99E+01	26.64	17.92%
2	0	0	2.90	4.06E+01	30.86	5.98%
2	2	0	2.05	2.27E+02	44.21	100%
3	1	1	1.75	2.87E+01	52.37	8.21%
4	0	0	1.45	1.76E+02	64.30	13.80%
3	3	1	1.33	2.19E+01	70.89	3.09%

L2$_1$

h	k	l	d (Å)	|F|	2θ	I
1	1	1	3.34	1.26E-14	26.64	0%
2	0	0	2.90	4.06E+01	30.86	5.98%
2	2	0	2.05	2.27E+02	44.21	100%
3	1	1	1.75	8.33E-14	52.37	0%
4	0	0	1.45	1.76E+02	64.30	13.80%
3	3	1	1.33	4.01E-14	70.89	0%

B2

h	k	l	d (Å)	|F|	2θ	I
1	1	1	3.34	3.06E-14	26.64	0%
2	0	0	2.90	7.21E-14	30.86	0%
2	2	0	2.05	2.27E+02	44.21	100%
3	1	1	1.75	4.27E-14	52.37	0%
4	0	0	1.45	1.76E+02	64.30	13.80%
3	3	1	1.33	4.51E-14	70.89	0%

A2

Figure 3.5. 3 different types of chemical order in Full Heusler compound X_2YZ and the corresponding X-ray Bragg peak and intensity *I* for each chemical ordering of Co_2TiSn shown in the table calculated using VESTA software [108].

Co_2TiSn possess the three different chemicals order of the Full Heusler compound: $L2_1$, B2, and A2 ordering. Figure 3.5 presents the results of peak intensities at different Bragg peak based on the structure factor calculation for the 3 different ordering of Co_2TiSn. Taking the $L2_1$ structure as the crystallographic basis, a (004) Bragg peak indicates at least partial A2 order, a (002) peak indicates at least partial B2 order, and a (111) peak indicates at least partial $L2_1$ order. Structure factor can be written as the following:

$$F(hkl) = \sum_n f_n e^{2\pi i(hx+ky+lz)} \tag{3.1}$$

Where $F(hkl)$ is the resultant of all waves scattered in the direction of the *hkl* reflection by the n atoms contained in the unit cell and f_n is the atomic scattering factor that is

independent of the position of the atom in the unit cell [53]. The $|F(hkl)|$ gives the scattering amplitude of the specific *hkl* reflection while the modulus squared $|F(hkl)|^2$ gives the scattering intensity that is proportional to measured peak intensity I such that [53]

$$I_{hkl} = PLA|F(hkl)|^2 \tag{3.2}$$

Where P is the polarization factor, L is the Lorentz factor, and A is the factor that accounts for the loss of intensity from single scattering in the sample. For the case of Co_2TiSn as shown in figure 3.5, $L2_1$ is the expected full-Heusler ordered phase while disorder between the Ti and Sn atoms would give B2 order and complete chemical disorder for Co, Ti, and Sn would give A2 order. Noticeably, the (111) Bragg peak intensity only present for the case of $L2_1$ ordering structure. Thus, in order to examine the degree of $L2_1$ ordering, the (111) Bragg peak is chosen as the peak intensity to identify the ordering of the thin film.

Figure 3.6 (left) shows the typical XRD of the 20nm Co_2TiSn thin film after growth at 400 ˚C. The expected (002) and (004) Co_2TiSn reflection are observed with no additional diffraction peaks, which suggests no additional phases presented in the measurement. However, the crystallinity of the film is rather poor because of its large FWHM as well as small (002) reflection intensity. From the structure factor calculation shown in figure 3.5, it is expected that the intensity of the (002) reflection to be about 43% of the (004) reflection intensity for a $L2_1$ order Co_2TiSn thin film. Evidentially, the resulting (002) reflection intensity is much smaller than what would be expected for a $L2_1$ order Heusler compound. Similarly, the line scan of the Co_2TiSn (111) Bragg peak as shown on the right

of figure 3.6 also indicates extremely weak intensity of the (111) Bragg peak where the peak intensity is close to the background of the measurement itself.

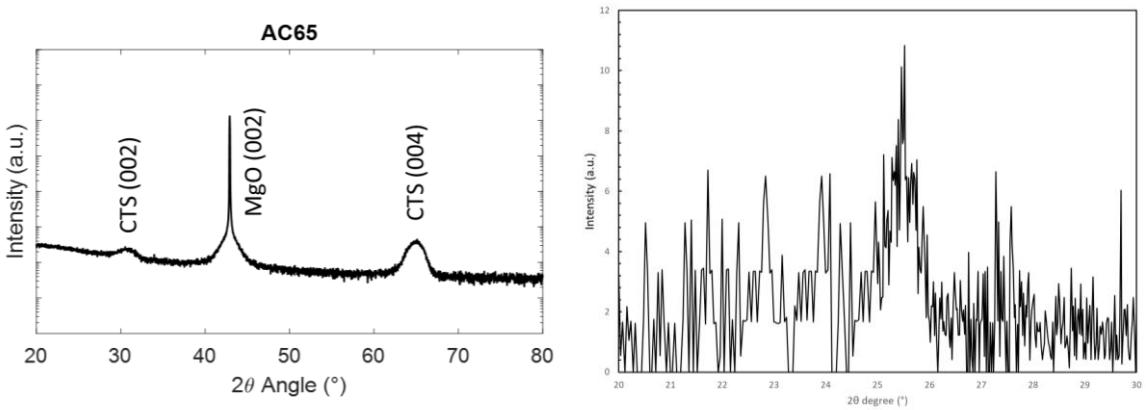

Figure 3.6. (Left) XRD of the epitaxially grown 20 nm thick Co_2TiSn on the MgO (001) buffer layer at 400 ˚C with no post-growth annealing process. (Right) normalized line scan of the Co_2TiSn (111) Bragg peak.

Co_2TiSn has shown the expected c(2x2) RHEED construction, but weak to almost no intensity of the (111) Bragg peak can be measured. This indicates that the Co_2TiSn thin film grown at 400 ˚C without any post-growth annealing process is likely to be dominated by B2 ordering. Thus, in order to synthesize $L2_1$ order Co_2TiSn thin film, post-growth annealing process is required.

3.3 Study of $L2_1$ ordering of Co_2TiSn using XRD-RSM

Co_2TiSn thin films were grown at a substrate temperature of 400 ˚C with various post-growth annealing temperatures and annealing times to identify the optimal post growth annealing process to obtain the $L2_1$ full-Heusler ordering. Reflection-high energy electron diffraction (RHEED) was used to monitor film during growth and post-growth annealing. Following the growth, the growth chamber manipulator heater was ramped at a rate of 25 ˚C/min to the target annealing temperature. The temperature range of 400 to 600 ˚C was chosen for the annealing temperature and the annealing time varied between 10 min to an hour. After the annealing, the samples were cooled to room temperature in the growth chamber by switching off the heater power at the end of the annealing process before being transferred to another UHV chamber. Next, a 10 nm AlO_x protective capping layer was deposited via e-beam evaporation of Al_2O_3 at room temperature to prevent oxidation after the samples were loading out of the UHV system.

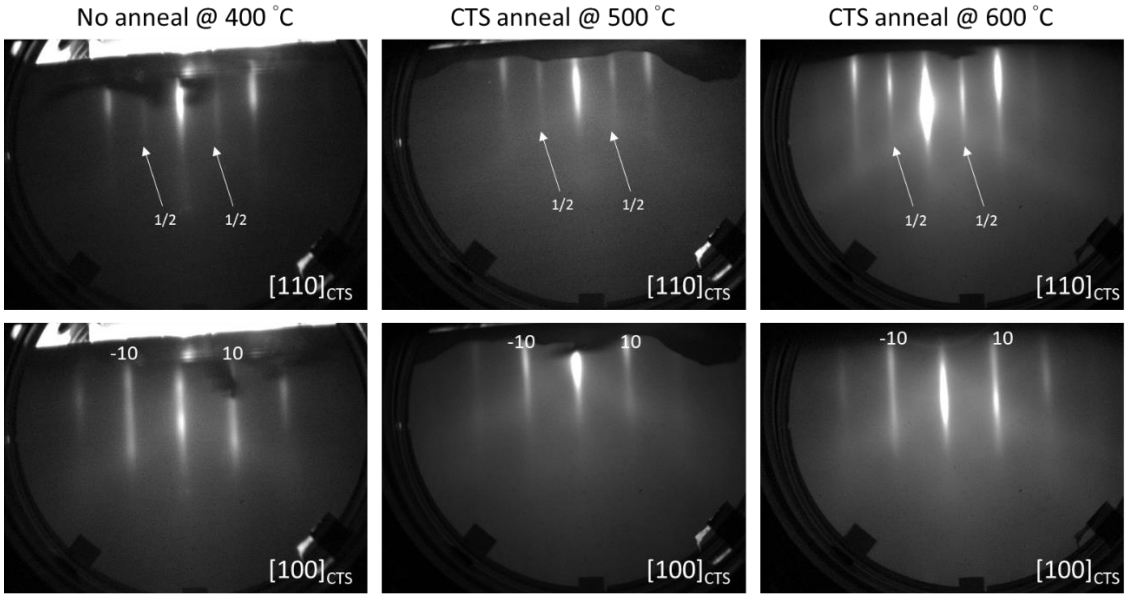

Figure 3.7. typical RHEED of 20nm Co_2TiSn thin film (left) grown at 400 ˚C with no post-growth annealing process, (middle) post growth annealing at 500 ˚C, and (right) post growth annealing at 600 ˚C for 20 minutes.

Figure 3.7 shows the typical RHEED of 20nm Co_2TiSn thin film grown at 400 ˚C with no post-growth annealing process, post growth annealing at 500 ˚C, and post growth annealing at 600 ˚C for 20 minutes. The expected c(2x2) RHEED construction can be observed at all post-growth annealing temperature up to 600 ˚C. However, because of the slight variation in the manipulator angle, it is hard to compare the change in the intensity of the specular spot. Nonetheless, it can be seen that the specular peaks become the sharpest at 600 ˚C annealing temperature, while annealing temperature above 600 ˚C does not show additional improvement in the RHEED pattern. Instead, additional spots around the (00) specular spot can be observed when sample is annealing above 600 ˚C. This means that sample of Co_2TiSn thin films that were annealed too hot can result in formation roughening

and surface faceting. The improvement in the crystallinity and ordering of the Co_2TiSn thin film after post-growth annealing process can also be observed through XRD and XRD Reciprocal space map (RSM). Figure 3.8 shows the XRD and XRD RSM of a 20nm Co_2TiSn thin film grown at 400 ˚C and annealed at 600 ˚C for 20 minutes. The XRD of a 20nm Co_2TiSn thin film grown at 400 ˚C and annealed at 600 ˚C for 20 minutes shows the expected (002) and (004) reflection in the XRD with the lattice constant calculated to be around 6.03 Å, which is closely matched with the lattice constant measured from the literature [80].

No additional peaks were observed suggesting that the samples that were grown are single phase Co_2TiSn. In addition, from figure 3.5, it was known that the peak area ratio between the (002) and (004) Bragg peak is calculated to be 0.43. The peak area ratio of the (002) and (004) Bragg peak from figure 3.8 is approximately 0.45 which agrees well with the expected peak ratio for the $L2_1$ ordering Co_2TiSn thin film. Similarly, the observation of Heusler (224) Bragg peak (peak that can be observed with any ordering of the Heusler compound) as well as the (111) Bragg peak (only observed with Co_2TiSn that possess $L2_1$ ordering) can be seen in the XRD RSM mapping show in figure 3.8.

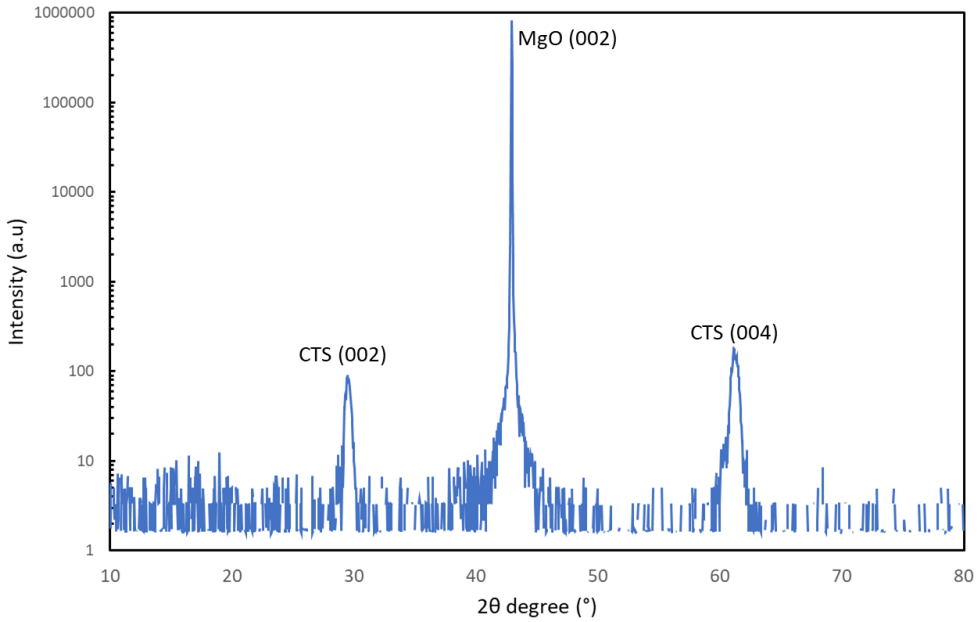

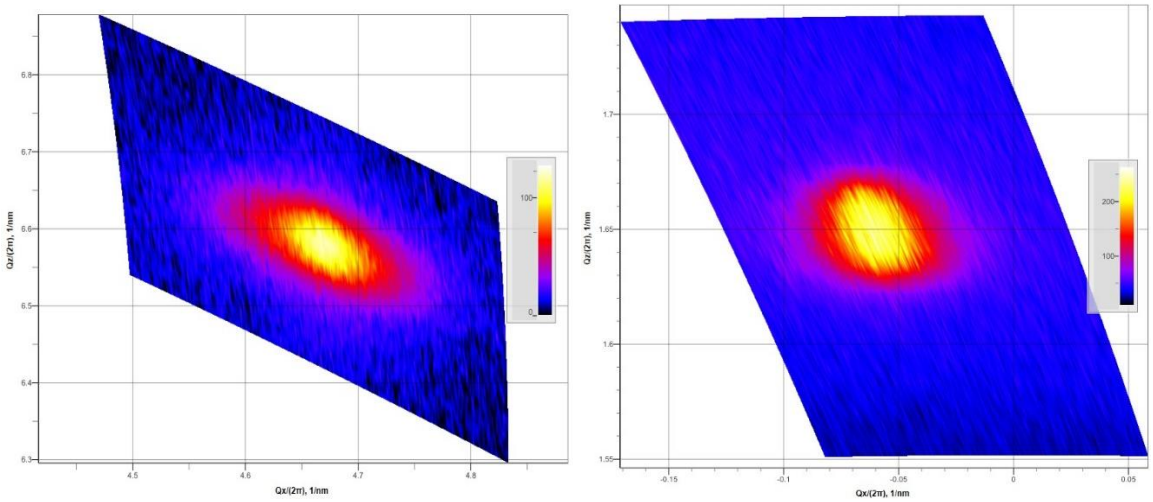

Figure 3.8. typical XRD of 20nm Co_2TiSn thin film (top) grown at 400 ˚C and post growth annealing at 600 ˚C for 20 minutes and the XRD RSM mapping of (bottom left) Heusler (224) Bragg peak and (bottom right) Heusler (111) Bragg peak of the same sample.

However, the degree of the ordering cannot simply be determined by visualization of the peak intensity from the RSM as the color intensity of the RSM data can be misleading. Thus, we also measure and plot out the line scan of the XRD of the (111) Bragg peak of Co_2TiSn thin film grown at 400 ˚C with no post-growth annealing process, post growth annealing at 500 ˚C, and post growth annealing at 600 ˚C for 20 minutes for comparison, which is shown in figure 3.9. Evidently, the intensity of the (111) Bragg peak increases with increasing annealing temperature up to 600 ˚C, meaning an increase in chemical ordering of the Co_2TiSn thin film. the maximum intensity as well as the FWHM between the 600 ˚C and 650 ˚C is roughly the same. In addition, as we can see from figure 3.5, the (111) Bragg peak is expected to be higher than that of the (004) Bragg peak.

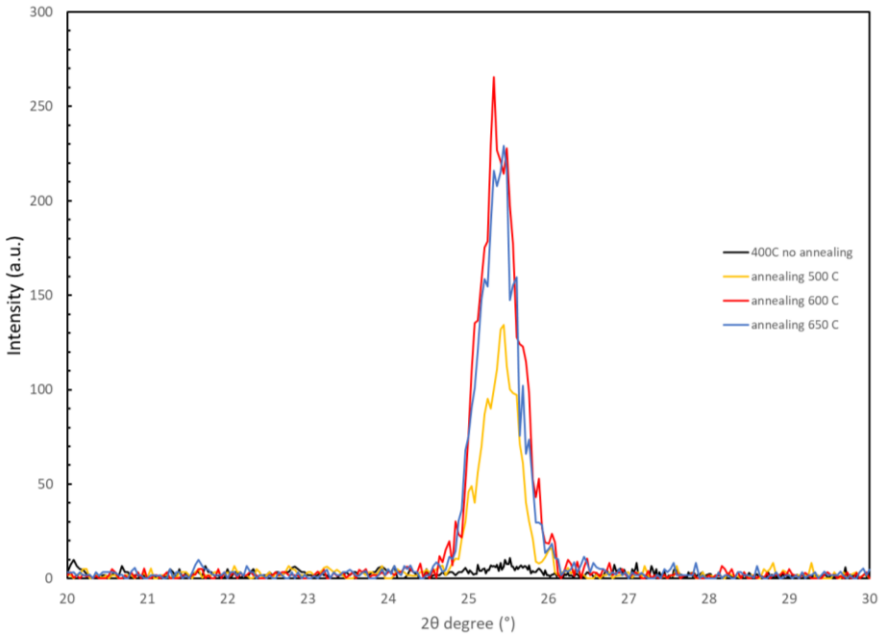

Figure 3.9. Line scan of XRD-RSM data for post-growth annealing temperature for 20 nm Co_2TiSn thin film on MgO (001) from 400 ˚C to 650 ˚C. The peak intensity of each individual measurement is normalized using the half maximum intensity calibration done at the beginning of each XRD calibration step for each XRD and XRD-RSM measurement.

The peak intensity ratio between the (111) peak of the 600 ˚C annealed sample and (004) Bragg peak is roughly about 1.34 compared to the calculated value from structure factor, which is 1.30. However, because of the observation of the additional specular spots that can be seen from the RHEED measurement at the 650 ˚C annealing temperature, we determine that most optimal growth condition to be 600 ˚C and 20-minute annealing time to obtain the highest $L2_1$ ordering for the Co_2TiSn thin films.

3.4 Magnetic and Transport properties

3.4.1 Magnetic properties

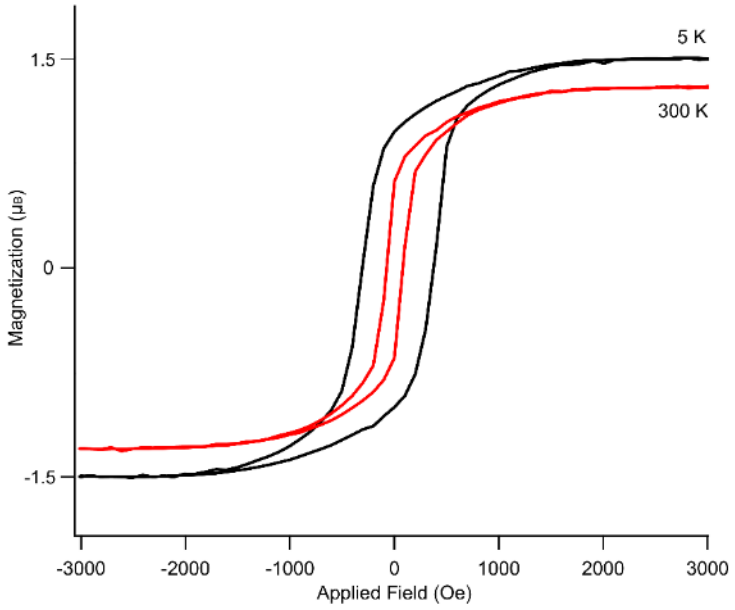

Figure 3.10: Magnetic hysteresis loops of the 20 nm Co_2TiSn/MgO (001) film as measured by SQUID. Magnetic field is applied parallel to the [110] axis

With the $L2_1$ order Co_2TiSn thin films, it will be important to examine its magnetotransport and electrical properties to determine if the Weyl semimetallic properties are present in the $L2_1$ Co_2TiSn thin film. Figure 3.10 shows the temperature dependent magnetization data normalized to sample volume determined using X-ray reflectivity (XRR) and photographic area measurements for the Co_2TiSn thin film. The magnetic field is applied parallel to the [110] direction of the sample. The coercive fields in the easy axis of [110] direction at $T = 5K$ and $300K$ are 342 Oe and 108 Oe, respectively. In addition, the saturation magnetization at $T = 5K$ of $M_S = 1.43\ \mu_B$ and $T = 300K$ of $M_S = 1.17\ \mu_B$ in Bohr Magneton formula unit, which agrees well with the literature [90].

3.4.2 Temperature dependent resistivity

Figure 3.11 shows the temperature dependent resistivity for Co_2TiSn thin film. Co_2TiSn is a half-metallic ferromagnet. Thus, to model the resistivity behavior of this system, it will be ideal to started with the resistivity of a ferromagnet material. Generally, we start with the resistivity function such that [91]

$$\rho_{xx} \approx \rho_{impurity} + \rho_{e-e}(T) + \rho_{e-p}(T) + \rho_{e-m}(H,T) \tag{3.3}$$

Where $\rho_{impurity}$ is the resistivity contribution from the electron impurity scattering, $\rho_{e-e}(T)$ is the resistivity contribution from the electron-electron scattering, $\rho_{p-e}(T)$ is the resistivity contribution from the electron-phonon scattering, and $\rho_{e-m}(H,T)$ is the resistivity contribution from the electron-magnon scattering, which depends on both

temperature and applied magnetic field. Since the magnetic properties of the Co_2TiSn are dominated by Co, we can consider using a strong 3*d* ferromagnets as the model [91].

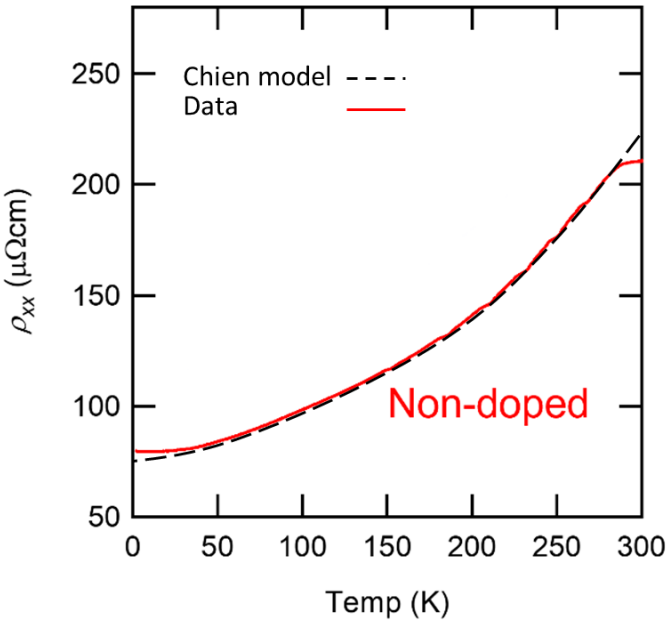

Figure 3.11: Resistivity vs. temperature for 20-nm-thick Co_2TiSn/MgO (001) film. The red line shows the experimental data, and the dash black line shows the fit to Chien model [94].

The interaction of the electron-electron and electron phonon scattering are driven by *s-d* interaction based on Baber derivation [92]. The electron-electron scattering can be simplified to a function of T^2 and electron-phonon scattering can be simplified to a function of T^5 contribution. The effective term a_{e-e} is the magnitude of electron-electron scattering to a function of T^2 and b_{e-p} is the magnitude of electron-phonon scattering to a function of T^5. Thus, equation 3.3 can be simplified to

$$\rho_{xx} \approx \rho_{impurity} + a_{e-e}T^2 + b_{e-p}T^5 + \rho_{e-m}(H,T) \qquad (3.4)$$

Now, for a 3*d* ferromagnet, the electron-magnon scattering contribution can be derived from the formalism developed by Goodings [93]. This expression is derived for an expression of the magnetic resistivity in strong ferromagnetic metals based on intraband [s-s, d-d] and interbond [s-d] spin-flip transition due to electron-magnon scattering [85]. The resulting electron-magnon scattering contribution can be writing as a function of temperature such that

$$\rho_{e-m}(T) = f_z(T)[1 - \alpha x^2] \tag{3.5}$$

When there is no applied field is present. Here, $f_z(T)$ is an arbitrary function that depends on the temperature from the electron-magnon scattering while α is the constant contribute to the fractional magnetization [91, 94]. The resulting resistivity function that depends on only temperature is given as the Chien model [94],

$$\rho_{xx} \approx \rho_{impurity} + a_{e-e}T^2 + b_{e-p}T^5 + f_z(T)\left[1 - \alpha\left(1 - \beta T^{\frac{3}{2}}\right)^2\right] \tag{3.6}$$

The resulting resistivity as a function of temperature with no applied field exhibits a metallic characteristic from figure 3.11. the resistivity ρ_{xx} of 78 $\mu\Omega cm$ and 217 $\mu\Omega cm$ are obtained at temperature of 2K and 300K, respectively, which agree well with the resistivity value from other literatures [90, 95]. In addition, the fitting of Chien model shown in figure 3.11 also shows a moderately good fit between the temperature of 35 K all the way to around 270 K. Unfortunately, the measurement was only taken up to 300K while the maximum from the resistivity is beyond that of the 300K. As a result, we can only conclude that the Curie temperature of the Co_2TiSn thin film is above 300K, which agree with a Curie temperature of 355 K from the literature [96].

3.4.3 Hall resistance measurement

The Hall resistance data at 5K and 100K of a 20-nm-thick Co_2TiGe/MgO (001) is shown in Figure 3.12 can be separated into high-field and low-field regions, which correspond to ordinary Hall effect (OHE) and anomalous Hall effect (AHE) contributions. In a ferromagnet, Hall resistivity is usually written as

$$\rho_H = \mu_0(R_H H + R_M M) \tag{3.7}$$

Where R_H and R_M are the ordinary Hall and anomalous Hall coefficients, while the H and M are the magnetic field and the magnetization. μ_o is the vacuum permeability. The ordinary Hall effect arises from the Lorentz force and the anomalous Hall effect originated from the intrinsic magnetization. As we can see form figure 3.12, the Hall resistance increases approximately linearly with the applied field at low field region before it tends towards the saturation at high field region. At the higher field region, a weak linear increase in ρ_H can be observed which contribute to the ordinary Hall effect [65]. By using a simple, single charge-carrier model. The Hall resistance is found by fitting a line to the high-field region far from any AHE contributions and extracting the slope, then normalizing by the current I_{xx}. Solving for bulk carrier density (n) and Hall mobility (μ_H) gives [65]

$$n = \frac{I_{xx}}{et(dV_{xy}/dB)}; \qquad \mu_H = \left(\frac{dV_{xy}}{dB}\right)\frac{l}{w}\frac{1}{V_{xx0}}, \tag{3.8}$$

Where e is the fundamental charge, t is the film thickness measured, l and w are the length and width of the Hall bar, and V_{xx0} is the longitudinal voltage value taken at zero field. With the given results from Hall resistance measurement, the positive slope indicating hole

type carrier and the carrier concentration and mobility is calculated to be $1.31 \times 10^{22}\ cm^{-3}$ at 100 K and $1.19 \times 10^{22}\ cm^{-3}$ at 2K, while the mobility is around 1.7 $\frac{cm^2}{Vs}$ at 2K. These values corresponding to a metallic like behavior.

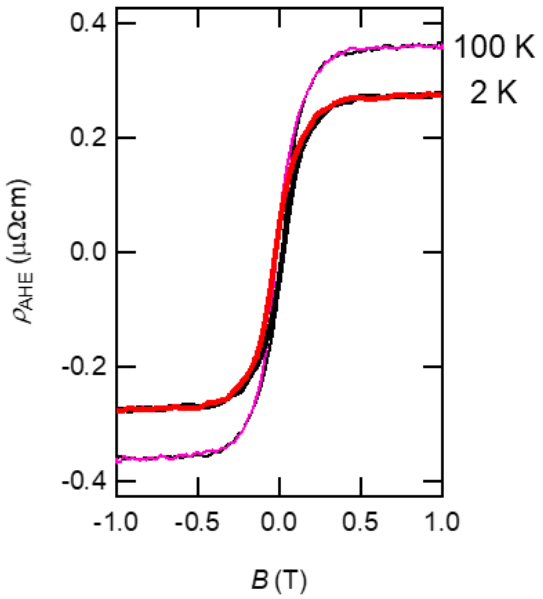

Figure 3.12. Hall resistance for 20-nm-thick Co_2TiGe/MgO (001) as a function of applied field and temperature of 2 and 100K. Low-field Hall resistance is governed by the anomalous Hall effect, while the high-field region is dominated by the ordinary Hall effect.

3.4.4 Anomalous Hall effect analysis

Similar to that of the OHE, we can also extract the anomalous Hall resistance (R_{AHE}) from Figure 3.12 by a zero-field extrapolation of the high field region (OHE). This finds the overall magnitude of the Anomalous Hall effect (AHE), which is then normalized by

the thickness of the film. The AHE can be separated into extrinsic scattering mechanisms (which are due to crystal imperfections and temperature effects), and intrinsic mechanisms which alter the properties of electron wavefunctions due to spin-orbit coupling [65, 97]. The intrinsic AHE is of particular interest for time-reversal symmetry breaking Weyl materials because it arises directly from the Berry curvature, which increases dramatically near Weyl nodes [98, 99]. The anomalous Hall effect scales with resistivity according to

$$\rho_{AH} = R_{AH} \cdot t = a'\rho_{xx0} + a''\rho_{xxT} + b\rho_{xxT}^2 \tag{3.9}$$

where a', a'', and b are fitting constants corresponding to the strength of impurity, phonon, and Berry related contributions, respectively [100]. The result of this analysis is shown in Figure 3.13. It is clear that all three scattering types contribute to the AHE in stoichiometric Co_2TiSn. The parameters $a' = -0.258$, $a'' = 0.00715$ and $b\rho_{xx0} = 0.00335$ are unitless numbers. Based on the fitting parameter, we can conclude that the contribution of the Berry related contribution is small. Thus, we can only conclude the overall AHE is contributed mostly by its extrinsic impurity contribution such as skew scattering and side jump mechanism while only small contribution of Berry curvature.

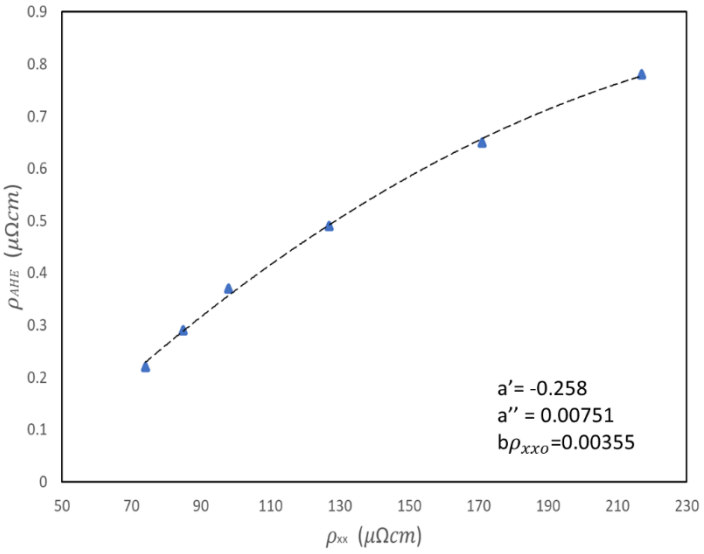

Figure 3.13. AHE analysis showing contributions from impurity (a') and phonon (a") scattering, and Berry curvature ($b\rho_{xx0}$) contributions for a 20-nm-thick Co_2TiGe/MgO (001)

It will be interesting to understand if any other extrinsic contributions such as skew scattering and side jump mechanism [101, 102]. From quantum mechanics, electrons that are scattered will trajectory in a straight line. However, in the presence of spin-orbit interaction, it will result in deviation from the straight line, resulting in asymmetric scattering. This deviation results in skew scattering or side jumping mechanism [102]. It is often suggested that skew-scattering dominates in metals with dilute magnetic impurities and side-jump dominates in ferromagnetic metals and alloys [102]. To do so, it can be analyzed using the scaling law between the anomalous Hall effect and the resistivity by the equation

$$\rho_{AHE} \propto \rho_{xx}^{n} \tag{3.10}$$

For system with n = 1 corresponding to skew scattering and $n = 2$ corresponding to side jump mechanism [65]. Figure 3.14 shows the Anomalous Hall resistivity versus linear resistivity plotted in log10 form for a 20-nm-thick Co_2TiGe/MgO (001). The data fitted well by a linear dependence with $n = 1.191$. This suggests that skew scattering is extrinsic impurity scattering that is dominating in our study.

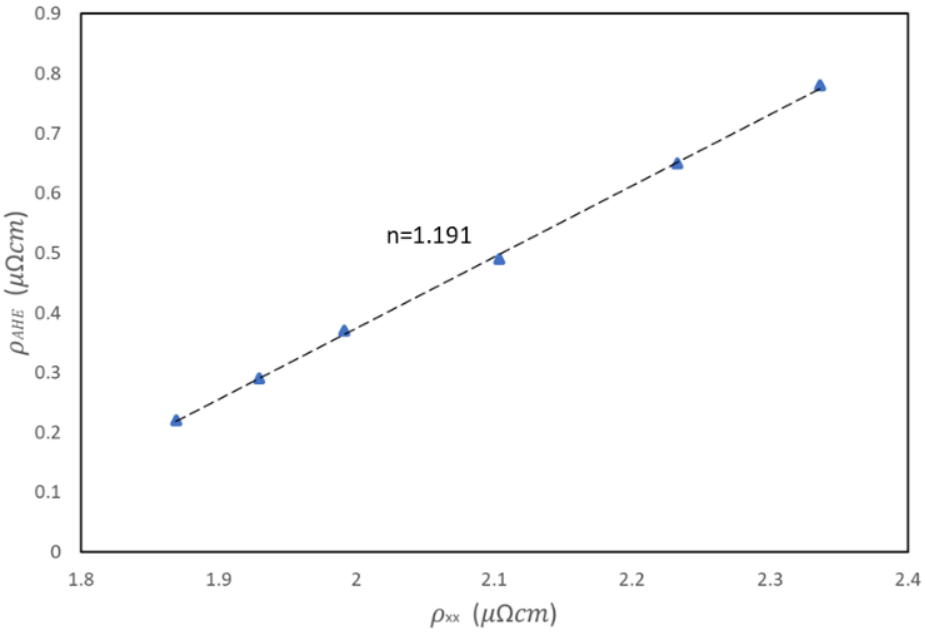

Figure 3.14 Anomalous Hall resistivity versus linear resistivity plotted in log10 form for a 20-nm-thick Co_2TiGe/MgO (001).

Even though there is no clear evidence of the chiral anomaly as a result of the dominated contribution of Berry curvature from the intrinsic AHE, it does not necessarily mean the Co_2TiSn does not possess the Weyl semimetallic properties. In order to study electron near the Weyl point, the Fermi level must be shifted toward the Weyl point [103]. This can be accomplished using electron doping or substituting an element with one

additional electron onto one of the atomic sites. In order to isolate each of the Weyl points in their own Fermi surface it will be necessary to tune the Fermi level upwards by 0.278 eV [42] to be able to draw strong conclusion regarding Co_2TiSn Weyl semi metallicity.

Chapter 4

Fermi level engineering and Angle Resolved Photoemission Spectroscopy of Co_2TiSn using Ni-alloying

4.1 Introduction

In order to shift the Fermi level of the Co_2TiSn toward the Weyl point, Fermi level tuning is required by introducing a substitutional element with one additional/fewer

electron onto one of the atomic sites. For the case of Co_2TiSn, the Weyl point is predicted to be about 278 meV above the Fermi level [42]. Thus, Fermi level can be shift upward by substituting an element with one additional electron. This means alloying Ni onto the Co site, V onto the Ti site, or As onto the Sn site. Unlike some of the other Heusler compounds where alloying can result in tetragonal distortion, alloying Co_2TiSn with Ni element will retain the $L2_1$ crystal structure as Ni_2TiSn is expected to have $L2_1$ crystal structure [104]. The relationship between composition x and the increase in Fermi level is not straightforward and must be experimentally determined or calculated using density functional theory (DFT). Unfortunately, there has not been a DFT calculation of how the Fermi level shifting will be as a function of Ni composition for Co_2TiSn. However, it is likely that the composition x required to move the Fermi level will be small. For example, DFT calculations suggest that $Co_2Zr_{1-x}Nb_xSn$ requires $x = 0.28$ to move the Fermi level upwards by 0.6 eV [105].

Thus, by tuning the Fermi level with Ni alloying to approach the Weyl node, the Berry curvature is expected to increase dramatically, and it may be possible to detect this using AHE. At the same time, the longitudinal magnetoresistance can be measured as a function of Ni-alloying, which would capture the appearance of the chiral conductance, if it exists. This chapter will focus on the growth and transport of the Ni-alloyed Co_2TiSn. A comparison to that of the stochiometric Co_2TiSn film will also be present. ARPES measurement of the stochiometric Co_2TiSn film and the Ni-alloyed Co_2TiSn will be presented to shows the electronic structure of the stochiometric Co_2TiSn as well as the Fermi level tuning of the Ni-alloyed Co_2TiSn.

4.2 Growth of $Co_{2-x}Ni_xTiSn$ using Ni-alloying

From chapter 3, it was determined that Co_2TiSn thin film was a material determined to be low in carrier mobility, no observation of negative longitudinal magnetoresistance, and very mild Berry curvature contribution from its anomalous Hall effect. So far, none of the signatures of the Weyl semimetallic behavior have been observed. However, it does not mean that Co_2TiSn does not possess the Weyl semimetallicity. Instead, it is expected that the Berry phase contribution from the Weyl point to be very small because of the large energy difference between the Weyl point and the Fermi level for the stoichiometric Co_2TiSn. For example, the theoretical analysis calculated by D.T. Son [106] shows that the Chiral anomaly contribution of the anomalous conductivity is given by

$$\sigma_{zz} = \frac{e^2}{4\pi^2\hbar c}\frac{v}{c}\frac{(eB)^2v^2}{\mu^2}\tau \tag{4.1}$$

Where $\hbar$ is the Planck constant, B is the magnetic field, e is the electron charge, τ is the relaxation time, and μ is the energy difference between the Weyl point and the Fermi level position such that

$$\mu = E_{Weyl} - E_F \tag{4.2}$$

This means that conductivity induced by the chiral anomaly drops off quickly as Fermi level shifts away from the Weyl node. This is exactly the case for stoichiometric Co_2TiSn such that the energy difference μ is around 0.278 eV. For this study, Ni substitution for Co was used since it has one additional electron compared to that of the Co and was readily

available in the MBE system that used to synthesize Co_2TiSn. For $Co_{2-x}Ni_xTiSn$, it was identified by our theoretical collaborator, Anderson Janotti, using DFT calculation to indicate that a Ni composition of $x = 0.2$ will be sufficient to shift the Fermi level by about 0.3 eV. Thus, various compositions of Ni alloying from $x = 0$ to $x = 0.2$ was examined. Each of the thin films were grown using the growth condition and post-growth anneal step that were developed in the chapter 3, where 20nm $Co_{2-x}Ni_xTiSn$ thin films were grown at 400 ˚C followed by a post-growth annealing process at 600 ˚C for 20 minutes.

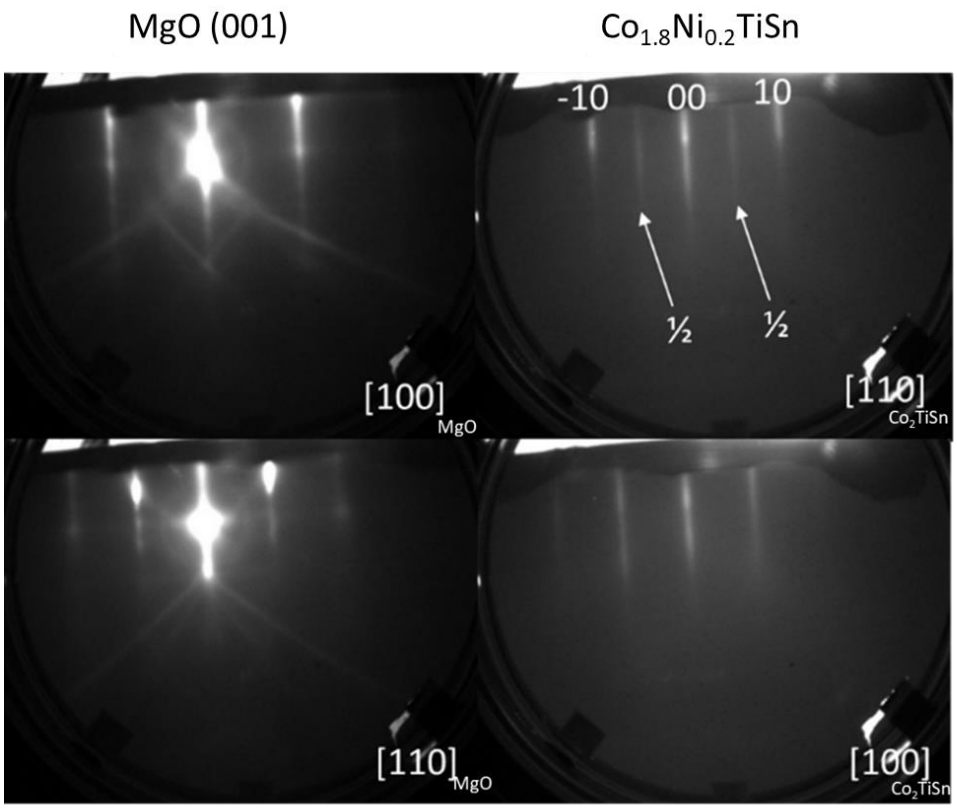

Figure 4.1. RHEED images showing the relevant crystallographic directions of the MgO (001) starting surface and a typical $Co_{1.8}Ni_{0.2}TiSn$ film grown at 400 ˚C and annealed to 600 ˚C for 20 minutes.

Figure 4.1 shows the typical RHEED pattern from the starting MgO (001) substrate at 400 ˚C and the $Co_{2-x}Ni_xTiSn$ thin film at x = 0.2 after the post-growth annealing step. Similar to Co_2TiSn thin film, the grown MgO buffer layer shows the expected (1x1) bulk unreconstructed surface reconstruction and the c(2x2) Full Heusler RHEED construction was observed at all Ni alloying composition up to $x = 0.2$. The ½ order specular streak can be seen along the [110] and $[1\bar{1}0]$ direction of $Co_{2-x}Ni_xTiSn$ thin film as shown in figure 3.1.

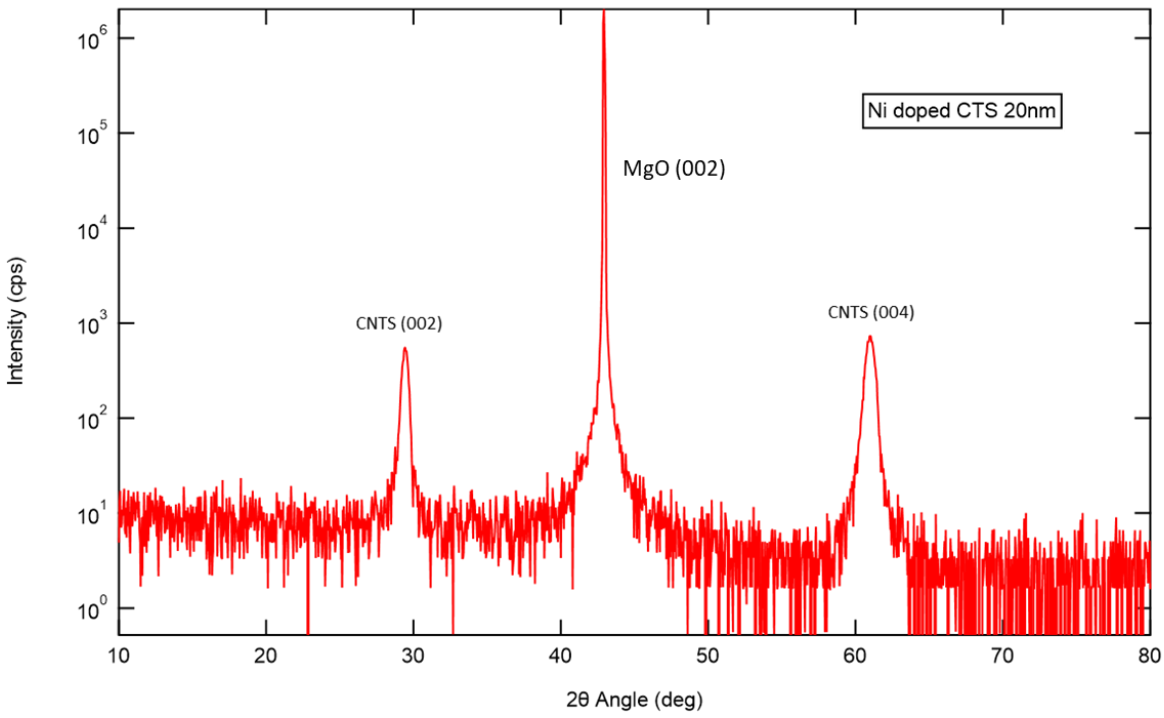

Figure 4.2. XRD of 20 nm $Co_{1.8}Ni_{0.2}TiSn$/MgO (001) thin film

Figure 4.2 shows the X-ray diffraction of a 20 nm $Co_{1.8}Ni_{0.2}TiSn$/MgO (001) thin film. The X-ray diffraction shows the expected (002) and (004) peak for the $Co_{1.8}Ni_{0.2}TiSn$ without any additional phases. This result is consistent with all Ni alloying composition from $x = 0$ all the way to $x = 0.2$. One thing to note is that the peak intensity ratio between the (002) and the (004) peak is higher for the $Co_{2-x}Ni_xTiSn$ than that of the Co_2TiSn thin film. The peak ratio is approximately 0.63 compared to the expected 0.43 for $L2_1$ ordering Co_2TiSn thin film. In addition, the FWHM of the (002) and (004) peaks are very sharp, meaning high crystallinity of the $Co_{2-x}Ni_xTiSn$ thin film was grown. What can be concluded from the XRD is that the $Co_{2-x}Ni_xTiSn$ thin film are at least some B2/$L2_1$ ordering based on the larger peak ratio between the (002) and (004) peak.

The XRD-RSM presents similar results to that of Figure 3.9 where a high intensity peak of (111) Bragg peak can be observed for all Ni alloyed composition. The normalized line scan of (111) Bragg peak is show in figure 4.3, which was observed for all Ni- alloying concentration. This suggests that the $Co_{2-x}Ni_xTiSn$ thin films using the growth method from chapter 3 have resulted in a $L2_1$ order thin films. The data from the XRD and XRD-RSM show promising results of high $L2_1$ order $Co_{2-x}Ni_xTiSn$ thin films. However, one still needs to determine the surface morphology of the thin film in order to provide a smooth surface to obtain high resolution ARPES data.

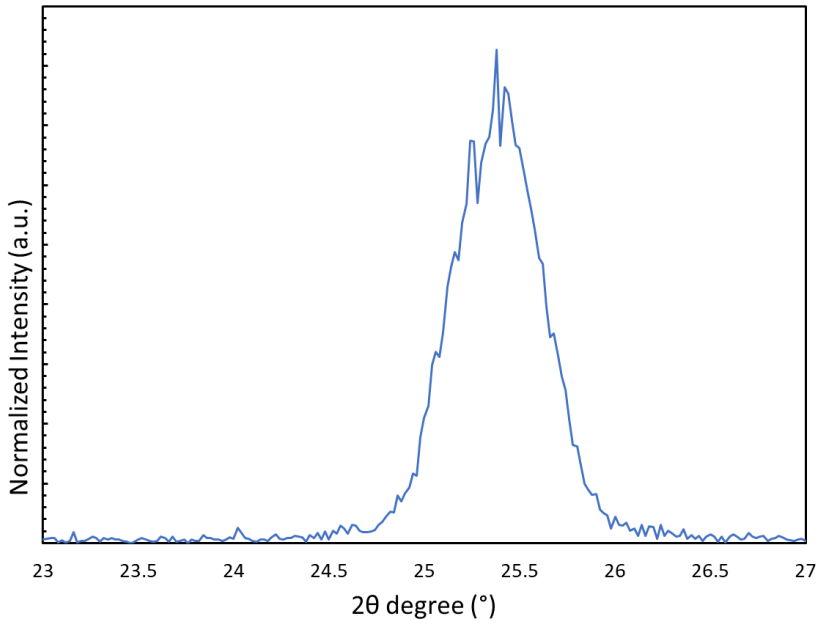

Figure 4.3. Normalized line scan of the $Co_{1.8}Ni_{0.2}TiSn$ (111) Bragg peak for post-growth at 650 ˚C annealing temperature for 20 nm $Co_{1.8}Ni_{0.2}TiSn$ thin film on MgO (001).

Figure 4.4 shows the STM image and a line scan of $Co_{1.8}Ni_{0.2}TiSn$/MgO thin film with a 225 nm by 225 nm scan. From the STM analysis, the surface morphology is uniform throughout the whole thin film. From the line scan indicated from the red line in the STM image, the surface roughness varies around 1 to 2 nm on average and is uniform throughout the thin film. Overall, the grown thin film is relatively smooth and no observation of any surface dislocation or impurity phases can be observed.

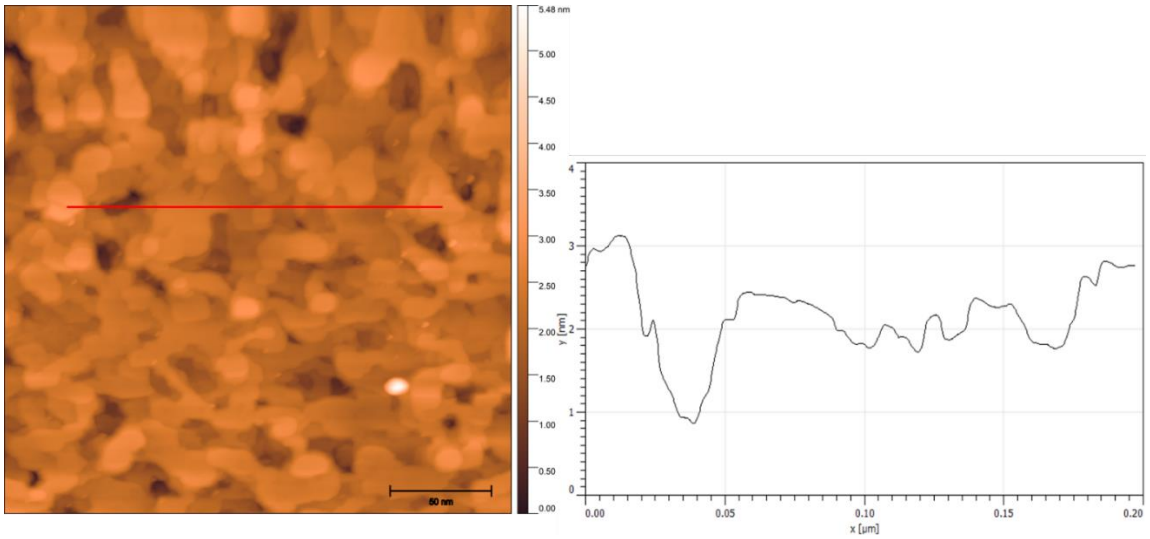

Figure 4.4. (Left) STM image and (right) a line scan corresponding to the red line on the STM image of a 20 nm $Co_{1.8}Ni_{0.2}TiSn$/MgO (001) thin film

4.3 Transport Comparison of Stochiometric Co_2TiSn and $Co_{2-x}Ni_xTiSn$

With the $L2_1$ order $Co_{2-x}Ni_xTiSn$ thin film, it will be our interest to see if a Ni concentration of $x = 0.2$ is enough to raise the Fermi level to the Weyl point through transport measurement. Starting with the temperature dependent resistivity in Figure 4.5, it can be seen that both the Co_2TiSn and $Co_{2-x}Ni_xTiSn$ show very similar curvature throughout the measured temperature region. Similar to before, the resistivity is metallic like. By fitting the data with the Chien model [94], the fitting shows a moderately good fit between the temperature of 75 K all the way to around 290 K. Unfortunately, the measurement was only taken up to 300K while the maximum from the resistivity is beyond

that of the 300K. As a result, we can only conclude that the Curie temperature of the $Co_{2-x}Ni_xTiSn$ thin film is above 300K, similar to that of the Co_2TiSn.

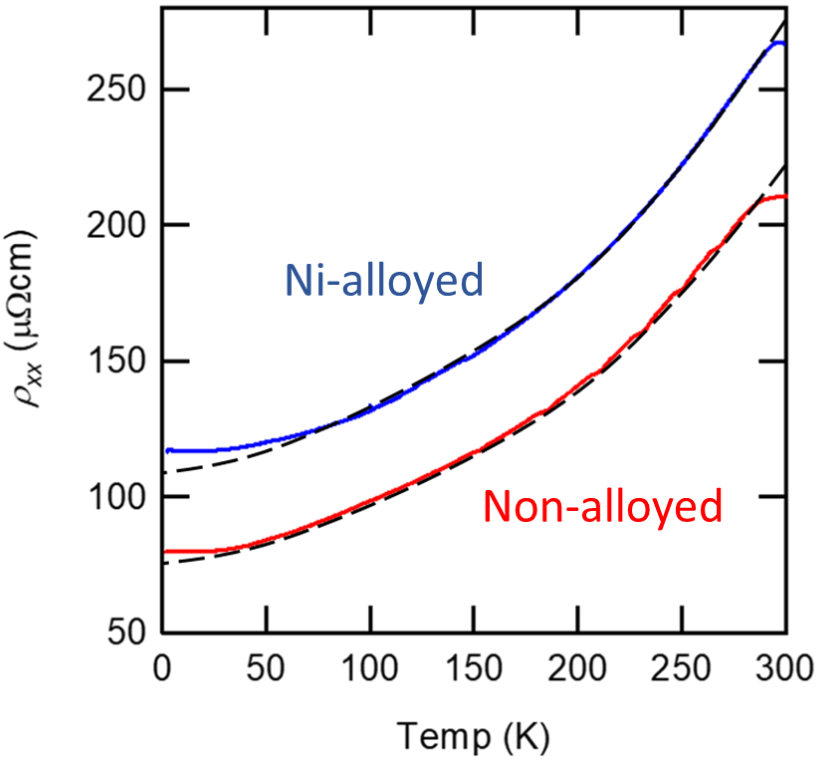

Figure 4.5. Resistivity vs. temperature for (red) 20-nm-thick Co_2TiSn/MgO (001) film and (blue) 20-nm-thick $Co_{1.8}Ni_{0.2}TiSn$ /MgO (001) film.

Interestingly, the resistivity increases uniformly throughout the full temperature region between the Co_2TiSn and the $Co_{2-x}Ni_xTiSn$ thin film by 1.5 times for Ni concentration of $x = 0.2$. A few things that can attribute to this result: 1) the increase in resistivity is due to the contribution from the Weyl point as the Fermi level shifted closer to it, 2) it increases simply by the virtue of the Ni element having one additional electron that contributes to the increase in the resistivity, or 3) the increase in resistivity is due to

the alloy scattering [107]. As it was previously discussed, even if the Fermi level was tuned to the Fermi level, the observation of the Weyl semimetallic behavior can still be obscured by the high number of bulk bands [7].

A large difference in AHE between the stoichiometric Co_2TiSn and $Co_{2-x}Ni_xTiSn$ is anticipated as the Berry phase contribution is expected to increase dramatically as the Fermi level approaches the Weyl point. Figure 4.6 shows the resistivity ρ_{xx} and Hall resistance (left) and the anomalous Hall resistance (right) as a function of applied magnetic field for both the Co_2TiSn and $Co_{2-x}Ni_xTiSn$ thin film. The resistivity ρ_{xx} shows similar behavior under the applied field between Co_2TiSn and $Co_{2-x}Ni_xTiSn$ where the maximum value of resistivity is reach when there is no applied field and decreases with increasing applied field. The resistivity is increased by around 1.5 times. The same behavior can also be seen in the anomalous Hall resistance measurement on the right where the curvature of the data is approximately identical, but the AHE value in high field region and the AHE value at 1T are increased by ~1.5 times with the Ni alloying. From the ordinary Hall effect, the slope is positive. Thus, the dominant carriers $Co_{2-x}Ni_xTiSn$ are holes. The hole density is about 2.0×10^{22} $/\mathrm{cm}^3$ 100K and 1.7×10^{22} $/\mathrm{cm}^3$ at 2K while the hole carrier mobility is around 2.5 $\frac{\mathrm{cm}^2}{\mathrm{Vs}}$ at 2K. The transport behavior is still metallic like similar to that of the Co_2TiSn thin film with very little change in mobility and carrier concentration.

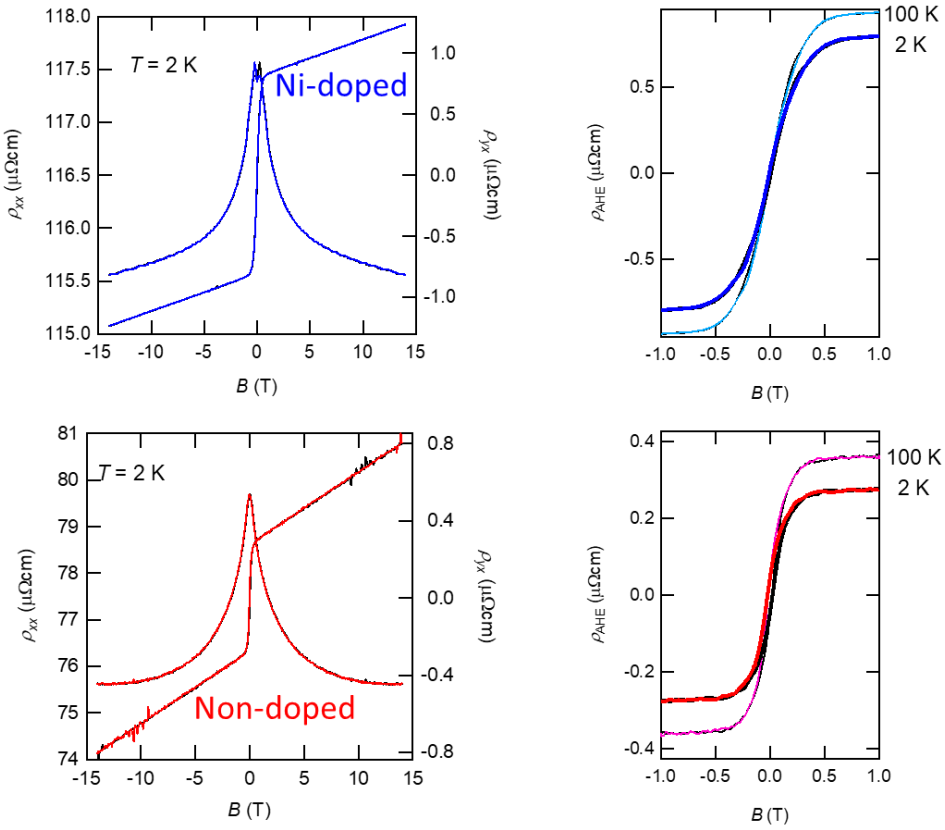

Figure 4.6. (left) Resistivity vs. applied magnetic field for (red) 20-nm-thick Co_2TiSn/MgO (001) film and (blue) 20-nm-thick $CO_{1.8}Ni_{0.2}TiSn$ /MgO (001) film at 2 K and (right) the anomalous Hall resistance as a function of applied field and temperature for 2 and 100 K.

Unfortunately, it does not seem like there are any obvious signature of Berry curvature contribution from the Weyl point as the increases in the AHE as well as the resistivity is not significant. However, it does not mean the Fermi level tuning does not work. It suggests that $x = 0.2$ of Ni alloying was not enough to shift the Fermi level to the Weyl point. One of the recent theoretical calculation works by Payal Chaudhary shows that it requires about 50% V alloyed compound in comparison to the stoichiometric Co_2TiSn in order to bring the Fermi nodes and the Fermi arcs near the Fermi level [42]. Thus, the 20%

Ni alloying might not have been enough to shift the Fermi level close enough such that the contribution of Berry curvature from the Fermi nodes and the Fermi arcs could be observed. As a result, careful analysis using ARPES will be required to understand the electronic structure of Co_2TiSn and $Co_{2-x}Ni_xTiSn$ as well as the degree of Fermi level tuning that can be achieved by using Ni alloying.

4.4 ARPES analysis of Co_2TiSn and Ni-alloyed Co_2TiSn

Angle resolved photoemission spectroscopy (ARPES), as discussed in chapter 2, is an experimental technique that utilizes the photoelectric effect to understand the nature of electronic structures of solids. It has become a widely used method when it comes to understanding topological materials due to their complex nature that sometimes cannot be fully understood or observed through magneto transport or electrical transport. To identify materials that possess the Weyl properties that arise from the Weyl nodes and Fermi arc which are far away from the Fermi level, it can be extremely difficult to observe those properties through traditional transport analysis as they often get overshadow by the conduction in the bulk of the material. Thus, the goal here is to study the electronic structure of the Co_2TiSn and $Co_{2-x}Ni_xTiSn$ using ARPES to determine if the Fermi level tuning using the Ni works.

The confirmation of Fermi level tuning allows the application of the Ni- alloying for the Co_2TiSn. To our knowledge, there have not been any reported ARPES studies for the Co_2TiSn thin film or bulk crystals. Thus, the first step will be to measure the electronic structure of the Co_2TiSn using ARPES. The same growth process and post-growth annealing step were utilized for the thin film samples for the ARPES measurement. However, two major challenges arise: 1) the transferring of the thin film samples from the Palmstrøm Lab to the beamline at either the Advanced Light Source at Lawrence Berkeley National Lab or SLAC National Accelerator Laboratory at Stanford University without exposing them to the atmosphere and 2) MgO is an insulator and normally would be unusable as a substrate for photoemission measurement due to charging effect. Unfortunately, typical methods of capping samples with materials such as Sb or As and decapping at the beamline was found previously by former colleagues that the capping material would either reacted with the surface of the samples. As a result, a vacuum suitcase was developed. The vacuum suitcase is a small UHV transfer arm with a sample storage cassette attached to its end. A getter ion pump and c double gate valves were used to retain a UHV pressure in the 10^{-11} torr range during transportation to the beamlines. It worked extremely well as the suitcase can be attached and detached between vacuum chamber without exposing the samples to the atmosphere. In addition, the getter ion pump can be run by UPS battery backup to keep the pump running during transportation. This has brought new insights into bringing pristine thin film samples to beamline. For the MgO substrate, it was previously determined that by having excess In bonding between the MgO substrate and the Omicron sample plate, the In bonding will prevent charging at the surface.

However, it was later verified at the beamline under Ultraviolet photoelectron spectroscopy that In from the bonding tend to rise to the surface of the thin film. This can potentially modify the surface morphology and composition as well as destroyed the Weyl semimetallic properties. As a result, a custom sample plate was used to attach the MgO substrate using large clips. The large clips can be moved within the ARPES measuring chamber using a wobblestick to electrically short the grown thin film surface to the sample plate, allowing charge-free measurements in ARPES.

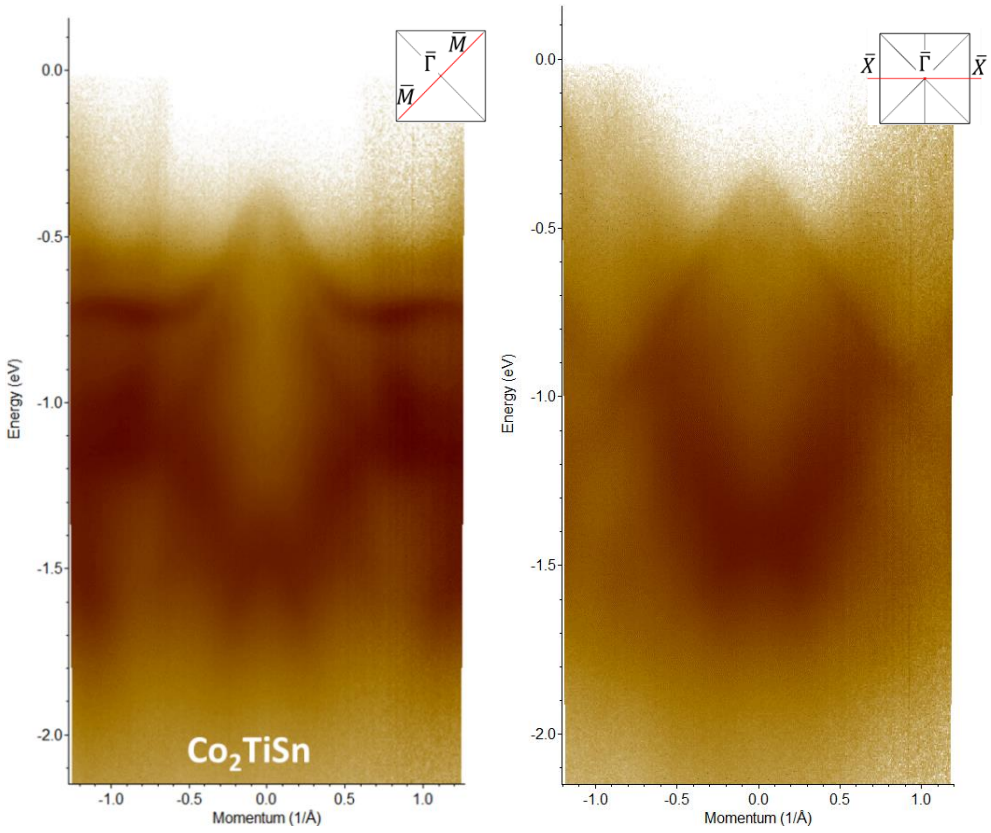

Figure 4.7. APRES energy dispersion slices collected at hv = 62 eV for Co_2TiSn along the (left pair) $\bar{M} - \bar{\Gamma} - \bar{M}$ and (right pair) $\bar{X} - \bar{\Gamma} - \bar{X}$ directions.

Figure 4.7 shows the measured ARPES energy dispersion slices collected at $h\nu = 62$ eV for Co_2TiSn along the (left pair) $\bar{M} - \bar{\Gamma} - \bar{M}$ and (right pair) $\bar{X} - \bar{\Gamma} - \bar{X}$ directions. The resulting ARPES dispersion slice is very desirable as the resolution of the bands and features are comparable to even some of the well-established Weyl semimetal binary compounds such as TaAs [77]. This is one of the few high resolutions of ARPES data among all of the literature related to the study of Heusler compound and the first for the Co_2TiSn thin film. The next step is to compare the ARPES data to the theoretical calculations to see if the features are genuine.

Figure 4.8 shows the APRES energy dispersion slice and the second derivate analysis collected at $h\nu = 62$ eV for Co_2TiSn along the $\bar{M} - \bar{\Gamma} - \bar{M}$ direction with various dotted color lines as guide. In order to compare to the theoretical calculations, Figure 1.7 from chapter 1 will be used for comparison. By examining the band structure from Figure 1.7 along the $X - \Gamma$ direction and mirrored along the Γ point, the band structure along the $X - \Gamma - X$ momentum direction from Figure 1.7 is equivalent to that of the APRES slice of $\bar{M} - \bar{\Gamma} - \bar{M}$ direction in Figure 4.8. Several features from the ARPES data reflected well with the theoretical calculations. For example, the two parabolic like bands highlighted by the red and orange dotted line at the $\bar{\Gamma}$ point matches with the bands at the Γ point in Figure 1.7. These two bands are the minority spin band that is below the Fermi level. In addition, another parabolic like band highlighted by the white dotted line emerge from the Γ point with the minimum energy position of -1.5 eV can also be seen in the theoretical calculated band structure, which is a majority spin band of Co_2TiSn.

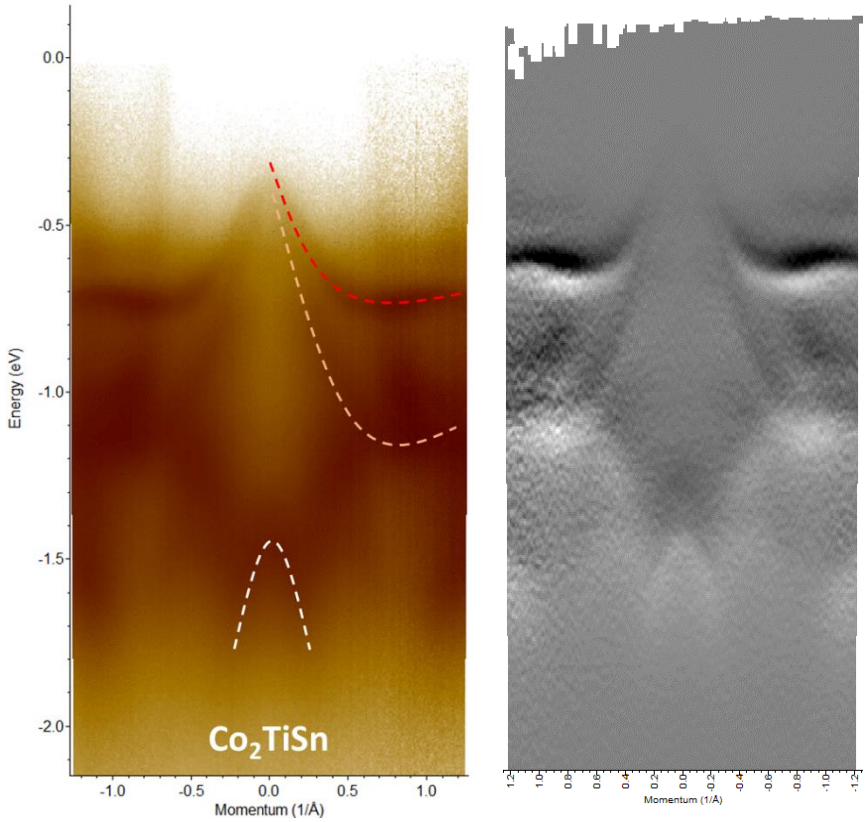

Figure 4.8. (Left) APRES energy dispersion slice collected at hv = 62 eV for Co_2TiSn along the $\overline{M} - \overline{\Gamma} - \overline{M}$ and (right) the second derivative analysis. The red dotted lines are only serving as a guide to the features presented in the second derivative.

Similarly, the feature from the $\overline{X} - \overline{\Gamma} - \overline{X}$ direction of ARPES dispersion slice shown in Figure 4.9 also matches relatively well by overlaying the experimental and theoretical predicted band structure in Figure 1.7. For example, a band with a relatively linearly dispersion, which corresponding to the spin minority band, highlighted by the red dotted line can be observed along the $\overline{\Gamma} - \overline{X}$ direction in the valance band. However, the 2-band

crossing at the Fermi level corresponding to the spin majority band in the $\overline{\Gamma} - \overline{X}$ direction from the theoretical calculation was not observed.

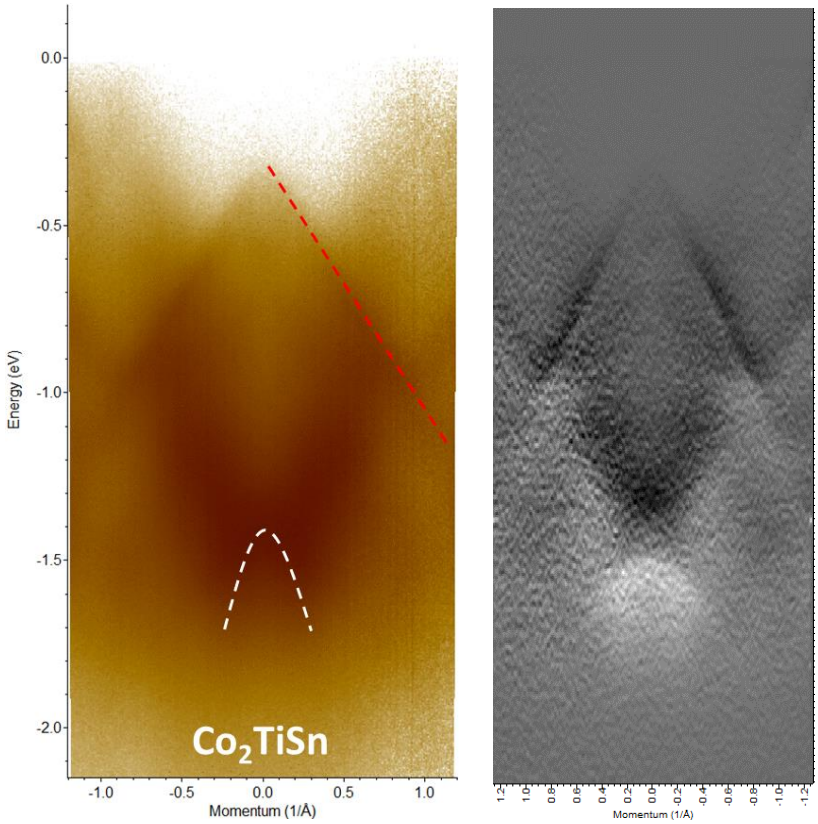

Figure 4.9. (Left) APRES energy dispersion slice collected at $h\nu = 62$ eV for Co_2TiSn along the $\overline{X} - \overline{\Gamma} - \overline{X}$ and (right) the second derivative analysis. The red dotted lines are only serving as a guide to the features presented in the second derivative.

Besides the relatively linear band highlighted by the red dotted line, the parabolic band that is highlighted by the white dotted line with the minimum energy position of around -1.4 eV can also be observed. This band, which corresponding to the spin majority band, matching well with the theoretical calculation in Figure 1.7. Unfortunately, the additional band features below the linearly dispersed band are very difficult to interpret because of

the blurriness of the spectral intensity. Regardless, we can still confidently conclude that these APRES dispersion slices are precisely the electronic structure of the Co_2TiSn.

Lastly, several ARPES dispersion slices along the $\bar{M} - \bar{\Gamma} - \bar{M}$ direction were examined with various θ angles that sweep through the Fermi surface. The goal was to see if any interesting features can be observed as the measurement sweep through the W_{001}^1 Weyl point shown in the Fermi map on the top right of Figure 4.10. Interestingly, a parabolic-like band emerged as we moved toward the W_{001}^1 Weyl point.

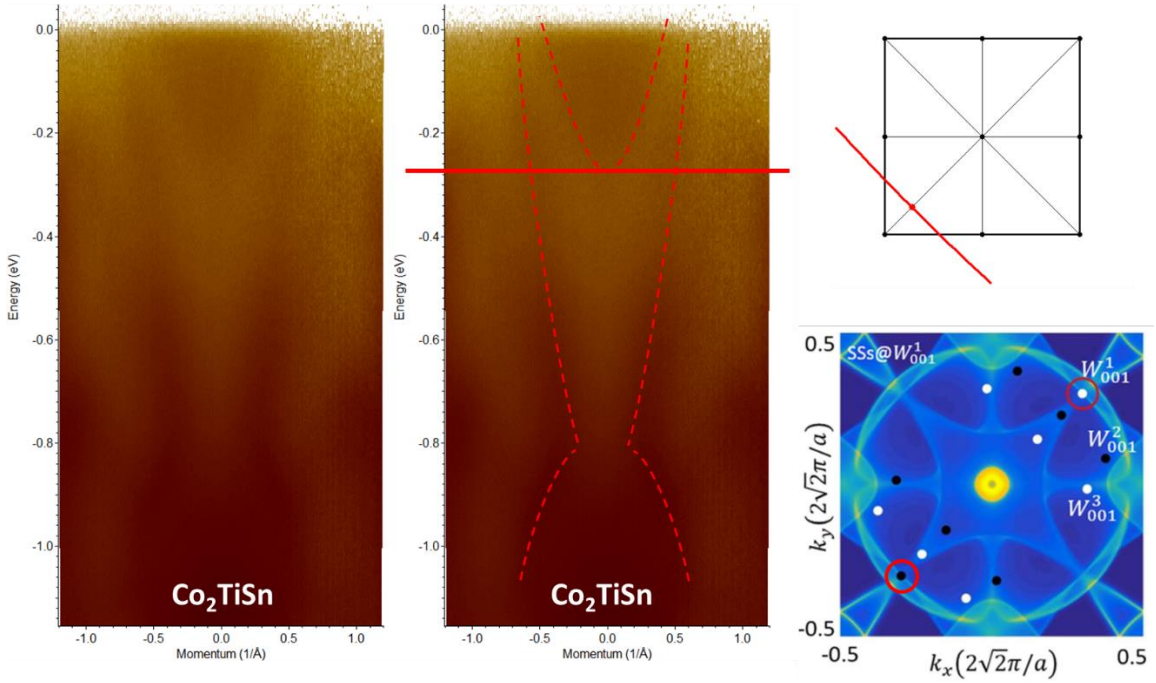

Figure 4.10. (Left) APRES energy dispersion slice collected at hv = 62 eV for Co_2TiSn along the across the W_{001}^1 Weyl point. The red dotted lines are only serving as a guide to the features presented in the second derivative. Fermi map on the bottom right is reprinted from [7] under a Creative Commons Attribution 4.0 International License.

The feature is very subtle as slight change in the θ angles. Of course, this ARPES dispersion slice shown in Figure 4.10 has to be interpreted with care since there is no clear comparison from the theoretical calculation as the dispersion slice is not from a major symmetric direction. However, it is still interesting to see that the band that emerges as we move closer to the W_{001}^{1} Weyl point has a minimum energy position of about 0.28 eV, which matches very closely with the expected W_{001}^{1} Weyl point from theory, which is expected to be 0.278 eV below the Fermi level. Though, this can only be considered as a speculation rather than a definite proof of the Weyl point.

4.5 Fermi level Tuning Analysis of Ni-alloyed Co_2TiSn

With the relative high resolution of spectral density from the ARPES measurement, it is possible to determine the quantity of Fermi level tuning from the Ni substitution with greater certainty. Figure 4.11 shows the ARPES dispersion slices of several different Ni composition of x = 0, 0.1, 0.13, and 0.16 of $Co_{2-x}Ni_xTiSn$ thin film along the $\bar{X} - \bar{\Gamma} - \bar{X}$ direction. The ARPES slices are align with respective to the Fermi level at $E = 0$, which is highlighted by the white dotted line. The red dotted line that shows the fitting to the band with a relatively linearly dispersion along the $\bar{\Gamma}$ point and the orange dotted line that show the energy position to the maximum of the band at $\bar{\Gamma}$ point. As we can see from the ARPES

slices, a downward shifting of the orange line can be observed as we increase the Ni composition.

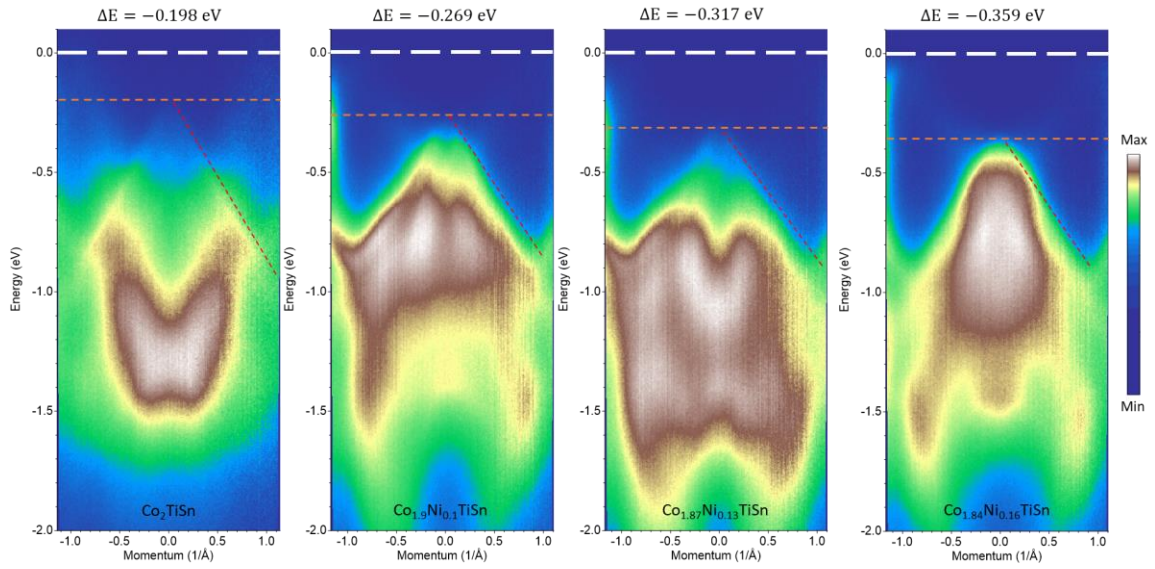

Figure 4.11. Energy-momentum spectral map taken at 16 K along the $\overline{X} - \overline{\Gamma} - \overline{X}$ direction close to the bulk Γ point of $Co_{2-x}Ni_xTiSn$ at several different Ni composition of $x = 0$, 0.1, 0.13, and 0.16 of $Co_{2-x}Ni_xTiSn$ thin film. The white dotted line is the Fermi level at 0 eV. A band with a relatively linearly dispersion can be observed along the $\overline{\Gamma} - \overline{X}$ direction, which is highlighted by the red dotted line that show the fitting to the band with a relatively linearly dispersion along the $\overline{\Gamma}$ point and the orange dotted line that show the energy position to the maximum of the band at $\overline{\Gamma}$ point compared to figure 1.7 along the $\overline{\Gamma} - \overline{X}$ direction.

From the shifting of the orange dotted line, we were able to successfully demonstrate an upward shift in Fermi level by 161 meV. However, this is not enough to shift the Fermi level toward the Weyl point as the energy difference between the Weyl point and Fermi level was expected to be 0.278 eV. Thus, in order for us to realize the Weyl semimetallicity of Co_2TiSn, we will need to increase the Ni alloying above 20% in order to shift the Fermi

level toward the Weyl point and determine if any Fermi arc and Weyl points can be observed using ARPES. However, this study demonstrates that we have successfully shifted the Fermi level by 0.161 eV.

Chapter 5

Growth, characterization, and Fermi level tuning of half Heusler PtMnSb and $Pt(Mn_{1-x}Lu_x)Sb$

5.1 Introduction

In 1995, the very first "half metal" materials, which are NiMnSb and PtMnSb, were predicted by S. J. Youn [108]. These new materials are very exciting because by

considering spin orbit coupling, they have majority spin bands that are metallic while the minority spin bands are semiconducting [108]. Although there have been several studies of NiMnSb [109-111], there has been very little experimental works done on the PtMnSb [49-50, 112]. On the other hand, PtLuSb, a half Heusler compound that is similar to the PtMnSb, was experimentally observed to be a Heusler compound that possess a topologically non-trivial surface state [5]. This is exciting because the arise of the topological surface state in the PtLuSb is the band inversion of the Γ_8 and Γ_6 band along the Γ momentum direction at the zero-band crossing point shown in the right figure of figure 5.1.

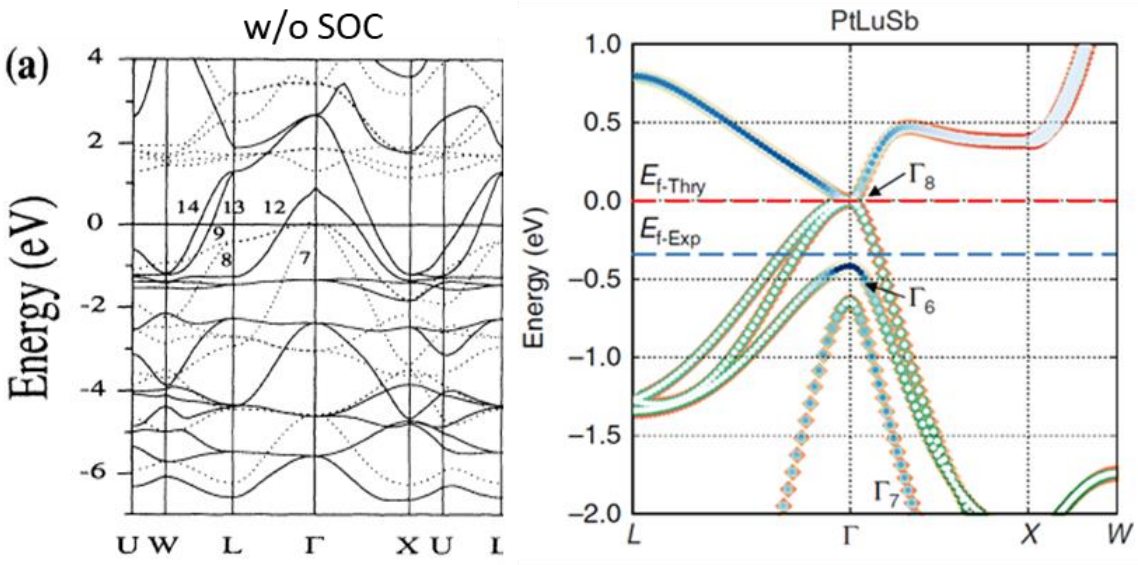

Figure 5.1. (left) First principles calculated bulk electronic band structure of PtMnSb. (right) First principles calculated bulk electronic band structure of PtLuSb. Image reprinted from [108] with permission and [5] under a Creative Commons Attribution 4.0 International License

PtMnSb shows very similar band structure as to that of the PtLuSb, which is shown on the left of figure 5.1. But what could happen if we introduced Lu element onto the Mn site of PtMnSb to Fermi level tune the Fermi level as well as the band gap of PtMnSb? This is essentially the question we would like to answer in this last part of the study of this dissertation to understand how Fermi level tuning using Lu substitution affect the band structure of the PtMnSb. what we are interested in is to determine if there will be any possible Weyl phase results from the band crossing along the Γ direction within the band gap because of the band closing by Mn-Lu alloying. Thus, in this study, we need to establish a method to stabilize the growth of PtMnSb and Pt($Mn_{1-x}Lu_x$)Sb thin film using Molecular Beam Epitaxy, examine its transport properties to see if any Weyl transport can be observed with Lu alloying, and study the Fermi level shifting and change in band structure using ARPES to understand the Lu alloying effect and determine if any Weyl phases can be observed.

5.2 Growth of PtMnSb and Lu alloyed Pt($Mn_{1-x}Lu_x$)Sb

In terms of thin film growth, growth of PtMnSb has been previously done by growth of co-sputtering of PtMnSb (001) thin film on Cr (001)/MgO (001) and MgO (001) [49] and PtMnSb (111) thin film on Al_2O_3 (0001) [50] by other studies in the past. However, growth of PtMnSb on the oxide substrate has resulting in low crystallinity thin film because of the relatively large lattice mismatch (+4% and 7% on MgO (001) and Cr/MgO (001) respectively) and high degree of mosaicisity and crystal twinning from the oxide substrates.

This study, we utilize molecular beam epitaxy to growth single-crystal PtMnSb (001) and $Pt(Mn_xLu_{1-x})Sb$ thin films on an MBE-grown LuSb barrier layer on a GaSb (001) substrate. LuSb was chosen as the substrate because of several reasons. LuSb has a relatively small lattice mismatch (2.6% lattice mismatch with PtMnSb) and similar crystal structure to that of the PtMnSb. LuSb substrate also has a much higher crystalline quality compared to the oxide substrate that has been shown in the other studies [49, 50]. In addition, LuSb has been found to be a great diffusion barrier that prevent interfacial reaction between the PtMnSb and GaSb. Thus, all these reasons make LuSb an excellent template for heteroepitaxial growth. The substrate structure consisted of MBE-grown LuSb(6nm)/ Be doped GaSb (500 nm) on a Zn doped GaSb (001) substrate. The thin film growth was accomplished by codepositing high purity elemental Mn, Sb, and Lu from effusion cells and Pt from an electron beam evaporator in an ultra-high vacuum MBE growth chamber. The Pt flux was controlled by controlling the e-beam filament emission current for a set flux measured using an *in-situ* Quartz crystal microbalance that had been calibrated by measuring the atomic areal densities by RBS of films grown on Si substrates. Similarly, the Mn, Sb, and Lu effusion cells atomic fluxes versus effusion cell temperature were calibrated by measuring film atomic areal densities grown on Si substrates with RBS. Figure 5.2 shows the typical growth procedure for the PtMnSb thin film on a LuSb buffer layer. The LuSb barrier layer was grown on a 500 nm Be doped GaSb (001) buffer layer using the growth method developed by Shouvik Chatterjee et al., which the detail of the LuSb growth method can be found in [113].

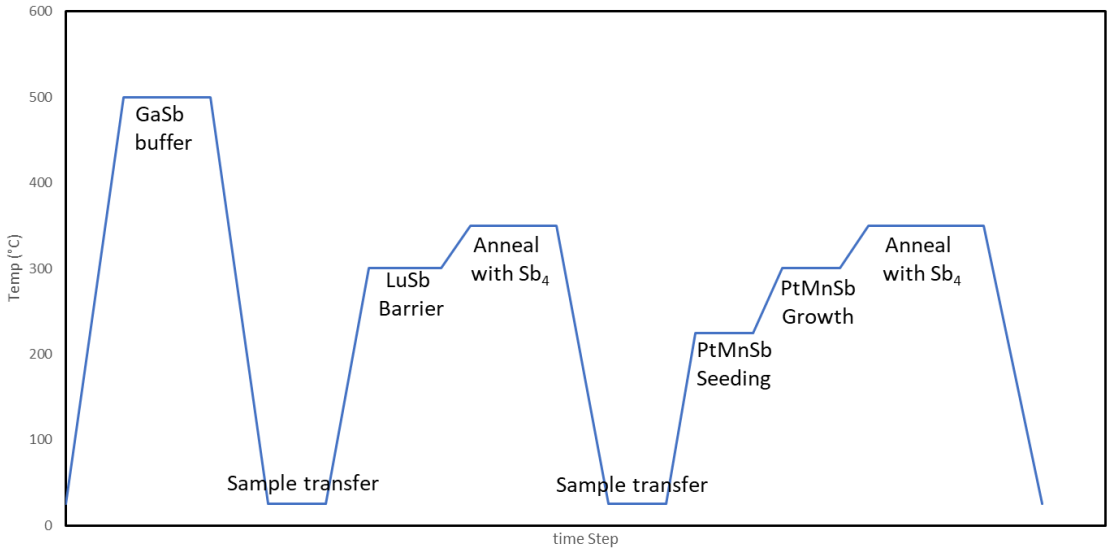

Figure 5.2. typical growth steps of PtMnSb thin film on LuSb barrier. GaSb buffer were first grown in the VG V80H III-V MBE system (as shown in figure 2.1) and transfer to the MOD Gen-II EMOF MBE for Heusler alloys for the LuSb barrier layer. The second sample transfer step is only necessary if the grown LuSb barrier was planned for a later experiment, where the LuSb barrier will be transferred and stored in the Gen-II preparation chamber.

Figure 5.3 shows the crystal structure and epitaxial relationship for PtMnSb (001) // LuSb (001) // GaSb (001) as well as the growth structure of the PtMnSb thin film on LuSb buffers layers. The 6 nm thick LuSb buffer were first preheated to 225 °C to prepare for a low temperature seeding layer growth. The purpose of this lower temperature seeding growth is to facilitate the nucleation of the PtMnSb on top of the LuSb buffer layer. This is accomplished by using a shutter growth where the initial growth is switching between 1 monolayer of Pt and 1 monolayer of Mn/Sb by close and opening the shutter of each effusion cell (Pt layer → Mn/Sb layer → Pt layer → Mn/Sb layer → repeat). A total of 8 monolayers of Pt and 8 monolayers of Mn/Sb were deposited for the seeding growth. After

the seeding growth, the growth temperature is increased to 300 °C for co-deposition for the rest of the PtMnSb layer. PtMnSb sample with thickness of 5 nm, 13nm, and 33 nm were grown in this study. After PtMnSb thin films were deposited, the manipulator temperature is increase to 350 °C for a 10-minute post-growth annealing step under Sb_4 overpressure to prevent re-evaporation of Sb from the PtMnSb thin film.

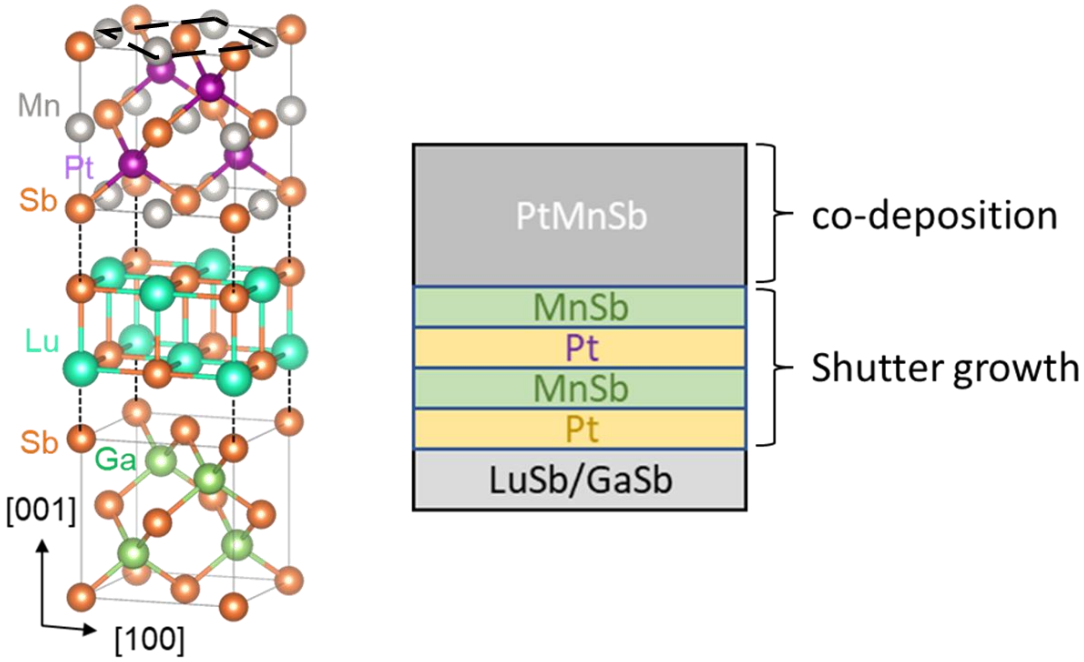

Figure 5.3. (left) crystal structure and epitaxial relationship for PtMnSb (001) // LuSb (001) // GaSb (001). (right) the growth structure of the PtMnSb thin film on LuSb buffer. The surface unit cell indicated by the dotted line with axes along the bulk <100> and <010> axes is shown

Figure 5.4 shows the typical RHEED patterns of the LuSb buffer and the grown PtMnSb thin film. The expected (1×1) surface reconstruction can be seen from the stoichiometric rock-salt LuSb atomic layers as shown in the [110] and $[1\bar{1}0]$ direction. On

the other hand, PtMnSb shows the 2 by reconstruction in the [110] direction, showing a c(2×2) pattern similar to those of PtLuSb [5]. The resulting RHEED patterns shows streaky RHEED pattern, indicating smooth surface. The use of 10-minute post-growth annealing step under Sb_4 overpressure slightly improve the streakiness of the specular spot with no change in RHEED reconstruction. However, the post-growth annealing step improves the surface roughness as observed by in-situ STM measurements.

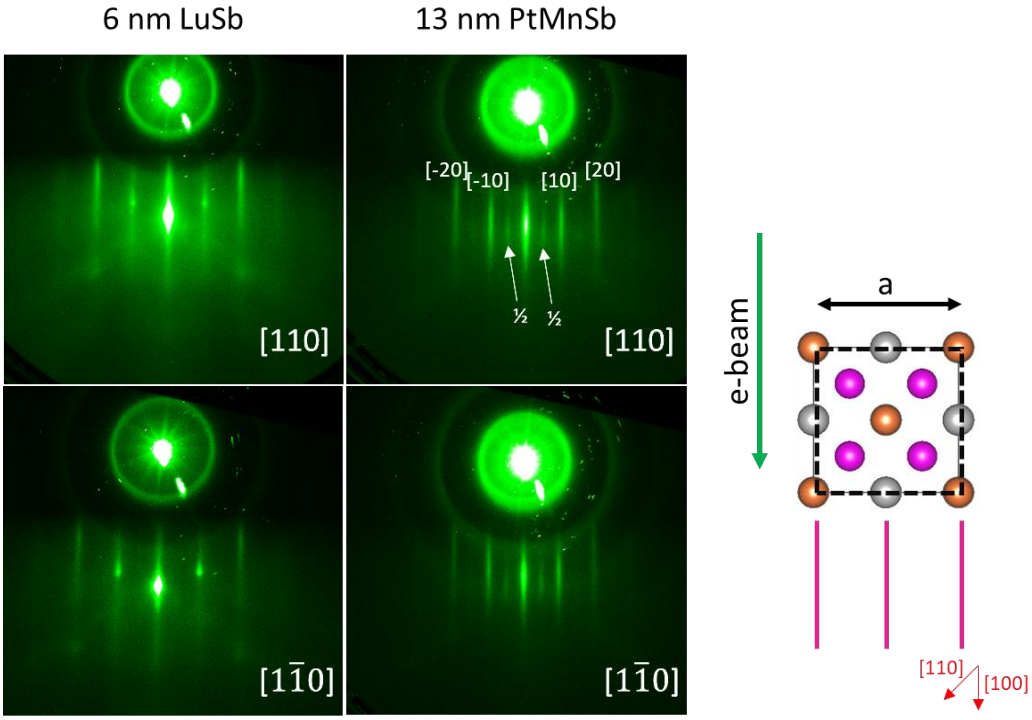

Figure 5.4. RHEED pattern of the 6 nm LuSb buffer layer and 13 nm PtMnSb thin film in the [110] and [1$\bar{1}$0] direction along the GaSb (001) substrate (right) shows the relationship between the RHEED beam along the [110] direction of PtMnSb from a top-down view.

Left of figure 5.5 shows the *in-situ* STM images of PtMnSb thin film before and after the post-growth annealing process. As we can see from the *in-situ* STM images, the

PtMnSb thin film without any post-growth annealing process form large terraces with large steps between each terrace. The root mean square of the surface roughness is calculated to be around 1.1 nm. On the other hand, PtMnSb thin film after 10-minute post-growth annealing step under Sb_4 overpressure has much smoother surface with a root mean square of the surface roughness of 0.3 nm. Thus, the usage of the post-growth annealing step help improves the smoothness of the PtMnSb thin film. In addition, right figure of 5.5 shows the transmission electron microscopy (TEM) measurement of the PtMnSb thin film after the post-growth annealing step. The HAADF-STEM image shows very abrupt and smooth interface between the PtMnSb/LuSb and LuSb/GaSb layer as indicated by the black dotted line. In addition, the structure of each layer along the [001] direction matches well with the crystal model shown in the inset on the right, indicating great chemical ordering of the PtMnSb sample that has been grown using the grown condition above.

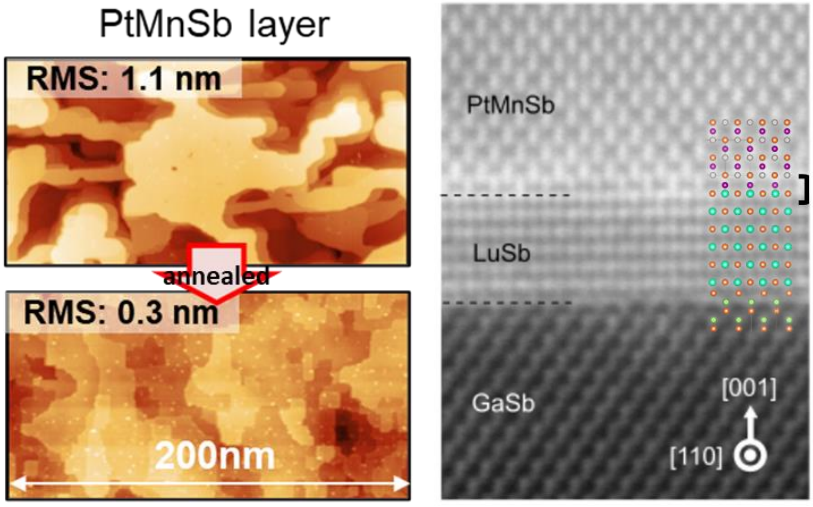

Figure 5.5. (left) *in-situ* STM measurement of the PtMnSb before and after the post-growth annealing step at 350 °C. (right) HAADF-STEM image of a 13nm PtMnSb thin film with post-growth annealing step at 350 °C. STM image courtesy of Jason Dong and HAADF-STEM image courtesy of Aranya Goswami.

Besides the STM measurement and the RHEED image, XRD and the XRD-RSM of the PtMnSb thin film were also measured. Figure 5.6 shows the out-of-plane θ-2θ XRD scan of a 13 nm PtMnSb thin film grown on LuSb buffer layer. Here the substrate peak is marked by asterisks indicating the GaSb (002) and GaSb (004) peaks. The broad peak at the GaSb (002) is the LuSb (002) since the PtMnSb (002) is a weak diffraction peak while the LuSb (002) peak is strong. The PtMnSb (002) peak is likely buried underneath the broad LuSb (002). The lattice constant of the PtMnSb thin film is calculated to be 6.22 Å, which is closely matched with other reported literature work [49, 50]. Besides the expected Bragg peak from the LuSb and PtMnSb peaks, no observation of the additional phases was seen in the XRD measurement and the sample that was grown is single phase.

Figure 5.7 shows the XRD-RSM of the 5, 13, and 33 nm PtMnSb thin film. From the XRD-RSM of (115) Bragg peak we can see that for the thinner PtMnSb (5 and 13 nm), the growth of the PtMnSb is pseudomorphic growth as we can see from the in-plane lattice constant of PtMnSb is matched to that of the GaSb (115) Bragg peak. And it can be seen clearly that the PtMnSb starts to relax as we increase thickness looking at the shifting of the red triangle (which indicate the (115) PtMnSb peak) in the in-plane direction. In addition, the broadening of the peak also indicates the crystallinity of the film becomes worsen as the thickness of the PtMnSb thin film increases.

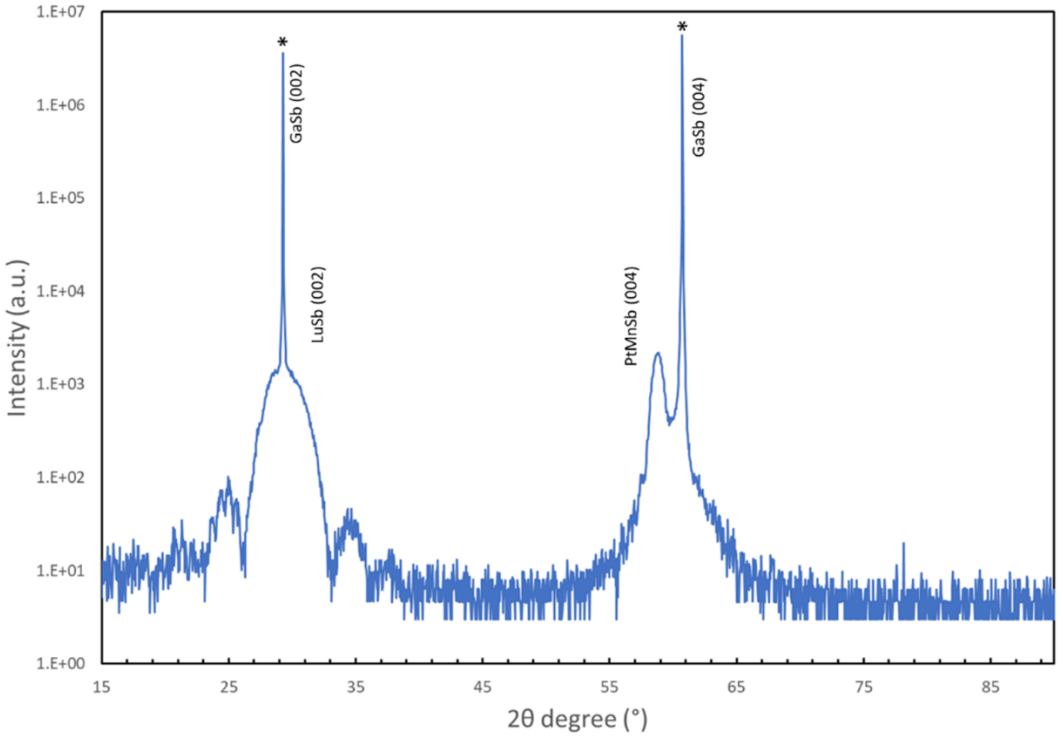

Figure 5.6. out-of-plane θ-2θ XRD scan of a 13 nm PtMnSb thin film grown on LuSb buffer layer. Substrate peaks are marked by asterisks.

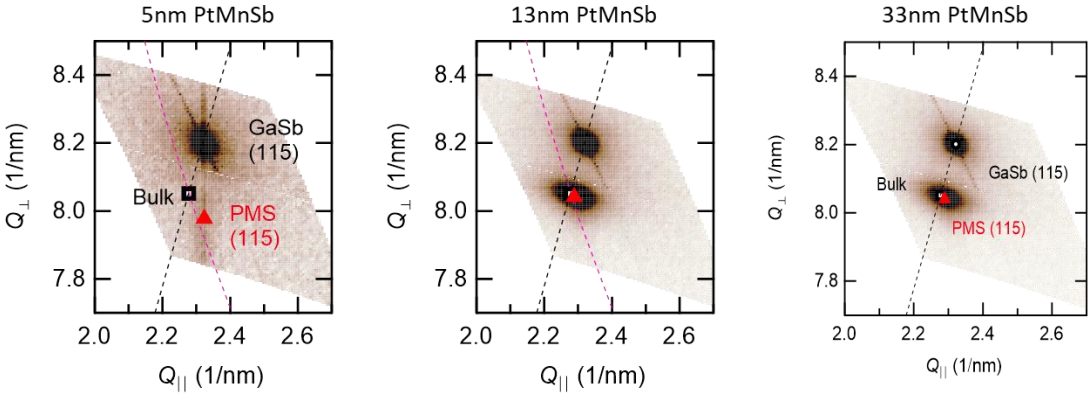

Figure 5.7. XRD-RSM of (left) 5 nm, (middle) 13 nm, and (right) 33 nm thick PtMnSb thin film on LuSb buffer. The red triangle indicates the (115) PtMnSb Bragg peak.

It is believed that this is the first successfully PtMnSb growth using Molecular Beam Epitaxy. The XRD, RHEED, STM, as well as the TEM have provided evidence of a high quality PtMnSb thin film. In order to explore the potential Weyl phases in this material system, we also need to establish the growth of $Pt(Mn_{1-x}Lu_x)Sb$ and ensure that the $Pt(Mn_{1-x}Lu_x)Sb$ phase is stable with the same growth condition. The same growth steps for the PtMnSb thin film was used for the $Pt(Mn_{1-x}Lu_x)Sb$ thin film at various Lu concentration from x = 0 to 0.7.

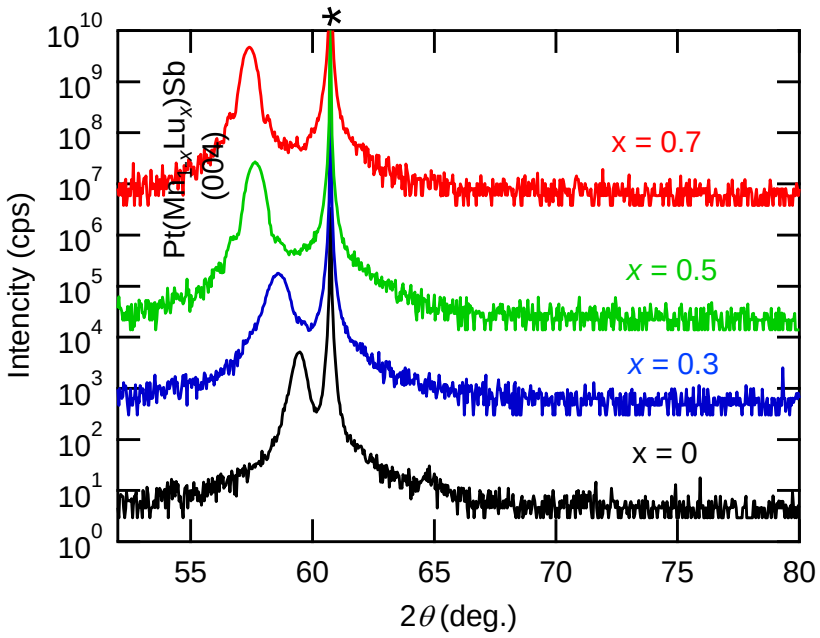

Figure 5.8. out-of-plane θ-2θ XRD scan of various Lu concentration from x = 0 to x = 0.7 of 13 nm $Pt(Mn_{1-x}Lu_x)Sb$ thin film grown on LuSb buffer layer. GaSb (004) Substrate peak is marked by asterisks.

Figure 5.8 shows the out-of-plane θ-2θ XRD scan of a 13 nm $Pt(Mn_{1-x}Lu_x)Sb$ thin film grown on LuSb buffer layer with various Lu concentration of x = 0, 0.3, 0.5, and 0.7.

Similar to the PtMnSb growth, no additional phases were observed from the XRD. However, a shift of Pt($Mn_{1-x}Lu_x$)Sb (004) Bragg peak can be observed toward the lower angle as we increase Lu concentration. The lattice constants of each different Lu concentration are 6.22, 6.29, 6.38, 6.41 Å for x = 0, 0.3, 0.5, and 0.7 respectively, which agreed closely with Vegard's law [101]. This is expected as PtLuSb thin film is expected to have a lattice constant of around 6.46 Å [5].

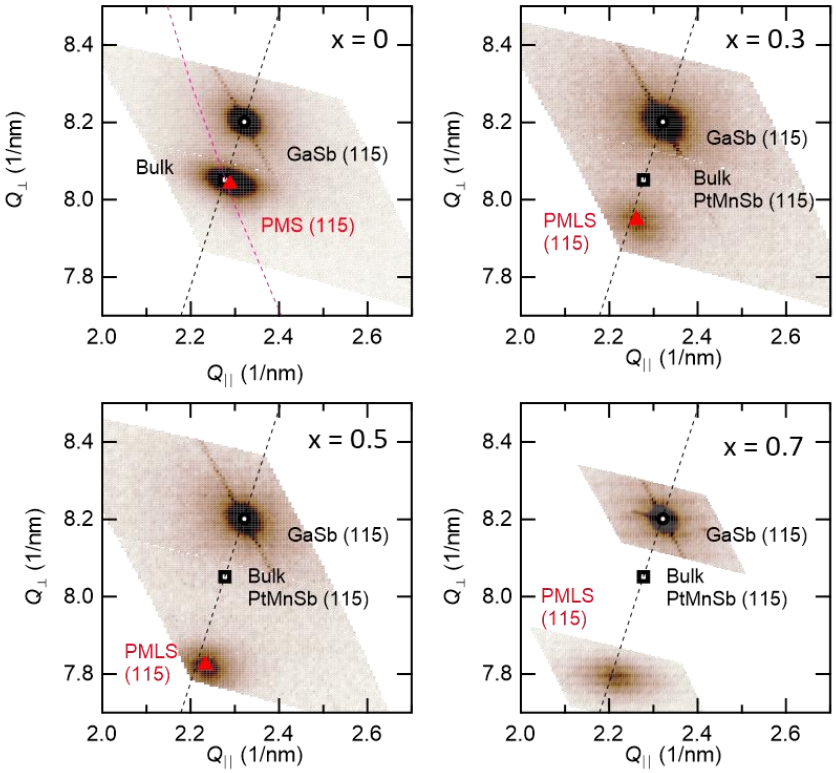

Figure 5.9. XRD-RSM of 13 nm thick Pt($Mn_{1-x}Lu_x$)Sb thin film at various Lu concentration of x = 0, 0.3, 0.5, and 0.7 on LuSb buffer. The red triangle indicates the (115) PtMnSb Bragg peak.

The XRD-RSM of the various Lu concentrations of the 13 nm $Pt(Mn_{1-x}Lu_x)Sb$ thin film were also measured. As expected, all the films apparent to be relaxed in the in-plane direction. On the other hand, the out-of-plane direction is shifting towards the larger lattice constant position as Lu concentration increases, which was exactly what we would expect from figure 5.9. Now, the growth of the PtMnSb and $Pt(Mn_{1-x}Lu_x)Sb$ has been established. The next goal will be examined its transport properties to see if any signature of Weyl phases can be observed with various Lu concentration.

5.3 Transport of PtMnSb and Lu alloyed $Pt(Mn_{1-x}Lu_x)Sb$

5.3.1 Transport analysis of PtMnSb

Before examining the transport of the Lu alloyed PtMnSb thin film, it will be interesting to examine some of the transport properties of the PtMnSb itself. Figure 5.10 shows the temperature dependent resistivity for 5nm, 13nm, and 33nm thick PtMnSb thin film on LuSb buffer. From the temperature dependent resistivity, we can see an over trend such that the resistivity in the low temperature region increases with increasing temperature up to a maximum around 100 K and decreases after reaching the maximum toward the high temperature region. The resistivity eventually flattens out at the high temperature region. This is true for all thickness of PtMnSb measured. GaSb carriers freezing out occurs for

temperatures below 100K. This mean that there is minimum conduction contribution from GaSb substrate at the low temperature region. Thus, the resistivity contribution in the low temperature region is coming mostly from LuSb buffers and PtMnSb conduction. The high temperature region (where the resistance flattens out) is contributed from a mix of LuSb buffer, GaSb substrate, and the PtMnSb conduction. In addition, by removing the contribution of the GaSb conduction, the behavior of the resistivity is metallic like.

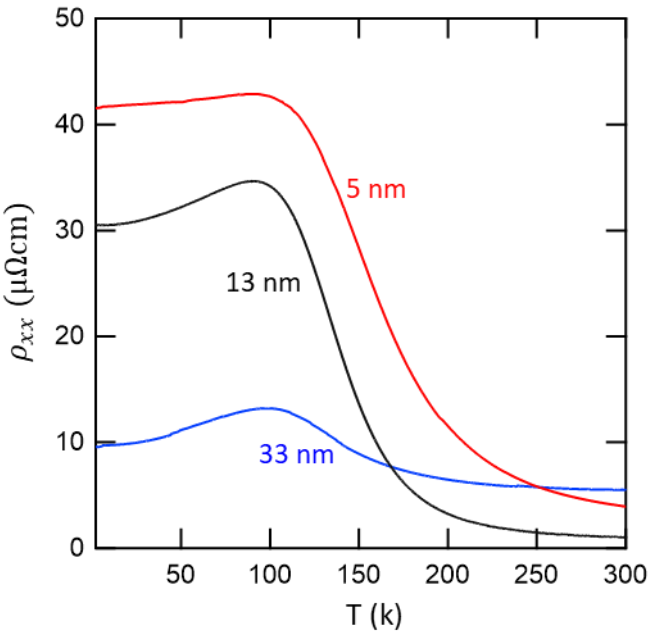

Figure 5.10. Resistivity measurement of PtMnSb thin film as a function of temperature for 5 nm, 13 nm, and 33 nm thick film.

Figure 5.11 shows the Hall resistivity as a function of applied magnetic field at 2K. LuSb buffer grown on GaSb (001) substrate has shown to be an electron type carrier conduction [113]. Based on the shape of the hall measurement, it can be seen that a R_{xy}

bending originating from the two-carrier transport (PtMnSb and LuSb parallel conduction) at the low field region can be observed. As we can see from the 33 nm thick PtMnSb film, the slope of the resistivity is positive, indicating hole type transport. This indicating that the conduction contribution is mainly dominated from PtMnSb, which has a hole type carrier. Similarly, the 13 nm thick PtMnSb film also shows positive slope. However, for the 5 nm PtMnSb thin film, there is a change in the sign of the slope compared to the 13 and 33 nm thick film where the hall resistivity become negative. This is the evidence of where the parallel conduction of the electron carrier type contribution from the LuSb buffer dominated over the hole type PtMnSb conduction. This means that the areal carrier density decreases as the thickness of the film decreases and the contribution of parallel conduction from the LuSb buffer is become more evidential for thinner samples, which is what we would be expecting. As a result, in order to study transport of PtMnSb thin film while using the LuSb buffer, we have to resort to utilize thicker film to prevent the contribution of the parallel conduction from LuSb buffer layer shorting out the PtMnSb layer.

Since this is a two-carrier transport system, one will have to measure the hall resistance measurement of the LuSb buffer layer/GaSb (001) only thin film and obtained the information of electron density and mobility of LuSb. Once the electron density and mobility of LuSb film is determined, one will fit the high field region of the PtMnSb R_{xy} data using the two-carrier ordinary hall effect transport term [114]

$$\mathrm{R_{yx}} = \frac{\mu_1^2 n_1 + \mu_2^2 n_2 + (\mu_1 \mu_2 B)^2 (n_1 + n_2)}{e[(\mu_1 |n_1| + \mu_2 |n_2|)^2 + (\mu_1 \mu_2 B)^2 (n_1 + n_2)^2]} B \qquad (5.1)$$

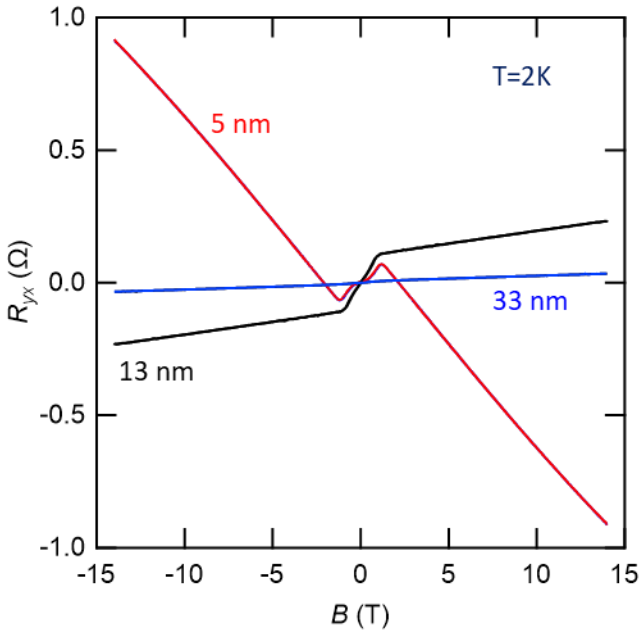

Figure 5.11. hall resistance measurement of PtMnSb thin film as a function of applied magnetic field for 5 nm, 13 nm, and 33 nm thick film at 2K.

Where μ and n corresponding to the mobility and carrier density of LuSb and PtMnSb. Then substrate the term to obtain the R_{AHE}. Figure 5.12 shows both the anomalous hall effect (red curve) as well as the magnetization (blue curve) measurement as a function of applied magnetic field at 2K for hall measurement and 5K for magnetization. From the magnetization measurement, we can see that the saturation magnetization decreases with increases thickness of the thin film for PtMnSb. The saturation magnetizations at 5K are 4.27 μ_B, 3.97 μ_B, and 3.21 μ_B for 5 nm, 13 nm, and 33 nm thick PtMnSb thin film respectively. The calculated magnetic moment for the PtMnSb is expected to be around 3.94 μ_B from theoretical literature [112], which matched closely with the experimental extracted data from this study.

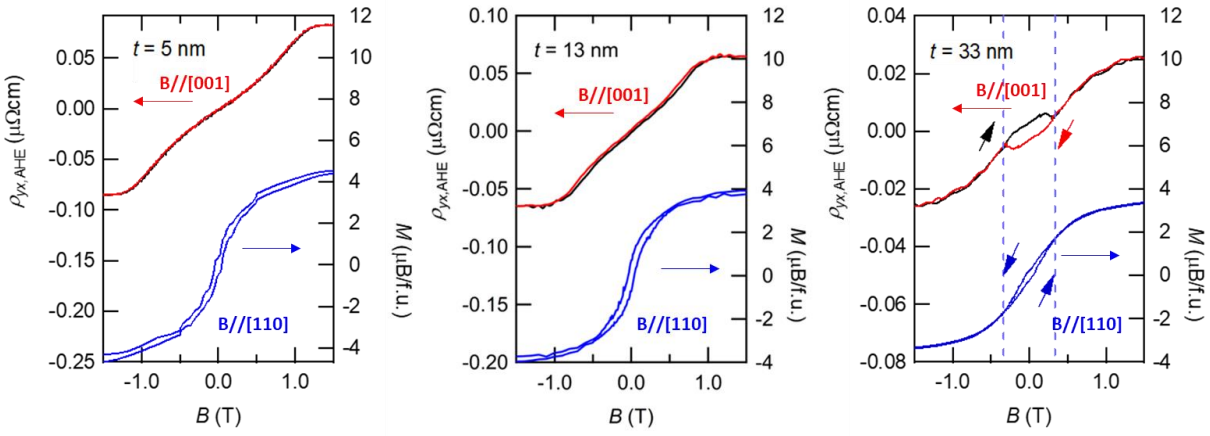

Figure 5.12. anomalous hall effect (black/red curve) and magnetization (blue curve) of PtMnSb thin film as a function of applied magnetic field for 5 nm, 13 nm, and 33 nm thick film at 2K for hall measurement (black/red curve) and 5K for magnetization (blue curve).

For the anomalous Hall effects show in red line in figure 5.12, the value anomalous Hall resistance is very small. The anomalous Hall resistance increases with increasing applied field and flattens out at the high field region. In addition, the anomalous Hall resistance decreases with increasing thickness. Since the slope is positive, the transport of the PtMnSb is that of hole type, which agrees with the Hall resistance measurement. The hole density is calculated to be about 4.41×10^{22} cm^{-3}. One thing to note from the anomalous Hall measurement is that for the 33 nm PtMnSb thin film, a deviation in the anomalous Hall resistance measurement in the low field region between the forward (black line) and the backward (red line) magnetic field sweep can be observed. This deviation is contributed from the formation of either an impurity phase or crystallite of different orientation within the bulk crystal that otherwise was not observed under XRD. These features were observed

for the 33 nm thick PtMnSb film under TEM measurement but not for the 13 nm or 5 nm PtMnSb film as shown in figure 5.13. Thus, 13 nm thickness is used for the Lu alloyed study of $Pt(Mn_{1-x}Lu_x)Sb$ films.

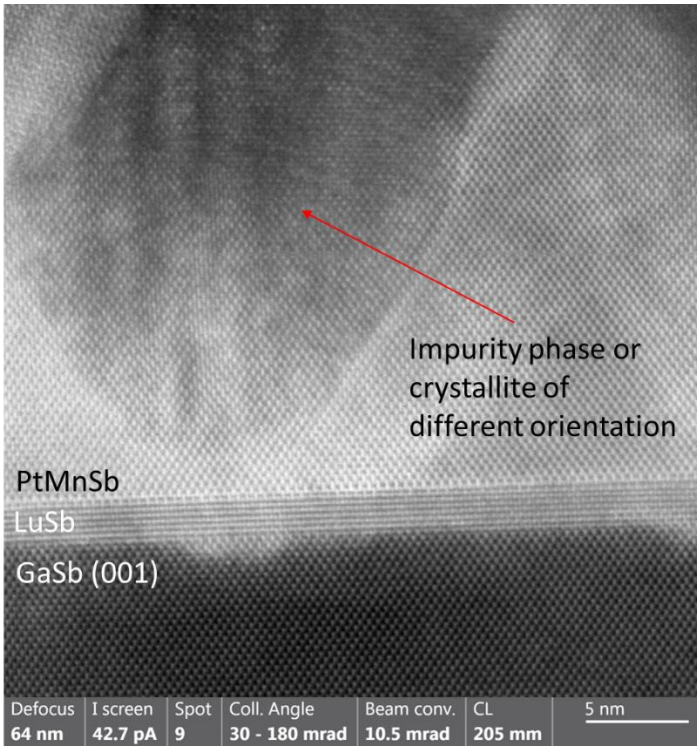

Figure 5.13. TEM image of a 33nm PtMnSb thin film with post-growth annealing step at 350 °C. Observation of the either an impurity phase or crystallite of different orientation within the bulk crystal can be seen throughout the PtMnSb layer. TEM image courtesy of Aranya Goswami.

5.3.2 Lu alloyed effect on Transport of $Pt(Mn_{1-x}Lu_x)Sb$

Substituting the Lu onto the Mn site for the $Pt(Mn_{1-x}Lu_x)Sb$ is expected to affect the magnetic properties of the $Pt(Mn_{1-x}Lu_x)Sb$ film because the magnetic moment of the PtMnSb is heavily dominated by Mn since Pt and Sb do not have magnetic moments. Thus,

it is expected that the $Pt(Mn_{1-x}Lu_x)Sb$ thin films will have decreased magnetic moments and magnetization with higher Lu substitution concentration. Figure 5.14 shows the magnetization as a function of applied magnetic field parallel to the [110] direction at 5K at various Lu concentrations for 13 nm $Pt(Mn_{1-x}Lu_x)Sb$ thin film. As expected, the saturation magnetization decreased with increasing Lu concentration for the $Pt(Mn_{1-x}Lu_x)Sb$.

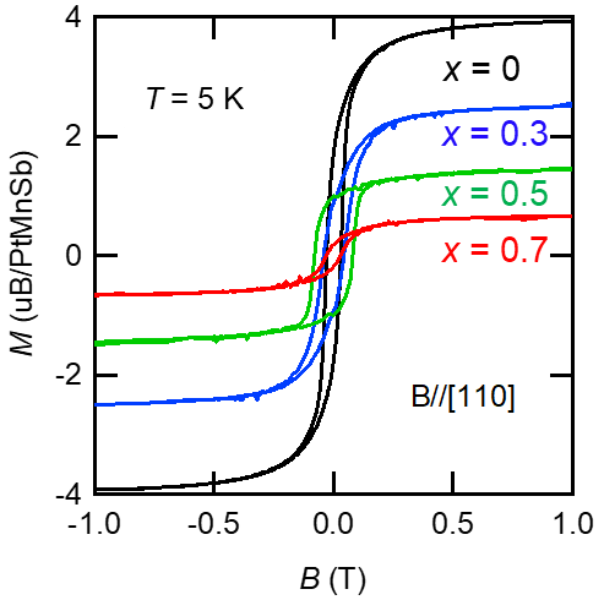

Figure 5.14. magnetization of 13 nm $Pt(Mn_{1-x}Lu_x)Sb$/LuSb/GaSb (001) as a function of applied magnetic field along the [110] direction for Lu concentration of x = 0, 0.3, 0.5, and 0.7 at 5K

Even though the Lu substitution $Pt(Mn_{1-x}Lu_x)Sb$ is expected to result in changes in electronic structure, the decrease in the carrier concentration as a function of increasing Lu substitution extracted from the Hall resistivity measurement as shown in figure 5.15 with

different Lu concentrations in $Pt(Mn_{1-x}Lu_x)Sb$ is not obvious. From the valence electron count of the half Heusler compounds, PtMnSb has 22 valence electrons while for PtLuSb is 18. We would expect PtMnSb to have more electrons than that of the PtLuSb based on the valance electron counting. Based on the carrier concentration calculated from the Hall measurement show in figure 5.15, the conduction type is hole type. This means that the Fermi level is below the band gap. What we would have expected is that by alloying Lu into the PtMnSb, a decrease in the Fermi level would be expected since alloying Lu would mean hole doping of the PtMnSb since Lu has less valence electron than Mn. This mean the hole density will increase with increasing Lu concentration in $Pt(Mn_{1-x}Lu_x)Sb$. By using the two-carrier model from equation 5.1, the carrier mobility and density can be determined. However, from figure 5.15, the hole density is decreasing with increasing Lu concentration in $Pt(Mn_{1-x}Lu_x)Sb$. The effect on the carrier density is opposite of what we would have expected. This opposite effect is likely because of the effects of 1) change in the band structure where the gap between Γ_6 and Γ_8 band is expected to close as observed in the PtLuSb study [108] and 2) Fermi level shift because of Lu alloying. From the shift of the hole density, we would expect the Fermi level to shift upward toward the gap closing direction of the γ_6 and γ_8 band while having the gap closing between the γ_6 and γ_8 band.

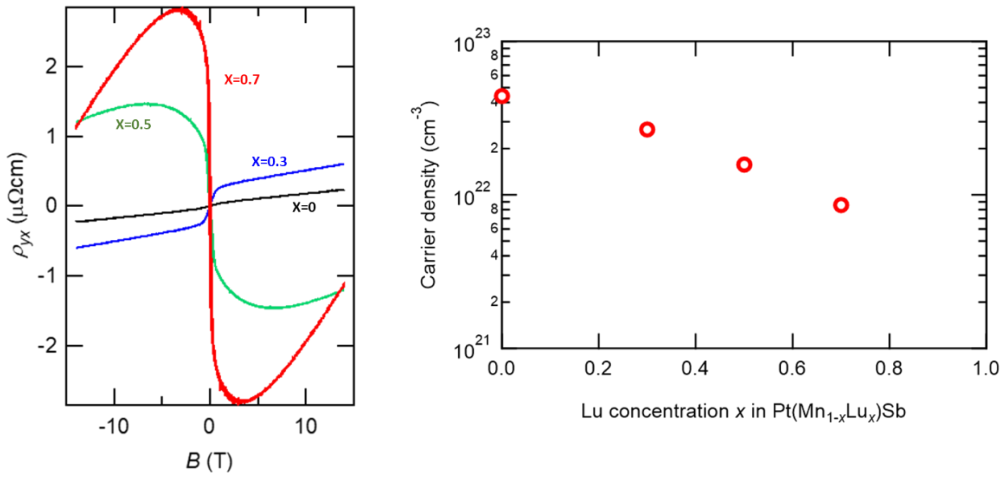

Figure 5.15. (left) Hall resistance measurement of 13 nm Pt($Mn_{1-x}Lu_x$)Sb thin film as a function of applied magnetic field at various x composition at 2K and the (right) hole carrier density extracted from Hall resistance measurement as a function of Lu concentration x in Pt($Mn_{1-x}Lu_x$)Sb at 2K

More interestingly, figure 5.16 shows the anomalous Hall effect measured at various Lu concentration for the 13 nm Pt($Mn_{1-x}Lu_x$)Sb thin film as a function of applied magnetic field at 2K and the anomalous Hall resistance as a function of Lu concentration in Pt($Mn_{1-x}Lu_x$)Sb. For Lu concentration of x = 0 and x = 0.3 (the black and the blue curves), both following the behavior that was previously seen for the PtMnSb thin film where the slope of the anomalous hall resistivity is positive. These curves also following the magnetization curve in figure 5.12, where the magnetic moment align to the applied field direction should results in a positive value at the positive field, which is expected. However, for concentration of x = 0.5 and x = 0.7, the curve is inverted while the slope becomes negative. In addition, the magnitude of the anomalous hall resistivity increases by more than 40 times for the x = 0.5 and more than 100 times for the x = 0.7 compared to the stochiometric PtMnSb thin film.

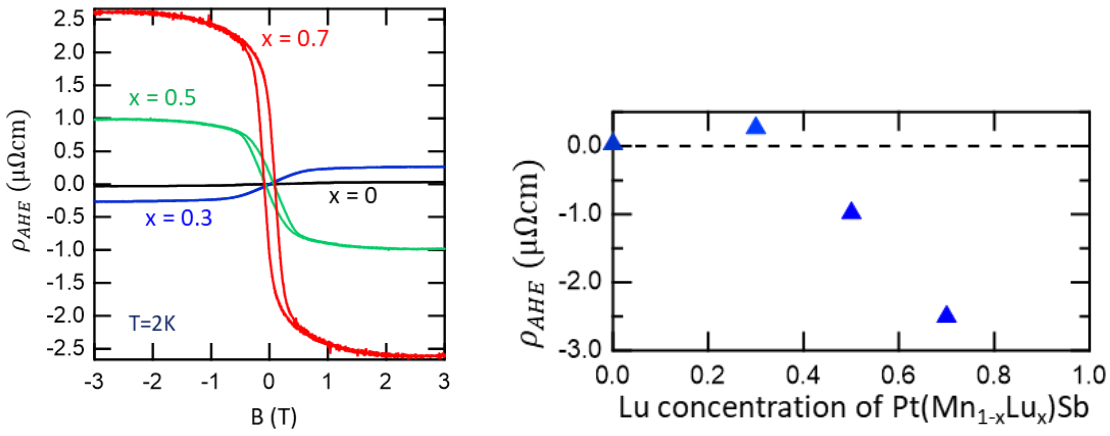

Figure 5.16. (left) anomalous hall resistance of Pt(Mn$_{1-x}$Lu$_x$)Sb thin film as a function of applied magnetic field along the [110] direction for Lu concentration of x = 0, 0.3, 0.5, and 0.7 at 2K and (right) the anomalous hall resistance as a function of Lu concentration x in Pt(Mn$_{1-x}$Lu$_x$)Sb

This sign change of the anomalous Hall resistivity around the Fermi level with increasing Lu concentration means that some bands that contributing to the positive anomalous Hall resistivity is lost while a negative contribution from some other bands is developing. This evidence along with the decrease in the hole density means that there is large change in the band structure at the Fermi level with increasing Lu concentration. What might potentially happen, is that the sign change is because of Weyl point is crossing the Fermi level. To further stress on the topic, figure 5.17 shows the Hall angle plot of anomalous Hall resistivity as a function of resistivity. For a material that possess Weyl semimetallic properties, a large hall angle away from the $\rho_{AHE}/\rho_{xx} = 0.1$ slope is observed [115, 116].

This has been observed for other Weyl semimetal materials such as Co_2MnAl, GdPtBi, and NdPtBi [115, 116]. It means that there is a large Berry phase contribution from the Weyl point to the anomalous Hall effect. However, this observation is also Fermi level dependent since the contribution of the anomalous Hall effect from the Berry phase of the Weyl point decreases drastically as the Fermi level moving away from the Weyl point. But based on what we can see from figure 6.17, there is an increase in Hall angle as we increase the Lu concentration of $Pt(Mn_{1-x}Lu_x)Sb$, which potentially showing the contribution of the Berry phase from the Weyl point. However, the exact effect of Lu alloying cannot be determined from the transport measurement alone. Instead, ARPES measurement of $Pt(Mn_{1-x}Lu_x)Sb$ thin film with various Lu concentrations will be need carefully examined to make conclusive results.

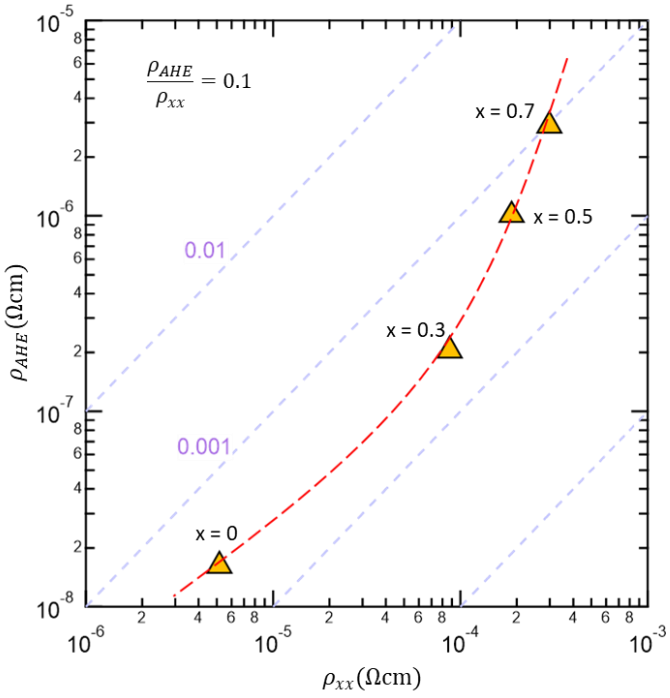

Figure 5.17. hall angle as a function of ρ_{AHE} verses ρ_{xx} for 13 nm $Pt(Mn_{1-x}Lu_x)Sb$ at various Lu concentrations.

5.4 Initial study of ARPES analysis on PtMnSb thin film

The ARPES analysis of the 5 nm PtMnSb thin film on 6 nm LuSb buffer was examined. Figure 5.18 shows the ARPES slice of the PtMnSb along the $\bar{X}-\bar{\Gamma}-\bar{X}$ direction. The APRES measurement of the $\bar{X}-\bar{\Gamma}-\bar{X}$ slice is demonstrated on the left figure of 6.16 where the red line is the $\bar{X}-\bar{\Gamma}-\bar{X}$ slice on the projected first Brillion zone, which corresponds to the $K-\Gamma-K$ in momentum space. This is cutting through the bulk Γ point, which is measured at a photon energy of 55 eV. Figure 5.18 shows the Fermi level cutting through the two spin down (red dotted line) band right at the Fermi level at Γ point.

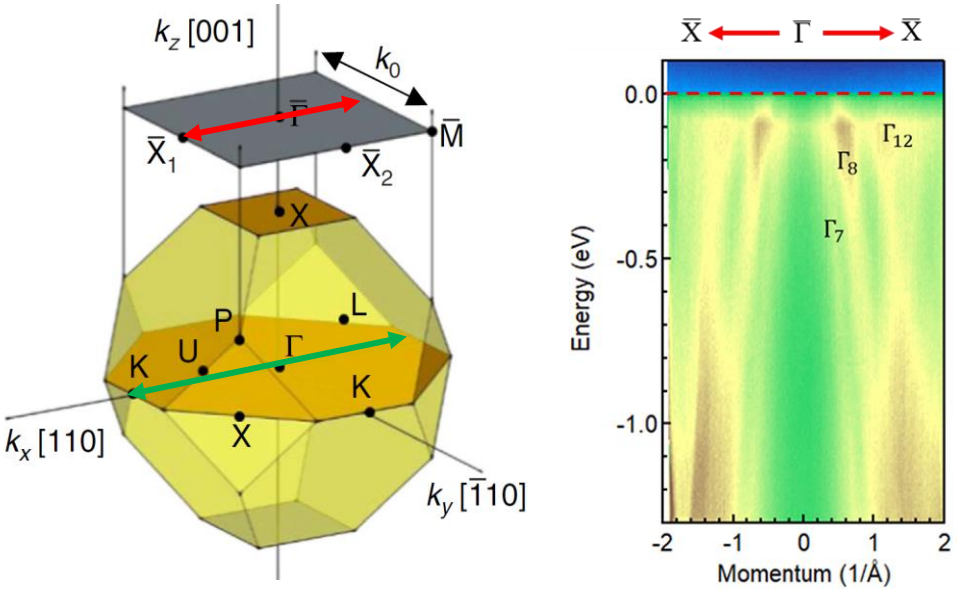

Figure 5.18. (left) Schematics of the bulk Brillouin zone projected to the (001) surface Brillouin zone, showing the projected measured kz plane (black square) at the Γ point and E-k spectra directions (red/Green line). (right) ARPES energy dispersion slices for PtMnSb collected at hv = 55 eV along the $\bar{X}-\bar{\Gamma}-\bar{X}$ direction

The estimated experimentally realized Fermi level is indicated by the green dotted line in figure 5.19 where it is about 0.5 eV below the theoretically calculated Fermi level. By examining figure 5.18, we can see the crossing of the Γ_8, Γ_7, and Γ_{12} band at the Fermi level as indicated on the figure, which matched relatively well with the theoretical calculated band structure.

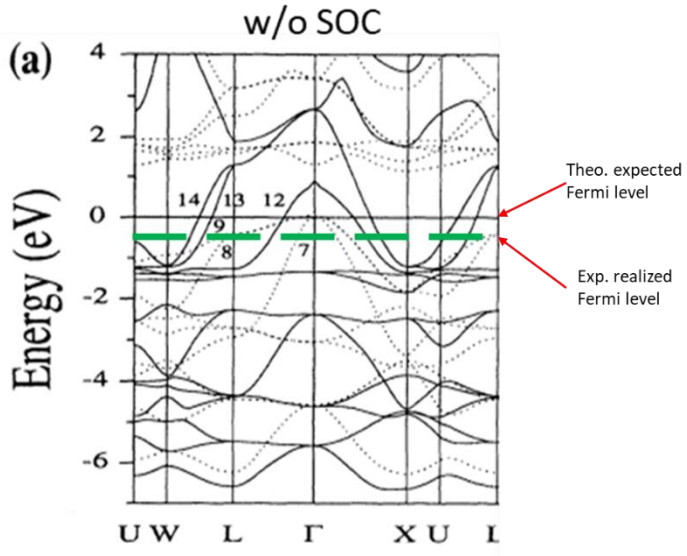

Figure 5.19 First principles calculated bulk electronic band structure of PtMnSb where the black line at $E = 0$ eV is the theoretically expected fermi level and the green dotted line is the experimentally realized Fermi level. Image reprinted from [108] with permission

Unfortunately, the ARPES measurement of the $Pt(Mn_{1-x}Lu_x)Sb$ has not been performed. Thus, at the moment, we cannot draw direct conclusion as to 1) how the band gap between the Γ_6 and Γ_8 are closing, 2) how does the Fermi level shifting with respected to the band gap closing as well as its position with respect to the Weyl point (if any existed), 3) whether or not there is band cross/band inversion that induced Weyl phases with Lu

alloying. But what we can conclude is that we are the first group to stabilize the growth of PtMnSb and the Lu alloyed $Pt(Mn_{1-x}Lu_x)Sb$ with LuSb buffer to form high quality thin film as well as examining the basic characterization of the materials. From transport, by Lu alloying, the band structure is change and the Fermi level is shifting upward toward the band closing direction. These effects results in the change in anomalous hall effect as well as increasing it magnitude but more than 100-fold at high Lu concentrations. In addition, we are also the first group to about to observe the band structure of PtMnSb using ARPES measurement.

Chapter 6

Summary and Future Work

6.1 Summary

In this dissertation, the study of half-metallic full-Heusler compound Co_2TiSn has been performed. Method of growth condition optimization, post-growth annealing process, and Fermi level tuning has been shown in this study. In chapter 3, a systematic study to determine the growth of Co_2TiSn were performed. The growth condition of 450 ˚C with 20 nm thickness was determined. However, under XRD-RSM, it was determined to be

heavily B2 ordering without any additional process. In order to obtain highly ordered $L2_1$ ordering of the Co_2TiSn full-Heusler, the process of post-growth annealing step was taken. The post-growth annealing study shows the Co_2TiSn thin film with the expected c(2x2) surface reconstruction during growth. Under XRD, the expected (002) and (004) Bragg peak can be observed without additional phases. By using XRD-RSM, the observation of the (111) Bragg peak can be observed as annealing temperature increase up to 600 ˚C. For Co_2TiSn thin film, the result from magnetization measurements shows that the low temperature saturated magnetization at $T = 5K$ of $M_S = 1.43\ \mu_B$ and Curie Temperature above 300K can be observed. From the ordinary Hall effect, the measured carrier density of $\sim 10^{22}\ cm^{-3}$ is relatively high, while the carrier mobility of $\sim 2\ cm^2/Vs$ is relatively low, indicating that charge transport in Co_2TiSn is that of metallic, rather than semimetallic as in TaAs or other Weyl semimetals. The extrapolated Berry curvature also only has modest contribution to the intrinsic Anomalous Hall effect. It was concluded that the deviation between the theory and experiment is due to an energy separation of 0.278 eV between the Fermi level and the relevant Weyl point W^1_{110} expected for Co_2TiSn. Thus, the studies utilizing alloying element to shift the Fermi level toward the Weyl point while utilizing the high temperature post-growth annealing process from this chapter to realize the $L2_1$ ordering used in Chapter 4.

In Chapter 4, the method of fermi level tunning is used in order to shift the Fermi level toward the Weyl point for Co_2TiSn thin film. This is done by substituting Ni onto the Co cite. The details of growth have been shown in the chapter. It was shown that the expected c(2x2) Full Heusler surface reconstruction was observed at all Ni doping

composition for $Co_{2-x}Ni_xTiSn$. Under XRD, the expected (002) and (004) peak can be observed without any additional phases. The XRD-RSM present similar results to the result from chapter 4 where a high intensity peak of (111) Bragg peak can be observed for all Ni doped composition. The examination of the surface morphology using STM also has relative smooth surface with no observation of any surface dislocation. Lastly, the resistivity as well as magnetotransport of Co_2TiSn and Co_2-xNi_xTiSn were compared. The results showed that both resistivity and Hall resistance increased with Ni alloying. However, no obvious signature of Berry curvature contribution from the Weyl point was observed from the transport measurements with Ni concentration up to $x = 0.20$. It is likely due to the fact that $x = 0.2$ of Ni doping was not enough to shift the Fermi level to the Weyl point as calculated from the theoretical analysis. Thus, the study of using Angle-Resolved Photoemission Spectroscopy (ARPES) was used in order to determine the effect of Ni-alloying on Fermi level tuning in Co_2TiSn thin film. APRES measurement of Co_2TiSn and its respective Ni-doped thin films were examined. APRES measurement of Co_2TiSn and $Co_{2-x}Ni_xTiSn$ thin film shows promising result in observing its electronic structure. In addition, it was also determined that a Ni doped of $x = 0.16$ shifts the Fermi level by about 161 meV. This confirms the method of growth and post-growth annealing step in Chapter 3 and the Fermi level tuning method in Chapter 4 was successful. However, in order to observe the Weyl point, Co_2TiSn thin film with more than 20% Ni alloying is required in order to shift the Fermi level to the Weyl point and determine if any Fermi arc and Weyl points can be observed using ARPES.

Lastly, Chapter 5 shows the study on the PtMnSb and Lu-alloying PtMnSb. Using MBE growth on GaSb (001) substrate and adopting LuSb as buffer layer, epitaxial films of PtMnSb (001) single phase can be achieved. The structure and morphology of the PtMnSb was examined using TEM and STM. The TEM image shows very abrupt and smooth interfaces between the PtMnSb/LuSb and LuSb/GaSb layers. The STM image of PtMnSb thin film shown large terraces with a root mean square of the surface roughness of 0.3 nm. From the magnetization measurement, saturation magnetizations at 5K are 4.27 μ_B, 3.97 μ_B, and 3.21 μ_B for 5 nm, 13 nm, and 33 nm thick PtMnSb thin film respectively. The calculated magnetic moment for the PtMnSb is expected to be around 3.938 μ_B from theory [103], which matched closely with the experimental extracted data from this study. The transport of the PtMnSb is that of hole type with a carrier density of 4.41×10^{22} cm^{-3}. For the Lu alloyed PtMnSb, the study demonstrated the alloy films of $PtMn_xLu_{1-x}Sb$ with various Lu concentration x can be achieved by MBE growth on the LuSb-buffered GaSb (001) substrate. In addition to the systematic change of lattice constant, magnetic moment and hole density as increasing Lu concentration, low temperature Hall measurements reveal enhancement of anomalous Hall effect (AHE), and in particular, a sign change of anomalous Hall resistivity ρ_{AHE} around x = 0.35. Such enhancement/sign change of AHE with reducing the magnetization by Lu doping, strongly indicates significant modulation of intrinsic Berry phase, which is sensitive to the low-energy band structure change such as band inversion/Weyl point formation during the topological phase transition from a half metal to a topological insulator.

6.2 Future Work

With the growth method, post-growth annealing process, and Fermi level tunning from this study, further study of using higher Ni-doping composition to shift the Fermi level by 278 meV toward the Weyl point is promising. As show in Figure 6.1, the Hall angle plot of the ρ_{xx} as a function of Anomalous Hall resistance ρ_{AHE} is shown. The dot points show the result from the magnetotransport measurement of Co_2TiSn and $Co_{1.8}Ni_{0.2}TiSn$ thin film and several Co_2TiGe thin film at various post-growth annealing temperature. By further increasing the Ni-doping composition beyond $x = 0.2$, the Hall angle for Co_2TiSn should follow the predicted gray curve shown in the figure 6.1.

The maximum of the curve is where the contribution from the Berry curvature is the greatest. That will be the composition where Fermi level is tuned right at the Weyl point. As a result, a systematic study of higher Ni-composition alloying beyond 20% to Ni_2TiSn should be applied in order to determine precise composition of Ni doping that is needed to shift the Fermi level right at the Weyl point.

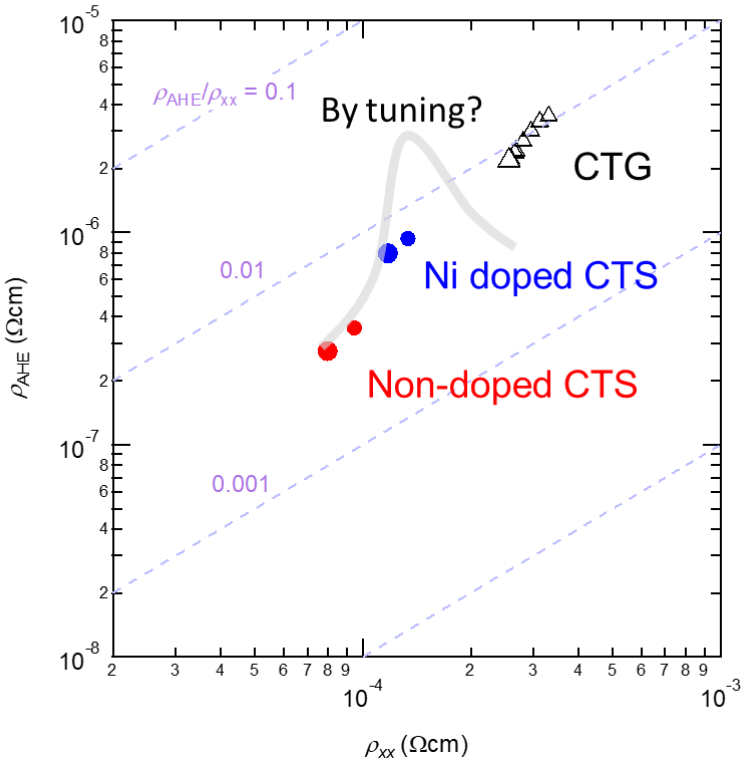

Figure 6.1: Hall angle plot of the ρ_{xx} as a function of Anomalous Hall resistance. The result from the Co_2TiSn and $Co_{1.8}Ni_{0.2}TiSn$ and several Co_2TiGe at various post-growth annealing temperature were shown. By further tuning the Fermi level with higher Ni-doping, a predicted curve shown in gray is expected to be observed with its maximum apparent when the Fermi level is at the Weyl point.

After determining the exact Ni composition that is needed for Co_2TiSn, a comprehensive study of the electrical and magnetotransport should be conducted in order to see if any observation of Weyl semimetallic behavior occurs such as: negative longitudinal magnetoresistance, giant anomalous Hall effect, and high contribution of Berry curvature in anomalous Hall effect. In addition, the method of using other lattice matched buffer layer such as thin layer of Cr buffer on top of MgO substrate or using rare-earth monopnictides such as LuSb buffer can significantly improve the surface morphology

of the overlaying Co_2TiSn thin film. Unlike those of the III-V substrate, LuSb buffer layers are less susceptible to high temperature annealing step and are also relatively well lattice matched to Co_2TiSn. This can provide a new direction in order to obtain sharper bands in ARPES spectral density and allows more precise measurement of the Fermi-level tuning as well as potential observation of the Weyl points. Similarly, since there was an observation of the enhancement/sign change of AHE in Lu-alloyed PtMnSb, it means that a potential band inversion/Weyl point formation can occurred with increasing Lu concentration. Thus, in order to observe the change in the band structure, detailed ARPES measurement and Fermi mapping will be desired to understand how Lu-alloying affected the band evolution of the PtMnSb thin film and whether a topological phase transition occurred from the band inversion/Weyl point formation.

Appendix A - *RBS analysis*

Overview

Rutherford backscattering spectrometry (RBS) is a non-destructive measurement that allows the measurement of thin film thickness, composition at the surface, and contamination. A beam of high energy ion, such as $^4He^+$ particles, is accelerated towards the sample surface. Some of the incident ions are backscattered elastically and collected by a detector. The change in the energy of the scattered particles depends on the masses of then incoming and target atoms, which can be expressed in the following equation [117],

$$E = k^2 E_o \tag{A.1}$$

$$k = \frac{\left(M_1 \cos(\theta) + \sqrt{M_2^2 - M_1^2 \sin^2 \theta}\right)}{M_1 + M_2} \tag{A.2}$$

Where E is the residual energy of the scattered particles, E_o is the energy of the incident ions, M_1 is the mass of the incident particles, M_2 is the mass of the target atom, θ is the scattered angle of the scattered particle, and k is the kinematic scattering factor. With known particle masses, scattering angle, and incident energy of ions, one can analyze the energy spectrum collected from the detector, where the intensity of ions detected are plotted as a function of their kinetic energy.

Helium is typically used as the incident high energy ions because it does not scattered at the surface lose energy as they traverse the solid. They lose energy due to interaction with

electron in the target. Thus, it is also important to understand the energy loss as the ions traverse the solid. For thin film analysis, it is typically assume that the total energy lost ΔE into depth t is only proportional to t for a given target, which can be written as

$$\Delta E = \Delta t \left(k \frac{dE}{dx_{in}} + \frac{1}{\cos\theta} \frac{dE}{dx_{out}} \right) \quad \text{(A.3)}$$

Where $\frac{dE}{dx_{in}}$ and $\frac{dE}{dx_{out}}$ defined as the energies at which the rate of loss of energy for the inward path and exiting path. For the constant $\frac{dE}{dx}$ approximation, the total energy loss becomes linearly related to depth t. From the plot of intensity as a function of kinetic energy, one can determined the $\frac{dE}{dx_{in}}$, $\frac{dE}{dx_{out}}$, and ΔE to determined Δt, which then is the thickness of the target [117].

RUMP software

Analysis of Rutherford backscattering spectrometry (RBS) is an essential part of this work. This appendix will provide an instruction to perform a high-quality fit to an example experimental RBS data using the RUMP software [88]. However, this is only one of many methods to analyze RBS data and is only intended to present the method that was used for this study. Analysis of a 1-hour growth CoTiSn sample will be presented here. When first conducting the RBS data measurement, one will need to first determine the position of the energy channel for each element within a single sample. In the case of CoTiSn, it is important to make sure none of the peaks are overlapping. In order to do so,

we will start by creating a theoretical layer of sample by the following commands in figure A.1:

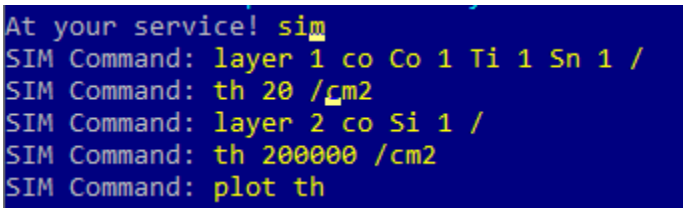

Figure A.1: The code lines for creating a simulating layer of a 20 $\times 10^{15}$ atoms cm^{-2} thick CoTiSn on a Si substrate in RUMP

The SIM command allows you to create a simulated RBS data with multiple layers of materials included. In the above example, a layer of CoTiSn with 20×10^{15} atoms/cm^2 thickness as well as a layer of Si substrate were made. The thickness of the Si substrate layer can be made abstractly as long it's thick enough that it does not affect the background of the analysis. With this, you will obtain a plot with the following result:

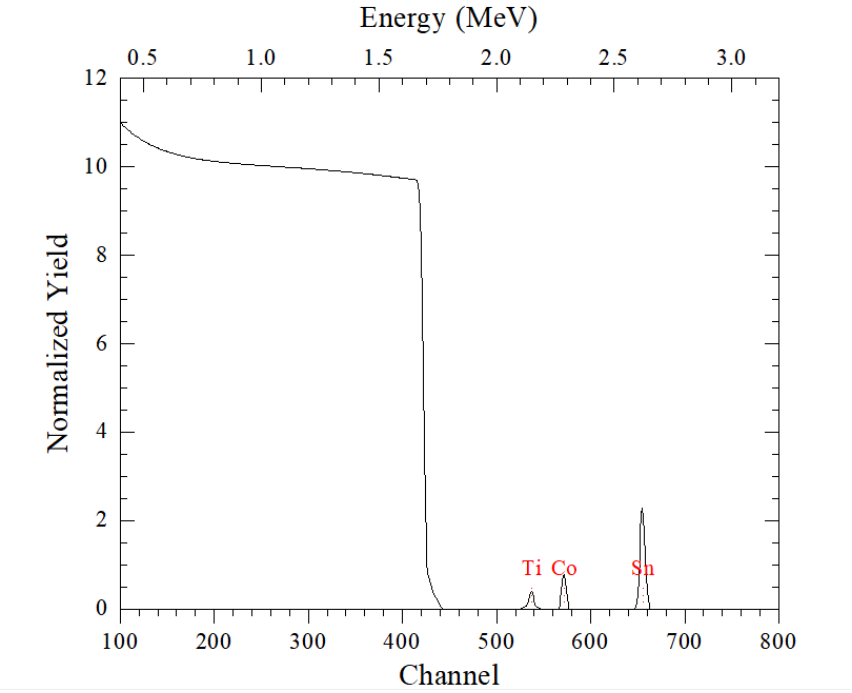

Figure A.2: The RBS plot from the simulated data of a 20×10^{15} atoms cm^{-2} thick CoTiSn on a Si substrate in RUMP

Evidently, we can see that the energy channel spacing among the three elements is great enough that it is unlikely for them to overlap with a reasonable thickness of sample. With this in mind, a set of RBS samples for CoTiSn at various flux value can be grown and examined. After obtained the RBS data from RBS facility, the data is inputted into the Genplot RUMP freeware either by the "Read" command if the data comes in the format of RUMP text file or "Swallow" if the data comes in the form of other excel/text data file.

After the data is inputted into RUMP, the next is creating the simulated RBS data to fit to the actual experimental results.

```
2048 points entered into buffer 1
Yes dear? sim
SIM Command: layer 1 co Co 1 Ti 1 Sn 1 / th 50 /cm2
SIM Command: layer 2 co Si 1 / th 200000 /cm2
SIM Command: show
  #         Thickness         Sublayers     Composition  . . .
   1          50.00  /CM2        auto         Co   1.000     Ti   1.000
                                              Sn   1.000
*  2      200000.00  /CM2        auto         Si   1.000
================================================================================
SIM Command: region 100 800
Your wish? plot 1 ov th
```

Figure A.3: The code lines for creating a simulating layer of a 50 cm^{-2} thick CoTiSn on a Si substrate and plot over the actual experimental data in RUMP

Here we created a simulated layer a 50 cm^{-2} thick CoTiSn on a Si substrate and plot over the actual experimental data. However, this is incomplete as the experimental parameter for the RBS measurement is not included. With the active command, one can access the measurement parameters

```
Hey, man, what next? active
  RBS  File:    dummy.rbs
  Identifier:   Initialized buffer
  LTCT Text:
  Date:
  Beam:         2.000 MeV   4He++     10.00 uCoul  @  0.00 nA
  Geometry:         IBM  Theta:    3.00  Phi:   15.00  Psi:    0.00
  MCA:          Econv:   3.220   50.000  First chan:  0.0  NPT: 2048
  Detector:     FWHM: 25.0 keV  Tau:  5.0   Omega: 4.000
  Correction:   0.5100
```

Figure A.4: The active parameters of the experimental RBS measurement

Now by inputting the correct parameter from the experimental work as shown in figure A.4, the resulting plot becomes

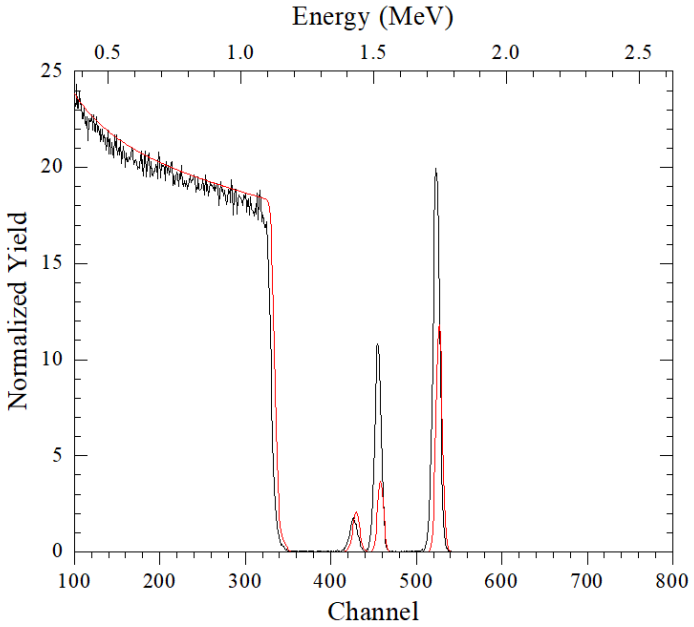

Figure A.5: The RBS plot for a simulating layer of a 50×10^{15} atms cm^{-2} thick CoTiSn (show in red line) on a Si substrate and plot over the actual experimental data (show in black line) in RUMP after matching the experimental parameters with the simulated data set

From here on, some fine adjustment between the "Econv", "FWHM", and "correction" will help the simulated data to match the edge of each plot. (Econv is channel-to-energy conversion and FWHM is full wide half maximum). The following plot shows the simulated data after fitted to the curve edge of the Si front.

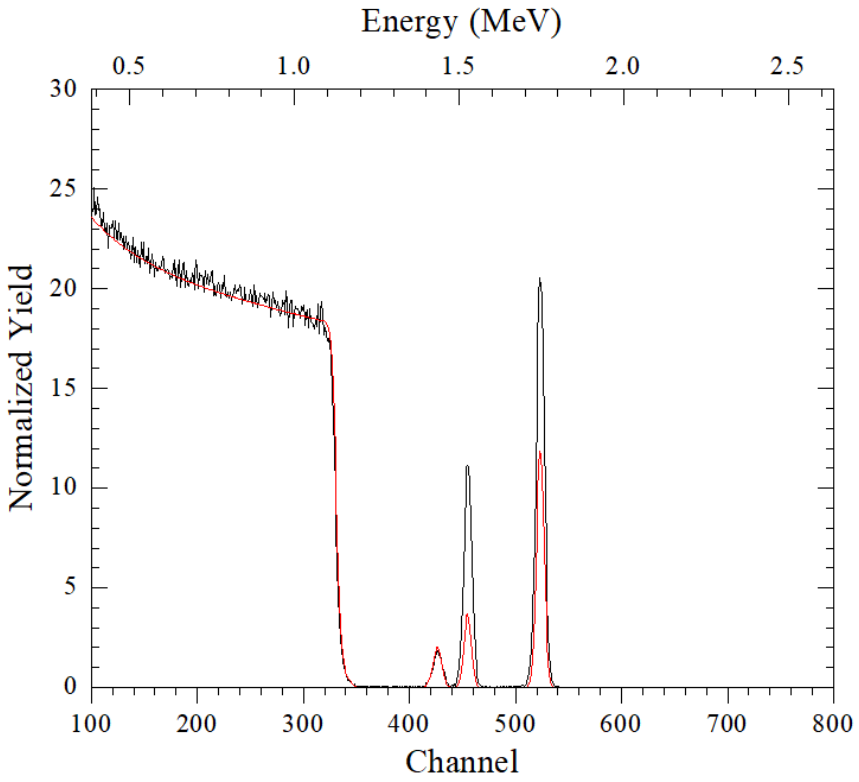

Figure A.6: The RBS plot for a simulating layer of a 50 $\times 10^{15}$ atmscm^{-2} thick CoTiSn (show in red line) on a Si substrate and plot over the actual experimental data (show in black line) in RUMP after adjusting FWHM, Econv, and correction parameters

With this, one can started fitting the simulated data to the RBS data. Generally, two methods can be used: 1) by using the built-in Perturbation command or 2) by adjusting the simulated data between the ratio of the element, the thickness of the sample layers, and the FWHM. We will be using the latter method as the built-in Perturbation command can often go into an infinite loop when it trying to fit the data. After the fitting, the resulting simulated data should match well with the actual data as show in the figure below

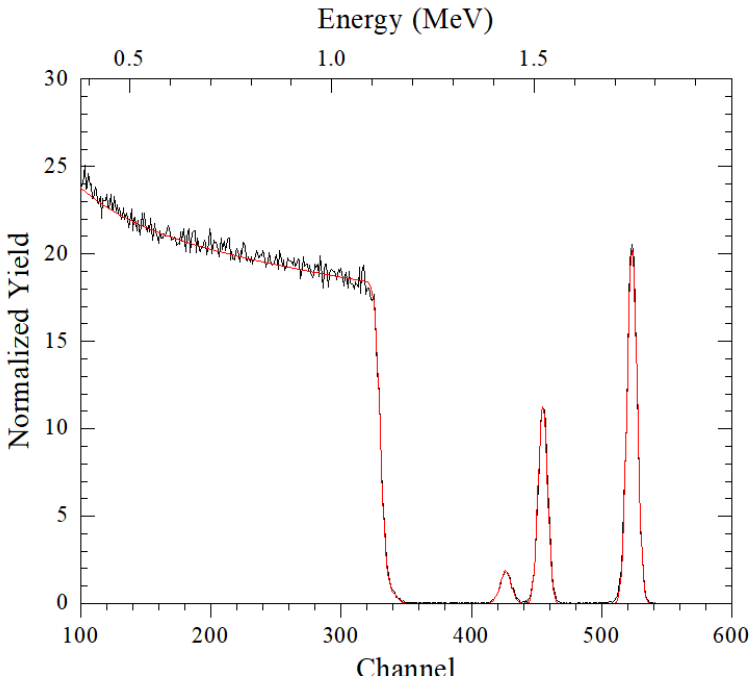

Figure A.7: The RBS plot for a simulating layer of a 50 cm^{-2} thick CoTiSn (show in red line) on a Si substrate and plot over the actual experimental data (show in black line) in RUMP after adjusting the simulation layer's thickness and composition

With this, one can analysis each peak area by using the "thickness" command to obtain the Gross and net thickness of each element's peak area.

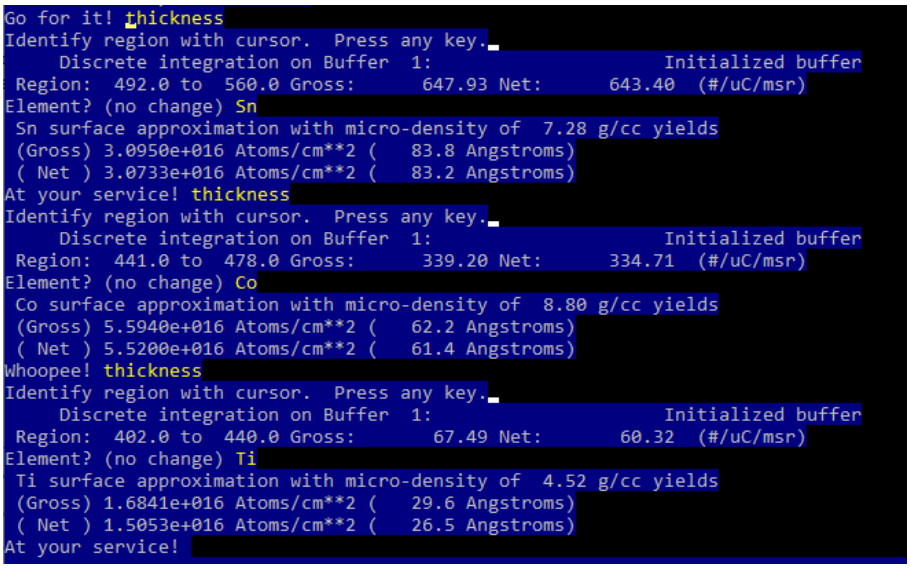

Figure A.8: The thickness command that allows the calculation of peak area for each individual simulation peak in order to determine the total thickness of each element in the unit of atom/cm^2. This data along with the total growth time can be used to determine the flux rate of each element at various temperatures.

Appendix B

Restarting of Metal-Organic Molecular Beam Epitaxy (MOMBE)

Majority of my first-year research work in the Palmstrøm Research Group have been heavily revolved around the restarting of the Metal-Organic Molecular Beam Epitaxy (MOMBE) chamber system. The status of the MOMBE chamber was in an idle state with many parts and components been broken or in needed of repair. The below timeline shows

some of the highlighted work that was done on the MOMBE chamber as well as the metals chamber during year 1 and 2.

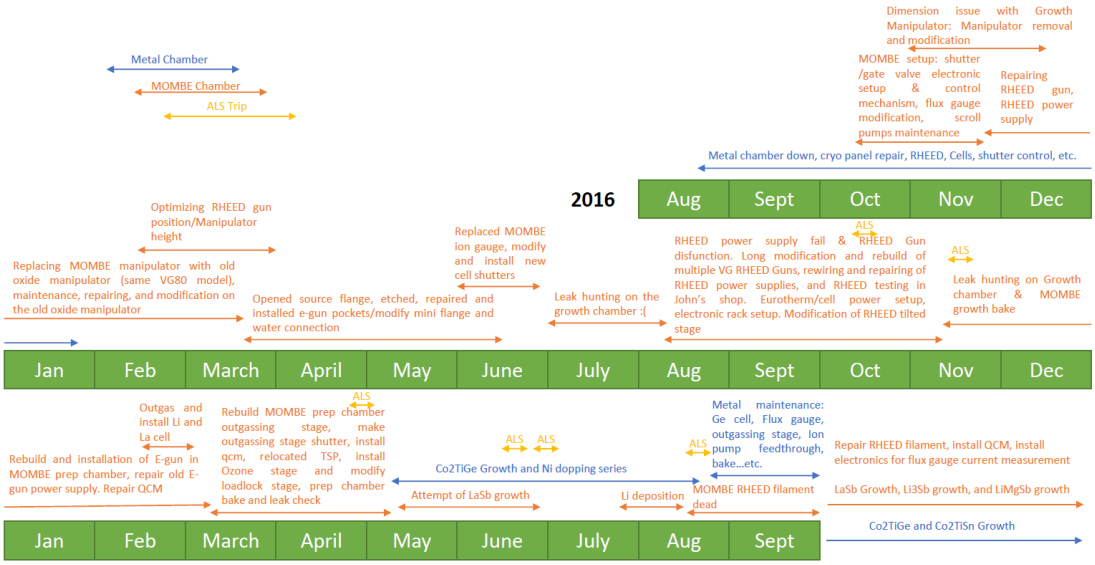

Figure B.1: Timeline shows some of the highlighted work that was done on the MOMBE chamber as well as the metals chamber during year 1 and 2

Since I have no prior experience of UHV equipment, working on an MBE system is a new experience for me. During the first year, I was mainly learning maintenance work of the MBE system from other group members as well as other UHV equipment. Additionally, an incident on the metals chamber that required a full vent to remove the damaged cryopanel. This work includes the removal of the cryopanel from the MBE system, removal and reinstallation of each individual cell as well as refilling new source materials, rebuilding of the flux gauge, replacement of RHEED filament, and rebuilding of the shutter control and units for each cell. With this knowledge, I started to focus on restarting the MOMBE system. Several major issues arouse after the first check up on the system: many shutter/gate-valve electronic controls were not setup properly, flux gauge was broken,

RHEED gun and RHEED power supply were not working, growth manipulator height was incorrect to allow the usage of the RHEED beam to reflect on the sample. The figure below shows the measurement of the manipulator to that of the manufacturing dimension.

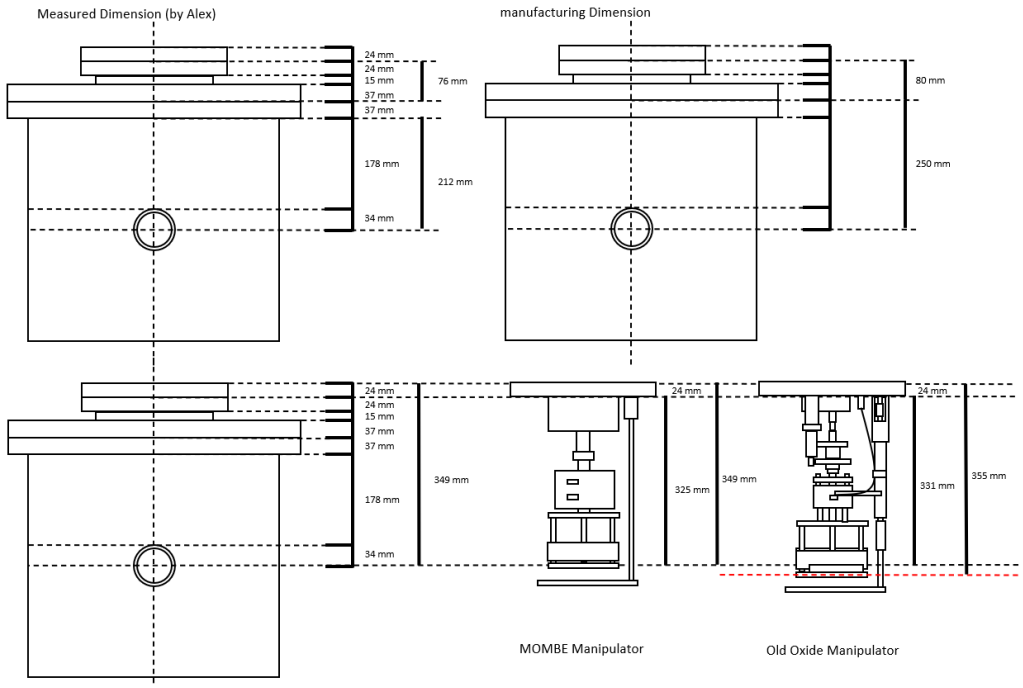

Figure B.2: dimension of the MOMBE manipulator and the manufactured spec

It was found out that the original MOMBE manipulator was slightly too high such that the tilt angle that is require for the RHEED beam to hit the sample is beyond the capacity of the tilt stage. As a result, the manipulator has to be taken apart and additional Moly parts were required to extend the manipulator stage downward by about 24 mm to have enough height for the RHEED beam to reflect on the sample. In addition, a major cleaning and etching of the Moly and tantalum part from both the growth manipulator as well as the preparation chamber manipulator had to be done.

Appendix C

Vacuum Suitcase

Vacuum suitcase plays a vital role in this work. It allows the transferring of the thin film samples from the Palmstrøm lab facility to either the Advanced Light Source at Lawrence Berkeley National Laboratory or SLAC at Stanford University without breaking the vacuum.

Figure C.1: The ALS vacuum suitcase and its power supply

Figure C.1 shows the construction of the ALS vacuum suitcase. As it can be seen from the figure, the vacuum suitcase is composed of 4 components: 1) an adjustable bellow section that is used to attach to the ALS preparation chamber. The bellow section is required in order to make fine adjustment for the transfer arm to pass through the chamber loading port. 2) A double gate valve with a vented port. This is an important component because the bottom gate valve helps to keep the vacuum section clean while being exposed to the atmosphere during transfer. It also gives additional protection to leaks as well as outgassing of the gate valve toward the storage section during bake out. 3) The transfer arm and the storage section which is where the sample are stored. More specifically, they are stored in a cassette that is sitting at the end of the transfer arm. 4) The pumping unit; a NEXTorr UHV Getter pump (NEG) is used that allows a pressure as good as $<5\times10^{-11}$ torr to be maintained. With all these components, the vacuum suitcase is loaded with samples in our APRES loading chamber and transferred to the ALS beamline by car. Figure C.2 shows the vacuum suitcase loaded onto the preparation chamber at the ALS 10.0.1.2 beamline. The bottom port of the bellow section is mounted onto the gate valve of the preparation chamber. The bellow section is then pumped out through the bottom gate valve's vent port using a turbo pump and baked over night at a temperature between 80-120 ℃. A fan is used to blow over the upper gate valve section to ensure no significant outgas from the first gate valve can occur while baking the lower section. The overnight bake can typically bring the bellow section to a pressure of around low 10^{-8} to high 10^{-9} torr. This bellow section is cooled down in the morning and open to the preparation chamber before opening up to the transfer arm and cassette for sample transferring.

Figure C.2: The ALS vacuum suitcase when installed on the 10.0.1.2 beamline preparation chamber

Bibliography

[1] T. Graf, C. Felser, and S. S. P. Parkin, “Simple rules for the understanding of Heusler compounds,” *Prog. Solid State Chem.* **39** (1), 1–50 (2011), doi: 10.1016/j.progsolidstchem.2011.02.001.

[2] M. I. Katsnelson, V. Y. Irkhin, L. Chioncel, A. I. Lichtenstein, and R. A. de Groot, “Half-metallic ferromagnets: From band structure to many-body effects,” *Rev. Mod. Phys.*, **80** (2), 315 (2008), doi: 10.1103/RevModPhys.80.315.

[3] J. Winterlik, G. Fecher, A. Thomas, and C. Felser, “Superconductivity in palladium-based Heusler compounds,” *Phys. Rev. B*, **79** (6), 64508 (2009), doi: 10.1103/PhysRevB.79.064508.

[4] H. C. H. Kandpal, C. Felser, and R. Seshadri, “Covalent bonding and the nature of band gaps in some half-Heusler compounds,” *J. Phys. D: Appl. Phys.*, **39** (5), 776 (2006), doi: 10.1088/0022-3727/39/5/S02.

[5] J. A. Logan, S. J. Patel, S. D. Harrington, C. M. Polley, B. D. Schultz, T. Balasubramanian, A. Janotti, A. Mikkelsen, and C. J. Palmstrøm, “Observation of a topologically non-trivial surface state in half-Heusler PtLuSb (001) thin films,” *Nat. Commun.* **7**, 11993 (2016), doi: 10.1038/ncomms11993.

[6] Z. Wang, M. G. Vergniory, S. Kushwaha, M. Hirschberger, E. V. Chulkov, A. Ernst, N. P. Ong, R. J. Cava, and B. A. Bernevig, “Time-Reversal-Breaking Weyl Fermions in Magnetic Heusler Alloys," *Phys. Rev. Lett.*, **117** (23), 236401 (2016), doi: 10.1103/PhysRevLett.117.236401.

[7] G. Chang, S.-Y. Xu, H. Zheng, B. Singh, C.-H. Hsu, G. Bian, N. Alidoust, I. Belopolski, D. S. Sanchez, S. Zhang, H. Lin, and M. Z. Hasan, “Room temperature magnetic topological Weyl fermion and nodal line semimetal states in half-metallic Heusler Co2TiX (X=Si, Ge, or Sn)," *Sci. Rep.*, **6**, 38839 (2016), doi: 10.1038/srep38839.

[8] J. M. Kosterlitz, D. J. Thouless, “Long range order and metastability in two dimensional solids and superfluids. (Application of dislocation theory),” *J. of Phys. C: Solid State Phys.* **5**, L124 (1972), doi: 10.1088/0022-3719/5/11/002

[9] J. M. Kosterlitz, D. J. Thouless, "Ordering, metastability and phase transitions in two-dimensional systems," *J. of Phys. C: Solid State Phys.* **6**, 1181 (1973), doi: 10.1088/0022-3719/6/7/010

[10] The Nobel Prize in Physics 2016. NobelPrize.org. Nobel Prize Outreach AB 2022. Mon. 12 Sep 2022. https://www.nobelprize.org/prizes/physics/2016/summary/

[11] J. Li, F. Jiang, B. Yang, X. R. Song, Y. Liu, H. H. Yang, D. R. Cao, W. R. Shi, G. N. Chen, "Topological insulator bismuth selenide as a theranostic platform for simultaneous cancer imaging and therapy," *Sci. Reports*, **3**, 1998 (2013), doi: 10.1038/srep01998.

[12] G. Roberts Jr., "Topological Matters: Toward a New Kind of Transistor." https://newscenter.lbl.gov/2018/12/10/topological-matters-toward-a-new-kind-of-transistor/

[13] T. Su, R. P. Scott, S. S. Djordjevic, N. K. Fontaine, D. J. Geisler, X. Cai, and S. J. B. Yoo, "Demonstration of free space coherent optical communication using integrated silicon photonic orbital angular momentum devices," *Optics Express*, **20** (9), 9396-9402 (2012), doi: 10.1364/OE.20.009396.

[14] M. J. Gilbert, "Topological electronics," *Comm. Phy.*, **4**, 70 (2021), doi: 10.1038/s42005-021-00569-5.

[15] L.D. Anh, K. Takase, T. Chiba, Y. Kota, K. Takiguchi, M. Tanaka, "Elemental topological Dirac semimetal α-Sn with high quantum mobility," *Adv. Mat.*, **33** (51), 2104645(2021), doi: 10.1002/adma.202104645.

[16] A. Barfuss, L. Dudy, M. R. Scholz, H. Roth, P. Höpfner, C. Blumenstein, G. Landolt, J. H. Dil, N. C. Plumb, M. Radovic, A. Bostwick, E. Rotenberg, A. Fleszar, G. Bihlmayer, D. Wortmann, G. Li, W. Hanke, R. Claessen, and J. Schäfer, "Elemental Topological Insulator with Tunable Fermi Level: Strained α-Sn on InSb(001)," *Phys. Rev. Letters*, **111** (15), 157205 (2013), doi: 10.1103/PhysRevLett.111.157205.

[17] Q. Barbedienne, J. Varignon, N. Reyren, A. Marty, C. Vergnaud, M. Jamet, C. Gomez-Carbonell, A. Lemaître, P. L. Fèvre, F. Bertran, A. Taleb-Ibrahimi, H. Jaffrès, J. M. George, and A. Fert, "Angular-resolved photoemission electron spectroscopy and transport studies of the elemental topological insulator α-Sn," *Phys. Rev. B*, **98** (19), 195445 (2018), doi: 10.1103/PhysRevB.98.195445.

[18] C. Z. Xu, Y. H. Chan, Y. Chen, P. Chen, X. Wang, C. Dejoie, M. H. Wong, J. A. Hlevyack, H. Ryu, H. Y. Kee, N. Tamura, M. Y. Chou, Z. Hussain, S. K. Mo, and T. C. Chiang, "Elemental Topological Dirac Semimetal: α-Sn on InSb(111)," *Phys. Rev. Lett.*, **118** (14), 146402 (2017), doi: 10.1103/PhysRevLett.118.146402.

[19] S. Küfner, M. Fitzner, and F. Bechstedt, "Topological α-Sn surface states versus film thickness and strain," *Phys. Rev. B*, **90** (12), 125312 (2014), doi: 10.1103/PhysRevB.90.125312.

[20] Y. Ohtsubo, P. L. Fèvre, F. Bertran, and A. Taleb-Ibrahimi, "Dirac Cone with Helical Spin Polarization in Ultrathin α-Sn (001) Films," *Phys. Rev. Lett*. **111** (21), 216401 (2013), doi: 10.1103/PhysRevLett.111.216401.

[21] H. Zhang, C. X. Liu, X. L. Qi, X. Dai, Z. Fang, and S. C. Zhang, "Topological insulators in Bi_2Se_3, Bi_2Te_3 and Sb_2Te_3 with a single Dirac cone on the surface," *Nat. Phys.*, **5**, 438–442 (2009), doi: 10.1038/nphys1270.

[22] P. Zareapour, A. Hayat, S. Y. F. Zhao, M. Kreshchuk, A. Jain, D. C. Kwok, N. Lee, S. W. Cheong, Z. Xu, A. Yang, G. D. Gu, S. Jia, R. J. Cava, and K. S. Burch, "Proximity-induced high-temperature superconductivity in the topological insulators Bi_2Se_3 and Bi_2Te_3," *Nat. Comm.*, **3**, 1056 (2012), doi: 10.1038/ncomms2042.

[23] S. V. Dordevic, M. S. Wolf, N. Stojilovic, H. Lei, and C. Petrovic, "Signatures of charge inhomogeneities in the infrared spectra of topological insulators Bi_2Se_3, Bi_2Te_3 and Sb_2Te_3," *J. Phys.: Condens. Matter*, **25**, 075501 (2013), doi: 10.1088/0953-8984/25/7/075501.

[24] J. Zhang, J. Caillaux, Z. Chen, M. Konczykowski, A. Hruban, A. Wołoś, A. Materna, L. Perfetti, E. Papalazarou, and M. Marsi, "Probing spin chirality of photoexcited topological insulators with circular dichroism: multi-dimensional time resolved ARPES on Bi_2Te_2Se and Bi_2Se_3," *Journal of Electron Spectroscopy and Related Phenomena*, **253**, 147125 (2021), doi: 10.1016/j.elspec.2021.147125.

[25] W. Al-Sawai, H. Lin, R. S. Markiewicz, L. A. Wray, Y. Xia, S.-Y. Xu, M. Z. Hasan, and A. Bansil, "Topological electronic structure in half-Heusler topological insulators," *Phys. Rev. B*, **82** (12), 125208 (2010), doi: 10.1103/PhysRevB.82.125208.

[26] Z. K. Liu, L. X. Yang, S.-C. Wu, C. Shekhar, J. Jiang, H. F. Yang, Y. Zhang, S.-K. Mo, Z. Hussain, B. Yan, C. Felser & Y. L. Chen, "Observation of unusual topological surface states in half-Heusler compounds LnPtBi (Ln=Lu, Y)," *Nat. Comm*, **7**, 12924 (2016), doi: 10.1038/ncomms12924.

[27] S. Chadov, X.-L. Qi, J. Kübler, G. H. Fecher, C. Felser, S.-C. Zhang, "Tunable multifunctional topological insulators in ternary Heusler compounds," *Nat. Mater.*, **9**, 541–545 (2010), doi: 10.1038/nmat2770.

[28] Graf, T., Felser, C., Parkin, S.S.P. (2016). Heusler Compounds: Applications in Spintronics. In: Xu, Y., Awschalom, D., Nitta, J. (eds) Handbook of Spintronics. Springer, Dordrecht. doi: 10.1007/978-94-007-6892-5_17.

[29] V. Bhardwaj, R. Chatterjee, "Topological Materials," Resonance 25, 431-441 (2020), doi: 10.1007/s12045-020-0955-5.

[30] M. Zhang, X. Wang, F. Song, R. Zhang, "Layered Topological Insulators and Semimetals for Magnetoresistance Type Sensors," Adv. Quan. Tech. 2, 1-2 (2018), doi: 10.1002/qute.201800039.

[31] S. Chege, P. Ning'i, J. Sifuna, et al., "Origin of band inversion in topological Bi_2Se_3," *AIP Advances* **10**, 095018 (2020), doi: 10.1063/5.0022525.

[32] M. Vijayakumar, M.S. Gopinathan, "Spin-orbit coupling constants of transition metal atoms and ions in density functional theory," *J. of M. Struc.: THEOCHEM* **361**, 15-19 (1996), doi: 10.1016/0166-1280(95)04297-0.

[33] A. Bansil, H. Lin, T. Das, "*Colloquium*: Topological band theory," *Rev. Mod. Phys.* **88**, 021004 (2016), doi: 10.1103/RevModPhys.88.021004.

[34] L. M. Schoop, F. Pielnhofer, B. V. Lotsch, "Chemical Principles of Topological Semimetals," *Chem. Mater.* **10**, 3155-3176 (2018), doi: 10.1021/acs.chemmater.7b05133.

[35] C. J. Palmstrøm, "Heusler compounds and spintronics," *Prog. in Crystal Growth and Chara. of Mats.*, 62 (2), 371-397 (2016), doi: 10.1016/j.pcrysgrow.2016.04.020.

[36] A. D. Rice, J. K. Kawasaki, N. Verma, D. J. Pennachio, B. D. Schultz, C. J. Palmstrøm, "Structural and electronic properties of molecular beam epitaxially

grown $Ni_{1+x}TiSn$ films," *J. Crystal Growth*, **467**, 71-76 (2017), doi: 10.1016/j.jcrysgro.2017.03.015.

[37] S. D. Harrington, A. D. Rice, T. L. Brown-Heft, B. Bonef, A. Sharan, A. P. McFadden, J. A. Logan, M. Pendharkar, M. M. Feldman, O. Mercan, A. G. Petukhov, A. Janotti, L. Colakerol Arslan, and C. J. Palmstrøm, "Growth, electrical, structural, and magnetic properties of half-Heusler $CoTi_{1-x}Fe_xSb$," *Phys. Rev. Materials*, **2** (1), 014406 (2018), doi: 10.1103/PhysRevMaterials.2.014406.

[38] J. W. Dong, L. C. Chen, J. Q. Xie, T. A. R. Müller, D. M. Carr, and C. J. Palmstrøm, "Epitaxial growth of ferromagnetic Ni_2MnGa on GaAs(001) using NiGa interlayers," *J. of App. Phys.*, **88** (12), 7357 (2000), doi: 10.1063/1.1326461.

[39] M. Jourdan, J. Minár, J. Braun, A. Kronenberg, S. Chadov, B. Balke, A. Gloskovskii, M. Kolbe, H.J. Elmers, G. Schönhense, H. Ebert, C. Felser, and M. Kläui, "Direct observation of half-metallicity in the Heusler compound Co_2MnSi," *Nat. Comm.*, **5**, 3974 (2014), doi: 10.1038/ncomms4974.

[40] H. Xiao, T. Hu, W. Liu, Y. L. Zhu, P. G. Li, G. Mu, J. Su, K. Li, and Z. Q. Mao, "Superconductivity in the half-Heusler compound TbPdBi," *Phys. Rev. B*, **97** (22), 224511 (2018), doi: 10.1103/PhysRevB.97.224511.

[41] T, Heft. *Engineering Magnetic and Topological Properties in Epitaxial Heusler Compounds*, University of California, Santa Barbara, Dissertation (2018).

[42] P. Chaudhary, K. K. Dubey, G. K. Shukla, S. Singh, S. Sadhukhan, S. Kanungo, A. K. Jena, S.-C. Lee, S. Bhattacharjee, J. Minár, and S. W. D'Souza, "Role of chemical disorder in tuning the Weyl points in vanadium doped Co_2TiSn," *Phys. Rev. Materials*, **5** (12), 124201 (2021), doi: 10.1103/PhysRevMaterials.5.124201.

[43] P. Neibecker, M. E. Gruner, X. Xu, R. Kainuma, W. Petry, R. Pentcheva, and M. Leitner, "Ordering tendencies and electronic properties in quaternary Heusler derivatives," Phys. Rev. B 96, 165131 (2017). *Philosophical Trans. of The Royal Society A*, **369** (1951), 0183 (2011), doi: 10.1098/rsta.2011.0183.

[44] W. Wanga, H. Sukegawa, R. Shan, T. Furubayashi, and K. Inomata, "Preparation and characterization of highly $L2_1$-ordered full-Heusler alloy $Co_2FeAl_{0.5}Si_{0.5}$ thin films for spintronics device applications," *Appl. Phys. Lett.*, **92**, 221912 (2008), doi: 10.1063/1.2940595.

[45] Y. Sakurabaa, T. Iwase, K. Saito, S. Mitani, and K. Takanashi, "Enhancement of spin-asymmetry by $L2_1$-ordering in $Co_2MnSi/Cr/Co_2MnSi$ current-perpendicular-to-plane magnetoresistance devices," *Appl. Phys. Lett.*, **94**, 012511 (2009), doi: 10.1063/1.3068492.

[46] Y. Sakuraba, K. Hyodo, A. Sakuma, S. Mitani, "Fermi level tuning and atomic ordering induced giant anomalous Nernst effect in $Co_2MnAl_{1-x}Si_x$ Heusler alloy," (2020), arXiv:1911.07741.

[47] Y. Sakuraba, K. Hyodo, A. Sakuma, S. Mitani, "Fermi level tuning and atomic ordering induced giant anomalous Nernst effect in $Co_2MnAl_{1-x}Si_x$ Heusler alloy," (2020), arXiv:1911.07741.

[48] R.A. de Groot, F.M. Mueller,P.G. Van Engen, and K.H.J. Buschow, "New Class of Materials: Half-Metallic Ferromagnets," *Phys. Rev. Lett*.**50**, 2024 (1983), doi: 10.1103/PhysRevLett.50.2024

[49] Z. Wen et al., "Optimization of half-Heusler PtMnSb alloy films for spintronic device applications," *J. of phys. D: App. Phys.* **51**, 435002 (2018)

[50] J. Krieft et al., "Co-sputtered PtMnSb thin films and PtMnSb/Pt bilayers for spin–orbit torque investigations," *Phys. Stat. Solidi* **11**, 4 (2017)

[51] M. Aitani, et al. "Fermi-Level Tuning of Topological Insulator Thin Films," Jpn. J. Appl. Phys. 52, 110112 (2013), doi: 10.7567/JJAP.52.110112

[52] B.A. Joyce, et al. "RHEED studies of heterojunction and quantum well formation during MBE growth — from multiple scattering to band offsets," *Surf. Sci.* **168**, 423-438 (1968)

[53] A. Ichimiya and P. I. Cohen, *Reflection High Energy Electron Diffraction*, Cambridge University Press (2011), ISBN: 978-0521184021.

[54] R. Gomer, *Field emission and field ionization*, American Institute of Physics (1993), ISBN: 978-1-56396-124-3.

[55] N. Derriche, S. Godin, R. Greenwood, A. Mercado, A. Warner, "Reflection High-Energy Electron Diffraction," 2019.

[56] N. D. Mermin and N. W. Ashcroft., *Solid State Physics*, Cengage Learning (2011), ISBN: 978-0030839931.

[57] B. E. Warren, *X-Ray Diffraction*, Dover Publications (1990), ISBN: 978-0486663173.

[58] I. Madni, G. A. Umana-Membreno, W. Lei, R. Gu, J. Antoszewski, L. Faraone, "X-Ray Reciprocal Space Mapping of MBE Grown HgCdTe on Alternative Substrates," *Crys. Research & Tech.*, **52** (9), 1700167 (2017), doi: 10.1002/crat.201700167.

[59] P. F. Fewster, "Reciprocal space mapping," *Critical Reviews in Solid State and Materials Sciences*, **22** (2), 69-110 (2006), doi: 10.1080/10408439708241259.

[60] S.R. Lee, B. L. Doyle, T. J. Drummond, J. W. Medernach, R. P. Schneider, Jr., "Reciprocal space mapping of epitaxial materials using position-sensitive x-ray detection," *annual Denver x-ray conference on applications of x-ray analysis,Steamboat Spring*, 1994.

[61] V. Holy, "High Resolution X-ray Reciprocal space mapping," *Acta Physica Polonica A*, **89** (1996).

[62] G. V. Hansson, H. H. Radamsson, and W.-X. Ni, "Strain and relaxation in Si-MBE structures studied by reciprocal space mapping using high resolution X-ray diffraction," *J. of Materials Science: Materials in Electronics*, **6**, 292–297 (1995), doi: 10.1007/BF00125883.

[63] G. Zhao, J. Li, L. Wang, Y. Meng, Z. Ji, F. Li, H. Wei, S. Yang, and Z. Wang, "Anisotropically biaxial strain in non-polar (112–0) plane $In_xGa_{1-x}N$/GaN layers investigated by X-ray reciprocal space mapping," *Scientific Reports*, **7**, 4497 (2017), doi: 10.1038/s41598-017-04854-8.

[64] A. Karsenty, "A Comprehensive Review of Integrated Hall Effects in Macro-, Micro-, Nanoscales, and Quantum Devices," *Sensors (Basel)*, 4163 (2020), doi: 10.3390/s20154163.

[65] N. Nagaosa, J. Sinova, S. Onoda, A. H. MacDonald, and N. P. Ong, "Anomalous Hall effect," *Rev. Mod. Phys.*, **82**, 1539–1592 (2010), doi: 10.1103/RevModPhys.82.1539

[66] Y. Zhang, Z. Liu, B. Zhou, Y. Kim, L. Yang, H. Ryu, C. Hwang, y. Chen, Z. Jussain, Z.-X. Shen, S.-K. Mo, "ARPES study of the epitaxially grown topological crystalline insulator SnTe(111)," *J. of Electron Spectroscopy and Related Phenomena*, **219**, 35-40 (2017), doi: 10.1016/j.elspec.2016.10.003.

[67] L. Locatelli, A. Kumar, P. Tsipas, A. Dimoulas, E. Longo, and R. Mantovan, "Magnetotransport and ARPES studies of the topological insulators Sb_2Te_3 and Bi_2Te_3 grown by MOCVD on large-area Si substrates," *Sci. Rep.*, **12**, 3891 (2022), doi: 10.1038/s41598-022-07496-7.

[68] B. Lv, T. Qian, and H. Ding, "Angle-resolved photoemission spectroscopy and its application to topological materials," *Nature Reviews Physics*, **1**, 609–626 (2019), doi: 10.1038/s42254-019-0088-5.

[69] O. Rader, J. Sánchez-Barriga, E. D. L. Rienks, A. Varykhalov, G. Springholz, L. V. Yashina, "Angle-Resolved Photoemission of Topological Matter: Examples from Magnetism, Electron Correlation, and Phase Transitions," *Physica status solidi*, **258** (1), 2000371 (2021), doi: 10.1002/pssb.202000371.

[70] N. Savage, "Topological materials move from the world of theoretical physics to experimental chemistry," *C&EN* **96**, 26 (2018). https://cen.acs.org/materials/electronic-materials/Topological-materials-move-world-theoretical/96/i26

[71] M. Edmonds, "A Topological-Insulator Sandwich for Efficient Microelectronics," *ALS news* (2022). https://als.lbl.gov/a-topological-insulator-sandwich-for-efficient-microelectronics/

[72] R. Xie, et al., "Progress, Advantages, and Challenges of Topological Material Catalysts," Small Sci. 2, 2100106 (2022), doi: 10.1002/smsc.202100106

[73] S. Roychowdhury, M. Samanta, et al., "Thermoelectric energy conversion and topological materials based on heavy metal chalcogenides*," J. of Sol. State Chem.* **275**, 103-123 (2019). doi: 10.1016/j.jssc.2019.04.005

[74] H. Wu, et al., "Magnetic memory driven by topological insulators," *Nat. Comm.* **12**, 6251 (2021), doi: 10.1038/s41467-021-26478-3

[75] D. Johnson, "Topological Insulators Offer Efficient Solution to Magnetic Memory: Researchers demonstrate that topological insulators are ten times as efficient as other materials at controlling magnetic memory," *IEEE Spec* (2014), https://spectrum.ieee.org/topological-insulators-offer-efficient-solution-to-magnetic-memory

[76] I. Belopolski, S.-Y. Xu, D. S. Sanchez, G. Chang, C. Guo, M. Neupane, H. Zheng, C.-C. Lee, S.-M. Huang, G. Bian, N. Alidoust, T.-R. Chang, B. Wang, X. Zhang, A. Bansil, H.-Tay Jeng, H. Lin, S. Jia, and M. Zahid Hasan, "Criteria for Directly Detecting Topological Fermi Arcs in Weyl Semimetals," *Phys. Rev. Lett.*, **116** (6), 066802 (2016), doi: 10.1103/PhysRevLett.116.066802.

[77] B. Q. Lv, H. M. Weng, B. B. Fu, X. P. Wang, H. Miao, J. Ma, P. Richard, X. C. Huang, L. X. Zhao, G. F. Chen, Z. Fang, X. Dai, T. Qian, and H. Ding, "Experimental Discovery of Weyl Semimetal TaAs," *Phys. Rev. X*, **5** (3), 031013 (2015), doi: 10.1103/PhysRevX.5.031013.

[78] Z. Li, H. Chen. S. Jin, D. Gan, W. Wang, L. Guo, and X. Chen, "Weyl Semimetal TaAs: Crystal Growth, Morphology, and Thermodynamics," *Cryst. Growth Des.*, **16** (3), 1172–1175 (2016), doi: 10.1021/acs.cgd.5b01758.

[79] R. Sankar, G. Peramaiyan, I. P. Muthuselvam, S. Xu, M. Z. Hasan, F. C. Chou, "Crystal growth and transport properties of Weyl semimetal TaAs," *J. phys. Condens. Matter.*, **30** (1), 015803 (2018), doi: 10.1088/1361-648X/aa9a75.

[80] J. Barth, G. H. Fecher, B. Balke, T. Graf, A. Shkabko, A. Weidenkaff, P. Klaer, M. Kallmayer, H.-J. Elmers, H. Yoshikawa, S. Ueda, K. Kobayashi and C. Felser "Anomalous transport properties of the half-metallic ferromagnets Co_2TiSi, Co_2TiGe and Co_2TiSn," *Phi. Trans. of. The Royal Soc. A* **369**, 1951 (2011), doi: 10.1098/rsta.2011.0183

[81] P. Neibecker, M. E. Gruner, X. Xu, R. Kainuma, W. Petry, R. Pentcheva, and M. Leitner, "Ordering tendencies and electronic properties in quaternary Heusler derivatives," Phys. Rev. B 96, 165131 (2017). *Philosophical Trans. of The Royal Society A*, **369** (1951), 0183 (2011), doi: 10.1098/rsta.2011.0183.

[82] W. Wanga, H. Sukegawa, R. Shan, T. Furubayashi, and K. Inomata, "Preparation and characterization of highly $L2_1$-ordered full-Heusler alloy $Co_2FeAl_{0.5}Si_{0.5}$ thin films for spintronics device applications," *Appl. Phys. Lett.*, **92**, 221912 (2008), doi: 10.1063/1.2940595.

[83] Y. Sakurabaa, T. Iwase, K. Saito, S. Mitani, and K. Takanashi, "Enhancement of spin-asymmetry by $L2_1$-ordering in Co_2MnSi/Cr/Co_2MnSi current-perpendicular-to-plane magnetoresistance devices," *Appl. Phys. Lett.*, **94**, 012511 (2009), doi: 10.1063/1.3068492.

[84] Y. Sakuraba, K. Hyodo, A. Sakuma, S. Mitani, "Fermi level tuning and atomic ordering induced giant anomalous Nernst effect in $Co_2MnAl_{1-x}Si_x$ Heusler alloy," (2020), arXiv:1911.07741.

[85] A. Tsukazaski et al., "$L2_1$ ordering of Co_2FeSn thin films promoted by high-temperature annealing," *AIP Advances* **12**, 065030 (2022), doi: 10.1063/5.0093195

[86] Y. Ando et al., "Influence of the $L2_1$ ordering degree on the magnetic properties of Co2MnSi Heusler films," *Journal of Applied Physics* **103**, 103910 (2008), doi: 10.1063/1.2931023

[87] DCA instruments Oy, https://www.dca.fi/

[88] M. Thompson, "Genplot RUMP," http://www.genplot.com, accessed: 2022-10-24.

[89] J. A. Logan, T. L. Brown-Heft, S. D. Harrington, N. S. Wilson, A. P. McFadden, A. D. Rice, M. Pendharkar, and C. J. Palmstrøm, "Growth, structural, and magnetic properties of single crystal full-Heusler Co_2TiGe thin films," *Journal of Applied Physics*, **121**, 213903 (2017), doi: 10.1063/1.4984311.

[90] J. Hu et al., "Anomalous Hall and Nernst Effects in Co_2TiSn and $Co_2Ti_{0.6}V_{0.4}Sn$ Heusler Thin Films," *Phy. Rev. App.* **10**, 044037 (2018), doi: 10.1103/PhysRevApplied.10.044037

[91] J. Q. Xiao, J. S. Jiang, C. L. Chien, "Giant magnetoresistance in nonmultilayer magnetic systems," *Phys. Rev. Lett.*, **68**, 3749 (1992), doi: 10.1103/PhysRevLett.68.3749

[92] W. G. Baber, "The contribution to the electrical resistance of metals from collisions between electrons," *Proc. R. Soc. London, Ser. A* **158**, 383 (1936), doi: 10.1098/rspa.1937.0027.

[93] D. A. Goodings, "Electrical Resistivity of Ferromagnetic Metals at Low Temperatures," *Phys. Rev.* **132**, 542 (1963), doi: 10.1103/PhysRev.132.542

[94] C. L. Chien, John Q. Xiao, and J. Samuel Jiang, "Giant negative magnetoresistance in granular ferromagnetic systems," *Journal of Applied Physics*, **73**, 5309 (1993), doi: 10.1063/1.353765.

[95] B. Ernst et al., "Anomalous Hall effect and the role of Berry curvature in Co2TiSn Heusler films," *Phy. Rev. B,* **100**, 054445 (2019), doi: 10.1103/PhysRevB.100.054445

[96] Z. Zhang et al., "Critical behavior in the half-metallic Heusler alloy Co2TiSn," Phys. Rev. B **100**, 214419 (2019), doi: 10.1103/PhysRevB.100.214419

[97] N. A. Sinitsyn, "Semiclassical theories of the anomalous Hall effect," J. *Phys. Condens. Matter*., **20** (2), 023201 (2008), doi: 10.1088/0953-8984/20/02/023201

[98] A. A. Burkov, "Negative longitudinal magnetoresistance in Dirac and Weyl metals," *Phys. Rev. B.* **91** (24), 245157 (2015), doi: 10.1103/PhysRevB.91.245157.

[99] A. A. Burkov, "Chiral anomaly and transport in Weyl metals," *J. Phys. Condens. Matter.*, **27**, 113201 (2015), doi: 10.48550/arXiv.1502.07609.

[100] Y. Tian, L. Ye, and X. Jin, "Proper Scaling of the Anomalous Hall effect," *Phys. Rev. Lett.* **103,** 1–4 (2009), doi: 10.1103/PhysRevLett.103.087206

[101] J. Smith, "The spontaneous hall effect in ferromagnetics II Show affiliations," Physica. **24**, 39 (1958), doi: 10.1016/S0031-8914(58)93541-9

[102] L. Berger, "Side-Jump Mechanism for the Hall Effect of Ferromagnets," *Phys. Rev. B.* **2**, 4559 (1970), doi: 10.1103/PhysRevB.2.4559

[103] H.-J. Kim, K.-S. Kim, J.-F. Wang, M. Sasaki, N. Satoh, A. Ohnishi, M. Kitaura, M. Yang, and L. Li, "Dirac versus weyl fermions in topological insulators: Adler-Bell-Jackiw anomaly in transport phenomena," *Phys. Rev. Lett.* **111,** 1–5 (2013), doi: 10.1103/PhysRevLett.111.246603.

[104] Butler, W. *et al.* Heusler Database. *Univ. of Alabama* (2015). Available at: http://heusleralloys.mint.ua.edu/.

[105] J. Kawasaki, "Epitaxial growth, surface, and electronic properties of unconventional semiconductors: RE-V/III-V nanocomposites and semiconducting Half Heusler alloys," Dissertation 2014. https://escholarship.org/uc/item/7bz192m3

[106] D. T. Son, B. Z. Spivak, "Chiral anomaly and classical negative magnetoresistance of Weyl metals," *Phys. Rev. B,* **88**, 104412 (2013), doi: 10.1103/PhysRevB.88.104412

[107] N. W. Ascroft, "Vegard's Law," *Phys. Rev. A* **43**, 3161 (1991), doi: 10.1103/PhysRevA.43.3161

[108] S.J. Youn et al., "Effects of the spin-oribit interaction in Heusler compounds: Electronic structures and Fermi surfaces of NiMnSb and PtMnSb," *Phys. Rev. B* **51**, 16 (1995), doi: 10.1103/PhysRevB.51.10436

[109] S. Gardelis, "Structural, magnetic, and electrical properties of NiMnSb thin films grown on InSb by pulsed-laser deposition," *Appl. Phys. Lett.* **85,** 3178 (2004), doi: 10.1063/1.1807026

[110] C. Ciccarelli, et al., "Room-temperature spin–orbit torque in NiMnSb," *Nat. Phys.* **12**, 855-860 (2016), doi: 10.1038/nphys3772

[111] Z. Wen, et al., "Spin-charge conversion in NiMnSb Heusler alloy films," *Sci. Adv.* **5**, 12 (2019), doi: 10.1126/sciadv.aaw9337

[112] P.G. Van Engel et al., "PtMnSb, a material with very high magnetooptical Kerr effect," *Appl. Phys. Lett*. **42**, 202 (1983), doi: 10.1063/1.93849

[113] S. Chatterjee et al., "Weak antilocalization in quasi-two-dimensional electronic states of epitaxial LuSb thin films," *Phy. Rev. B* **99**, 125134 (2019), doi: 10.1103/PhysRevB.99.125134

[114] N.E. Hussey, "Fermi-Surface Reconstruction and Two-Carrier Model for the Hall Effect in YBa2Cu4O8," *Phys. Rev. B* **82**, 020514 (2010), doi: 10.1103/PhysRevB.82.020514

[115] C. Shekhar et al., "Anomalous Hall effect in Weyl semimetal half-Heusler compounds RPtBi (R = Gd and Nd)," *PNAS* **115**, 9140-9144 (2018), doi: 10.1073/pnas.1810842115

[116] S. Granville, "Berry curvature origin of the thickness-dependent anomalous Hall effect in a ferromagnetic Weyl semimetal," *npj Quantum Materials* **6**, 17 (2021), doi: 10.1038/s41535-021-00315-8

[117] P. Raja, A. Barron, "1.15: Rutherford Backscattering of Thin Films," https://chem.libretexts.org/Bookshelves/Analytical_Chemistry/Physical_Methods_in_Chemistry_and_Nano_Science_(Barron)/01%3A_Elemental_Analysis/1.15%3A_Rutherford_Backscattering_of_Thin_Films